



UNIVERSITÀ DI PISA  
UNIVERSITY OF ADELAIDE

DOCTORAL THESIS

---

# Propagation Effects on HF Skywave MIMO Radar

---

*Supervisors:*

Prof. Marco MARTORELLA

*Author:*

Sonia TOMEI

Prof. Fabrizio BERIZZI

Prof. Christopher J. COLEMAN

*A thesis submitted in fulfilment of the requirements  
for the degree of Doctor of Philosophy*

Dottorato di Ricerca in Telerilevamento  
Scuola di Dottorato in Ingegneria *Leonardo da Vinci*  
The School of Electrical & Electronic Engineering  
SSD ING - INF/03

March 2014

# Declaration of Authorship

I, Sonia TOMEI, declare that this thesis titled, 'Propagation Effects on HF Skywave MIMO Radar' and the work presented in it are my own. I confirm that:

- This work was done wholly or mainly while in candidature for a research degree at this University.
- Where any part of this thesis has previously been submitted for a degree or any other qualification at this University or any other institution, this has been clearly stated.
- Where I have consulted the published work of others, this is always clearly attributed.
- Where I have quoted from the work of others, the source is always given. With the exception of such quotations, this thesis is entirely my own work.
- I have acknowledged all main sources of help.
- Where the thesis is based on work done by myself jointly with others, I have made clear exactly what was done by others and what I have contributed myself.

Signed:

---

Date:

---

*“Those who are in love with practice without knowledge are like the sailor who gets into a ship without rudder or compass, and who never can be certain where he is going.”*

Leonardo Da Vinci

UNIVERSITY OF PISA  
UNIVERSITY OF ADELAIDE

# *Abstract*

Doctor of Philosophy

## **Propagation Effects on HF Skywave MIMO Radar**

by Sonia TOMEI

MIMO technology has been suggested as an effective tool to overcome some of the issues typical of conventional OTH skywave radars. The advantages of the application of MIMO technology to HF Skywave radars is based on the transmission of multiple linearly independent waveforms and their separation at the receiver. Notwithstanding, the high instability of the ionosphere is responsible for severe signal fading and degradation that can prevent the separation with consequences on the radar performance. The present thesis is concerned with the problem of the effects of ionospheric propagation, which are analyzed from a theoretical point of view at first, through the description of the ionosphere morphology and the disturbances that affect the ionospheric electron density structure. The relation between structural variations in the ionosphere and the transmitted signal parameters has been then derived. A radar signal simulator has been realized accordingly to the signal model proposed in the thesis. The results of the thesis concern three different aspects of propagation in HF MIMO radars. The orthogonality of the transmitted waveforms after ionospheric propagation is analyzed first, while the effects of ionospheric propagation on the results of conventional beamforming is studied secondly. The performance of the radar receiver are evaluated in terms of ROCs in case of multipath propagation and compared to the single path case.

# *Acknowledgements*

Furthermore, I would like to express my sincere gratitude to my supervisors, Prof. Marco Martorella, Prof. Fabrizio Berizzi and Prof. Christopher J. Coleman, for their continuous support of my Ph.D study and research, for their patience, motivation, enthusiasm, and immense knowledge.

Thanks to Prof. Douglas A. Gray and to the guys at the School of Electric and Electronic Engineering in Adelaide for their help and kindness.

Thanks to all my fellow labmates in Pisa, for making me laugh even when there was nothing to laugh about... A special thank goes to Elisa, for her countless suggestions and priceless help.

Thanks to my family who have supported me during my studies.

Least but not the last, my deepest gratitude goes to Alessio, who shared this amazing and challenging adventure with me, for his infinite patience, for the days he spent reading my draft (while I was reading his..) and for his love.

Thank you.

Sonia

# Contents

Declaration of Authorship	i
Abstract	iii
Acknowledgements	iv
List of Figures	viii
List of Tables	xii
Abbreviations	xiii
Physical Constants	xv
Symbols	xvi
<b>1 Introduction</b>	<b>1</b>
1.1 Background and Motivation	1
1.2 Objective & Major contributions	4
1.3 Chapters outline	5
<b>2 HF, MIMO or HF-MIMO radar?</b>	<b>10</b>
2.1 HF radar	10
2.1.1 Brief history of OTH radar	11
2.1.2 The reflection mechanism	12
2.1.3 Main issues in OTH skywave radar	14
2.2 MIMO radar	19
2.2.1 Brief history of MIMO radar	19
2.2.2 Basic principles of MIMO radar	20
2.3 HF-MIMO radar	25
2.3.1 HF-MIMO radar: capabilities & issues	25
2.4 Summary	28
<b>3 HF MIMO radar: Signal Modulation &amp; Demodulation</b>	<b>30</b>

3.1	HF MIMO radar simulator . . . . .	30
3.1.1	The transmitter block . . . . .	33
3.1.1.1	Waveform generator . . . . .	34
3.2	The receiver block . . . . .	40
3.2.1	Waveform parameters selection: issues . . . . .	45
3.2.1.1	Frequency selection: the Frequency Management System . . . . .	46
3.2.1.2	Waveform parameters selection . . . . .	48
3.3	Summary . . . . .	55
<b>4</b>	<b>The ionosphere &amp; its effects on propagating signals</b>	<b>57</b>
4.1	The ionosphere . . . . .	58
4.1.1	Ionosphere structure . . . . .	58
4.1.2	Ionospheric models . . . . .	62
4.1.3	Ionospheric variation and disturbances . . . . .	63
4.2	Ionospheric effects on radiowave propagation . . . . .	71
4.2.1	Signal Losses . . . . .	71
4.2.2	Fading . . . . .	72
4.2.2.1	Polarization fading: Faraday Rotation effect . . . . .	72
4.2.2.2	Amplitude Fading . . . . .	74
4.2.2.3	Multipath Fading . . . . .	75
4.3	Summary . . . . .	77
<b>5</b>	<b>HF MIMO Radar Signal Model</b>	<b>78</b>
5.1	Signal Model . . . . .	79
5.1.1	Vector Notation . . . . .	86
5.2	Target Detection . . . . .	91
5.3	Summary . . . . .	93
<b>6</b>	<b>HF MIMO Radar Simulator</b>	<b>95</b>
6.1	HF MIMO simulator steps . . . . .	96
6.1.1	System Geometry Definition . . . . .	99
6.1.2	Evaluation of available paths . . . . .	100
6.1.2.1	Ionospheric state definition . . . . .	103
6.1.2.2	Skip distance evaluation . . . . .	104
6.2	Preliminary results . . . . .	109
6.2.1	Signal parameters vs frequency . . . . .	109
6.2.1.1	Scenario Definition . . . . .	110
6.2.2	Signal parameters vs array dimension . . . . .	111
6.3	Summary . . . . .	115
<b>7</b>	<b>Results</b>	<b>118</b>
7.1	Scenario settings & geometry description . . . . .	119
7.1.1	Geometry 1 . . . . .	119
7.1.2	Geometry 2 . . . . .	119

---

7.1.3	Geometry 3	123
7.2	Waveform orthogonality results	127
7.3	Beamforming results	127
7.3.1	Beamforming for geometry 1	131
7.3.2	Beamforming for geometry 2	138
7.3.3	Beamforming for geometry 3	144
7.3.4	Remarks on beamforming results	150
7.4	Detection performance results and ROC	150
7.5	Summary	151
<b>8</b>	<b>Conclusion &amp; Future Work</b>	<b>154</b>
	<b>Bibliography</b>	<b>158</b>

# List of Figures

1.1	The <i>telemobiloscope</i> , now at the Deutsches Museum Masterpieces of Science and Technology in Munich . . . . .	1
2.1	Representation of an e.m. wave striking into the ionosphere with angle of incidence $\phi_{inc,0}$ . . . . .	13
2.2	Representation of an e.m. wave propagating through the ionosphere: (a) ideal propagation for both rays; (b) non ideal propagation for the blue ray. . . . .	17
2.3	Representation of the concept of virtual array. . . . .	22
2.4	Representation of the virtual array obtained with sparse array. . . . .	24
3.1	Representation of the ionospheric propagation and HF MIMO radar simulator . . . . .	32
3.2	High level block diagram of the HF-MIMO radar signal simulator . . . . .	33
3.3	Representation of the element space signalling technique. Each transmitter element emits a waveform orthogonal to the waveforms emitted by the other elements of the transmitter. . . . .	36
3.4	Representation of the beam space signalling technique. A number of orthogonal beams is synthesized by properly adjusting the waveforms weights. . . . .	37
3.5	High level block diagram of the receiver for ES signalling technique . . . . .	42
3.6	High level block diagram of the receiver for ES signalling technique via deramping . . . . .	43
3.7	Representation of the Frequency Management System. . . . .	47
3.8	(a) $\tau_{off} = 0$ ; (b) $\tau_{off} = T_{sw}$ (c) nearly orthofonal LFM-CW. . . . .	50
3.9	Schematic representation of the reconstructed ambiguity function when a single frequency is associated to each single transmitted waveform. . . . .	52
3.10	Schematic representation of LFM CW stepped frequency waveforms. . . . .	53
3.11	Schematic representation of the reconstructed ambiguity function when LFM CW stepped frequency transmitted waveforms are used. . . . .	53
3.12	Ideal vs real LPF amplitude-frequency response function. . . . .	54
4.1	Representation of plasma frequency variations in altitude and range for a quiet ionosphere. Results are based on a Matlab routine created by C.J. Coleman. . . . .	59
4.2	Day and night representation of ionospheric layers. . . . .	60

4.3	Electron density profiles vs altitude for different hours of the day. . . . .	64
4.4	Montly variation of the electron density profiles vs altitude at midday. . . . .	65
4.5	Electron density profiles vs altitude for different hours of the day in case of ionospheric perturbation (TIDs). . . . .	66
4.6	Representation of plasma frequency variations in altitude and range in presence of TIDs for two different instants of time. Results are based on a Matlab routine created by C.J. Coleman. . . . .	70
5.1	Schematic representation of the propagation between two end points through a dispersive medium. . . . .	80
5.2	Block diagram of the path travelled by the transmitted signals in a HF MIMO radar. $y_m(t)$ denotes the contribution from the $m^{th}$ transmitter to the target. . . . .	86
5.3	Schematic representation of the structure of $\mathbf{h}_{kn}$ and $\sigma_{kn}$ as they appear in Eq.(5.16) and Eq.(5.17) respectively. Both the schematic representation refer to the output of the generic $k^{th}$ matched filter in the $n^{th}$ receiver chain. . . . .	88
6.1	HF MIMO simulator flow chart . . . . .	98
6.2	Representation of the geocentric system of reference $(x, y, z)$ and the local system of reference $(p, q, r)$ . . . . .	101
6.3	Elevation angle, $\phi_{el}$ , and incident angle, $\phi_{inc}$ , for a radiowave strik- ing into the ionosphere . . . . .	102
6.4	Plasma frequency grid representation . . . . .	105
6.5	Skip distance values for a same ionosphere at different hour of the day vs frequency. Missing frequencies in some plots are frequencies that completely cross the ionosphere without being reflected. . . . .	107
6.6	Zoom of Fig.6.5 for low frequencies. . . . .	108
6.7	Phase path (a), group path (b), losses (c) and Faraday rotation (d) trend vs frequency in an unperturbed ionosphere . . . . .	111
6.8	Phase path (a), group path (b), losses (c) and Faraday rotation (d) trend vs frequency in presence of TIDs. . . . .	112
6.9	Phase path (a), group path (b), losses (c) and Faraday rotation (d) trend vs array dimension in presence of TIDs . . . . .	113
6.10	Phase path (a), group path (b), losses (c) and Faraday rotation (d) trend vs array dimension in presence of TIDs . . . . .	114
6.11	Phase path (a), group path (b), losses (c) and Faraday rotation (d) trend vs array dimension in presence of TIDs . . . . .	115
6.12	Phase path (a), group path (b), losses (c) and Faraday rotation (d) trend vs array dimension in presence of TIDs . . . . .	116
6.13	Phase path (a), group path (b), losses (c) and Faraday rotation (d) trend vs array dimension in an unperturbed ionosphere . . . . .	117
7.1	Representation of the transmitter and receiver location (a) and vir- tual array elements location (b) . . . . .	120
7.2	Geometric representation of circular geometry . . . . .	121

7.3	Representation of the transmitter and receiver locations (a) and virtual array elements location (b) . . . . .	123
7.4	Zoom of the center of the virtual array represented in Fig.7.3(b). As can be seen the central element is missing. . . . .	124
7.5	Representation of the transmitter and receiver location (a) and virtual array elements location (b) . . . . .	125
7.6	Zoom of the center of the virtual array represented in Fig.7.5(b). As can be seen the central element is missing. . . . .	126
7.7	Cross correlation matrices of the set of transmitted waveforms after ionospheric propagation at the input of the demodulation block for geometry 1. . . . .	128
7.8	Cross correlation matrices of the set of transmitted waveforms after ionospheric propagation at the input of the demodulation block for geometry 2. . . . .	129
7.9	Cross correlation matrices of the set of transmitted waveforms after ionospheric propagation at the input of the demodulation block for geometry 3. . . . .	130
7.10	Result of conventional beamforming for the geometry in Fig.7.1 at time $t = 0$ with respect to the disturbances period . . . . .	131
7.11	Result of conventional beamforming for the geometry in Fig.7.1 at time $t = 0$ with respect to the disturbances period . . . . .	132
7.12	Result of conventional beamforming for the geometry in Fig.7.1 at time $t = 0$ with respect to the disturbances period . . . . .	133
7.13	Result of conventional beamforming for the geometry in Fig.7.1 at time $t = 300$ with respect to the disturbances period . . . . .	134
7.14	Result of conventional beamforming for the geometry in Fig.7.1 at time $t = 300$ with respect to the disturbances period . . . . .	135
7.15	Result of conventional beamforming for the geometry in Fig.7.1 at time $t = 500$ with respect to the disturbances period . . . . .	136
7.16	Result of conventional beamforming for the geometry in Fig.7.1 at time $t = 500$ with respect to the disturbances period . . . . .	137
7.17	Result of conventional beamforming for the geometry in Fig.7.3 at time $t = 0$ with respect to the disturbances period . . . . .	138
7.18	Result of conventional beamforming for the geometry in Fig.7.1 at time $t = 0$ with respect to the disturbances period . . . . .	139
7.19	Result of conventional beamforming for the geometry in Fig.7.3 at time $t = 300$ with respect to the disturbances period . . . . .	140
7.20	Result of conventional beamforming for the geometry in Fig.7.3 at time $t = 300$ with respect to the disturbances period . . . . .	141
7.21	Result of conventional beamforming for the geometry in Fig.7.3 at time $t = 500$ with respect to the disturbances period . . . . .	142
7.22	Result of conventional beamforming for the geometry in Fig.7.3 at time $t = 500$ with respect to the disturbances period . . . . .	143
7.23	Result of conventional beamforming for the geometry in Fig.7.5 at time $t = 0$ with respect to the disturbances period . . . . .	144

---

7.24	Result of conventional beamforming for the geometry in Fig.7.5 at time $t = 0$ with respect to the disturbances period . . . . .	145
7.25	Result of conventional beamforming for the geometry in Fig.7.5 at time $t = 300$ with respect to the disturbances period . . . . .	146
7.26	Result of conventional beamforming for the geometry in Fig.7.5 at time $t = 300$ with respect to the disturbances period . . . . .	147
7.27	Result of conventional beamforming for the geometry in Fig.7.5 at time $t = 500$ with respect to the disturbances period . . . . .	148
7.28	Result of conventional beamforming for the geometry in Fig.7.5 at time $t = 500$ with respect to the disturbances period . . . . .	149
7.29	ROC curves in case of single path propagation (a) and ionospheric multipath (b) . . . . .	153

# List of Tables

6.1	Parameters defining the unperturbed ionosphere . . . . .	105
6.2	AWGs parameters . . . . .	106
6.3	Geographical coordinates of the transmitter site. . . . .	106
6.4	Target local coordinates. . . . .	106
6.5	Elevation angle values corresponding to each frequency and hour considered in Fig.6.5 . . . . .	108
7.1	Angular location of main lobe (ML), angular location and amplitude of highest sidelobe (SL1) and number of sidelobes higher than $-10dB$	133
7.2	Angular location of main lobe (ML), angular location and amplitude of highest sidelobe (SL1) and number of sidelobes higher than $-10dB$	139
7.3	Angular location of main lobe (ML), angular location and amplitude of highest sidelobe (SL1) and number of sidelobes higher than $-10dB$	145

# Abbreviations

<b>AWG</b>	<b>A</b> tmospheric <b>G</b> ravity <b>W</b> ave
<b>BS</b>	<b>B</b> eam <b>S</b> pace
<b>CIT</b>	<b>C</b> oherent <b>I</b> ntegration <b>I</b> nterval
<b>CNR</b>	<b>C</b> lutter-to- <b>N</b> oise <b>R</b> atio
<b>DSTO</b>	<b>D</b> efence <b>S</b> cience <b>T</b> echnology <b>O</b> rganization
<b>e.m.</b>	electromagnetic
<b>ES</b>	<b>E</b> lement <b>S</b> pace
<b>FM-CW</b>	<b>F</b> requency- <b>M</b> odulated <b>C</b> ontinuous <b>W</b> ave
<b>FMS</b>	<b>F</b> requency <b>M</b> anagement <b>S</b> ystem
<b>FR</b>	<b>F</b> araday <b>R</b> otation
<b>HF</b>	<b>H</b> igh <b>F</b> requency
<b>HILOW</b>	<b>H</b> igh frequency <b>L</b> -shaped <b>O</b> rthogonal <b>W</b> aveform
<b>i.i.d.</b>	independent and <b>i</b> dentically <b>d</b> istributed
<b>IRI</b>	<b>I</b> nternational <b>R</b> eference <b>I</b> onosphere
<b>JORN</b>	<b>J</b> indalee <b>O</b> perational <b>R</b> adar <b>N</b> etwork
<b>LPF</b>	<b>L</b> ow <b>P</b> ass <b>F</b> ilter
<b>NOSTRADAMUS</b>	<b>N</b> Ouveau <b>S</b> ysteme <b>T</b> RAnshorizon <b>D</b> ecametrique Applicant les <b>M</b> ethodes <b>U</b> tilisees en <b>S</b> tudio
<b>LFM-CW</b>	<b>L</b> inear <b>F</b> requency- <b>M</b> odulated <b>C</b> ontinuous <b>W</b> ave
<b>LoS</b>	<b>L</b> ine of <b>S</b> ight
<b>LPF</b>	<b>L</b> ow <b>P</b> ass <b>F</b> ilter
<b>LSTID</b>	<b>L</b> arge <b>S</b> cale <b>T</b> ravelling <b>I</b> onospheric <b>D</b> isturbance
<b>MIMO</b>	<b>M</b> ultiple <b>I</b> nterface <b>M</b> ultiple <b>O</b> utput
<b>MISO</b>	<b>M</b> ultiple <b>I</b> nterface <b>S</b> ingle <b>O</b> utput

---

<b>MF</b>	<b>M</b> atched <b>F</b> ilter
<b>MSTID</b>	<b>M</b> edium <b>S</b> cale <b>T</b> ravelling <b>I</b> onospheric <b>D</b> isturbance
<b>NRL</b>	<b>N</b> aval <b>R</b> esearch <b>L</b> aboratory
<b>O</b>	<b>O</b> rdinary
<b>ONERA</b>	<b>O</b> ffice <b>N</b> ational d'Etudes et de Recherches <b>A</b> érospatiales
<b>OTH</b>	<b>O</b> ver <b>T</b> he <b>H</b> orizon
<b>PCA</b>	<b>P</b> olar <b>C</b> ap <b>A</b> bsorption
<b>pdf</b>	probability density function
<b>P.P.</b>	<b>P</b> erturbed <b>P</b> ath
<b>PRF</b>	<b>P</b> ulse <b>R</b> epetition <b>F</b> requency
<b>RADAR</b>	<b>R</b> adio <b>D</b> etection <b>A</b> nd <b>R</b> anging
<b>RCS</b>	<b>R</b> adar <b>C</b> ross <b>S</b> ection
<b>RIAS</b>	<b>R</b> adar a <b>I</b> mpulsion <b>S</b> ynthetique
<b>RVP</b>	<b>R</b> esidual <b>V</b> ideo <b>P</b> hase
<b>rx</b>	receiver
<b>SAR</b>	<b>S</b> ynthetic <b>A</b> perture <b>R</b> adar
<b>SIAR</b>	<b>S</b> ynthetic <b>I</b> mpulse <b>A</b> perture <b>R</b> adar
<b>SID</b>	<b>S</b> udden <b>I</b> onospheric <b>D</b> isturbance
<b>SISO</b>	<b>S</b> ingle <b>I</b> nput <b>S</b> ingle <b>O</b> utput
<b>SSTID</b>	<b>S</b> mall <b>S</b> cale <b>T</b> ravelling <b>I</b> onospheric <b>D</b> isturbance
<b>TID</b>	<b>T</b> ravelling <b>I</b> onospheric <b>D</b> isturbance
<b>tx</b>	transmitter
<b>UHF</b>	<b>U</b> ltra <b>H</b> igh <b>F</b> requency
<b>U.P.</b>	<b>U</b> nperturbed <b>P</b> ath
<b>VHF</b>	<b>V</b> ery <b>H</b> igh <b>F</b> requency
<b>X</b>	<b>e</b> Xtraordinary

# Physical Constants

Speed of Light  $c = 2.997\,924\,58 \times 10^8 \text{ ms}^{-\text{s}}$  (exact)

Electron Charge  $e = -1,602 \times 10^{-19} \text{ C}$

Electron Mass  $m_e = 9,109 \times 10^{-31} \text{ Kg}$

Vacuum Permittivity  $\epsilon_0 = 8,854 \times 10^{-12} \text{ F}^{-\text{m}}$

# Symbols

## A

$A_{FR}$	signal attenuation due to FR
$A^{(r)}$	FR attenuation along the $r^{th}$ path in the MISO case
$A^{(r,q)}$	FR attenuation in the MISO case
$A_m^{(r,q)}$	FR attenuation for the $m^{th}$ transmitted signal in the SISO case
$A_{mn}^{(r,q)}$	FR attenuation for the $m^{th}$ tx signal at the $n^{th}$ rx in the MIMO case

## B

<b>B</b>	Earth's magnetic induction field
$B$	signal bandwidth
$B_{av}$	available bandwidth
$B_g$	guard bandwidth
$B_{LPF}$	low pass filter bandwidth
$B_m$	bandwidth of the $m^{th}$ transmitted signal

## C

$C_{att}$	constant accounting for signal attenuations and losses
-----------	--

## D

$D_{array}$	maximum dimension of the array
$ds$	unit vector of length along the wave path

## E

## F

$f_0$	wave frequency
$f_{beat,max}$	maximum beat frequency
$f_{off}$	frequency offset

$f_{opt}$	optimum carrier frequency at the output of the FMS
$\hat{f}_{opt}$	estimated optimum carrier frequency at the output of the FMS
$f_{pi}$	plasma frequency of the $i^{th}$ ionospheric layer
$f_{pi0}$	plasma frequency of the unperturbed ionosphere
$f_{pi}$	plasma frequency of the perturbed ionosphere
$f_{pmax}$	maximum plasma frequency value
$f_{out}$	demodulated signal frequency after deramping
$f_{\mathbf{u} H_0}$	pdf of the measured signal under $H_0$
$f_{\mathbf{u} H_1}$	pdf of the measured signal under $H_1$
$f_{\mathbf{w}}$	pdf of noise
$f_{\sigma}$	pdf of target's RCS
	<b><u>G</u></b>
	<b><u>H</u></b>
<b>H</b>	global propagation channel matrix
$H_0$	hypothesis of no target in the range cell under test
$H_1$	hypothesis of target present in the range cell under test
$\mathbf{h}_{kn}$	propagation channel factors vector
$\mathbf{H}_n$	matrix of the propagation channel factors at the $n^{th}$ rx
	<b><u>I</u></b>
	<b><u>J</u></b>
	<b><u>K</u></b>
$k_0$	wavenumber
	<b><u>L</u></b>
$L^{(r)}$	signal losses along the $r^{th}$ path in the MISO case
$L^{(r,q)}$	signal losses in the MISO case
$L_m^{(r,q)}$	signal losses for the $m^{th}$ tx signal in the SISO case
$L_{mn}^{(r,q)}$	signal losses for the $m^{th}$ tx signal at the $n^{th}$ rx in the MIMO case
	<b><u>M</u></b>
$m_m(t)$	baseband signal emitted by the $m^{th}$ tx
$M_m(f)$	baseband signal emitted by the $m^{th}$ tx in the frequency domain
$\mathbf{M}_p$	matrix for coordinates transformation

**N**

$N_B$	number of beams in the BS signalling technique
$n_e$	electron density
$nmi$	nautical miles
$N_{rx}$	number of rx elements
$N_{tx}$	number of tx elements
$N_w$	number of orthogonal waveforms

**O**

$O$	centre of the local system of reference $T_p(p, q, r)$
-----	--

**P**

$\mathbf{p}$	vector of coordinates in the local system of reference
$P(\theta)$	power associated with the tx signals at location given by $\theta$
$\mathbf{p}_{Tm}$	$m^{th}$ tx coordinates in the local system of reference
$\mathbf{p}_T$	target's coordinate in the local system of reference
$\mathbf{p}_{Rn}$	$n^{th}$ rx coordinates in the local system of reference
$\mathbf{p}_{Tx,m}$	$m^{th}$ tx coordinates in the local system of reference
$P_{total}$	total phase path length

**Q**

$Q$	number of paths between the target and the rx in the MISO case
-----	--

**R**

$\mathbf{R}$	correlation matrix of the transmitted signals
$R_g$	range distance
$R_{max}$	maximum range
$R$	number of paths between the tx and the target in the MISO case
$R_m$	number of paths between the $m^{th}$ tx and the target in the SISO case
$\mathbf{R}_w$	noise covariance matrix
$\mathbf{R}_\sigma$	target's RCS covariance matrix

**S**

$s_m(t)$	$m^{th}$ waveform of a set of orthogonal waveforms
----------	--

**T**

$T_p(p, q, r)$	local Cartesian system of reference $T_{rep}$
----------------	---

$T_{sw}$	ramp duration
$T_x(x, y, z)$	geocentric system of reference
	<u><a href="#">U</a></u>
$\mathbf{u}$	vector notation of the received signal
$u_{kn}$	vector notation of the output of the $k^{th}$ MF at the $n^{th}$ rx
$\mathbf{u}_n$	vector of the outputs of all the MFs at the $n^{th}$ rx
	<u><a href="#">V</a></u>
	<u><a href="#">W</a></u>
$\mathbf{w}$	total noise contribution at the receiver at the output of the MFs
$w_{kn}$	noise at the output of the $k^{th}$ MF at the $n^{th}$ rx
$\mathbf{w}_n$	output noise of all the MFs at the $n^{th}$ rx
	<u><a href="#">X</a></u>
$\mathbf{x}$	vector of coordinates in the local system of reference
$x$	horizontal direction of the plasma frequency modulation
$x_m(t)$	signal emitted by the $m^{th}$ tx
	<u><a href="#">Y</a></u>
$y_T(t)$	signal at the target location in the MISO case
	<u><a href="#">Z</a></u>
$z(t)$	received signal in the MIMO case
$z_m(t)$	signal emitted by the $m^{th}$ tx at the rx site
$z_{miso}(t)$	received signal in the mISO case
$z_{T,nk}$	output of the $k^{th}$ matched filter at the $n^{th}$ rx
$z_{siso}(t)$	received signal in the SISO case
$z_{siso,m}(t)$	received signal from the $m^{th}$ tx in the MISO case

### Greek Symbols

	<u><a href="#">α</a></u>
$\alpha_m$	amplitude of the $m^{th}$ transmitted signal
$\alpha_{mn}$	amplitude of the $m^{th}$ transmitted signal at the $n^{th}$ rx
	<u><a href="#">β</a></u>
$\beta_i$	direction of the $i^{th}$ beam in the BS signalling technique

	<u><math>\gamma</math></u>	
$\gamma$		chirprate
$\gamma_0$		pdf multiplying factor under $H_0$
$\gamma_1$		pdf multiplying factor under $H_1$
	<u><math>\delta</math></u>	
$\delta\mu$		refractive index contribution due to ionospheric perturbation
$\delta_R$		range resolution
$\delta_{CR}$		cross range resolution cell dimension
	<u><math>\epsilon</math></u>	
$\epsilon$		amplitude modulation of the plasma frequency
	<u><math>\theta</math></u>	
$\overline{\delta_R}$		fixed range resolution
$\vartheta_0$		initial phase of the plasma frequency modulation
	<u><math>\lambda</math></u>	
$\lambda$		wavelength
	<u><math>\mu</math></u>	
$\mu_i$		refractive index of the $i^{th}$ ionospheric layer
$\mu_p$		refractive index for a perturbed ionosphere
	<u><math>\rho</math></u>	
$\phi_{inc,i}$		angle with an e.m. wave strikes into the $i^{th}$ ionospheric layer
	<u><math>\sigma</math></u>	
$\sigma$		vector of the target's RCS
$\sigma(\xi)$		scaling factor accounting for the target RCS
$\sigma_{kn}$		vector of target's reflectivity
$\sigma_n$		vector containing the target RCS at the $n^{th}$ rx
$\sigma^{(r,q)}$		target's RCS for the signal propagating in the MISO case
$\sigma_m^{(r,q)}$		target's RCS for the $m^{th}$ transmitted signal in the SISO case
	<u><math>\tau</math></u>	
$\tau$		time delay
$\tau_{max}$		maximum time delay
$\tau_{off}$		time offset of the transmitted signals

$\tau_{p,mn}$	propagation delay between the $m^{th}$ tx to the $n^{th}$ rx via target
$\tau_{G,T}^{(r)}$	group delay at the target location
$\tau_G^{(r,q)}$	group delay of the signal propagating in the MISO case
$\tau_{Gm}^{(r,q)}$	group delay of $m^{th}$ transmitted signal in the SISO case
$\tau_{P,T}^{(r)}$	phase delay at the target location
$\tau_P^{(r,q)}$	phase delay of the signal propagating in the MISO case
$\tau_{Pm}^{(r,q)}$	phase delay of the $m^{th}$ transmitted signal in the SISO case
$\tau_T^{(r)}$	phase delay between the tx and the target along the $r^{th}$ path
	<u><math>\phi</math></u>
$\phi_{el}$	elevation angle of an e.m. wave
$\Phi$	amount of FR
$\Delta\varphi$	phase shift
	<u><math>\chi</math></u>
$\chi$	LRT threshold
$\chi_1$	LRT modified threshold
	<u><math>\omega</math></u>
$\omega_0$	angular carrier frequency

### Math Operators

$E\{\}$	expectation
$H$	Hermitian operator
$\delta_{i,j}$	Kronecker delta function
$T$	transpose operator
$*$	conjugate operator

# Chapter 1

## Introduction

### 1.1 Background and Motivation

Hertz's studies about electromagnetic (e.m.) wave propagation and Marconi's experiments about radio propagation are the basis of the development of the radar theory. The first working system that can be associated to a radar was developed by Christian Hulsmeyer in 1904. It was a simple anti-collision ship detector, called *telemobiloscope* [1].



FIGURE 1.1: The *telemobiloscope*, now at the Deutsches Museum Masterpieces of Science and Technology in Munich

During the World War II radar technology exponentially improved its capabilities. In 1935, Sir Robert Watson-Watt patented the first radar system while the acronym *RADAR*, meaning *Radio Detection and Ranging* was coined by USA Navy in 1940.

Different radar technologies have been developed since then: SAR (Synthetic Aperture Radar) has been developed during the 1950s while phased array systems appeared during the 1960s, together with Over The Horizon (OTH) radars.

OTH Skywave radars are especially suitable for surveillance of wide areas because of their ability to reach regions far beyond the optical horizon via ionospheric propagation. The idea of detecting targets over the horizon attracted the military community worldwide so that in the '70s many different countries invested in the OTH radar research and developed a number of OTH systems.

The ionosphere is fundamental for effective OTH applications, but radio wave refraction is an extremely complex mechanism, which is highly sensitive to changes in the ionosphere structure. As a consequence, a number of aspects have to be considered in the design of an OTH radar in relation to the effects of the ionosphere on the waveform propagation. In particular, the selection of the carrier frequency is fundamental since every wave with a frequency higher than the maximum supported frequency by the ionosphere at the time of transmission will not be reflected towards the Earth's surface. Secondly, ionospheric turbulence can cause fluctuations in the ionospheric structure. Such movements of the ionospheric layers are responsible for clutter returns to spread in Doppler that can mask target returns. Thirdly, attenuation due to ionospheric propagation losses can be so high to prevent the detection of the signals at the receiver site. In addition, one of the main cause of corruption at HF frequencies is due to *fading*. Fading is mainly caused by fluctuations in the ionospheric structure that lead to fluctuations in the signal amplitude with consequences in the signal detection process. In particular, the presence of multiple paths between the transmitter and the receiver, i.e., *multipath fading*, is responsible for either constructive or destructive interference among all the contributions at the receiver site, so that the attenuation in the signal amplitude varies unpredictably with ionospheric fluctuations. Moreover, during the propagation through the ionosphere the polarization vector is subject to a rotation, known as *Faraday effect*, which is responsible for polarization mismatch at the receiver, usually referred as *polarization fading*. Finally, additional *amplitude fading* is caused by focusing and defocussing effects undergone by the

signal during the propagation through the ionosphere.

In the last few decades, the enhanced capabilities of digital signal processing have allowed for the development of complex systems, such as Multiple Input Multiple Output (MIMO) radars. MIMO radars rely on the use of multiple transmitters that emit a set of linearly independent waveforms that are properly separated and processed at the receiver site.

Recently, the capabilities of MIMO radar have been suggested as an effective way to overcome the limitations typical of OTH radars. In fact, the transmission of orthogonal waveforms provide a means of avoiding the use of adaptive filter at the transmitter to adapt the waveforms parameters. In addition, the transmitted waveforms can be properly combined to synthesise a desired beam pattern and focus the transmitted energy in specific directions. Notwithstanding, the correct functioning of MIMO radars relies on the assumption that the propagation channel does not affect the waveform orthogonality. Such an assumption cannot be done in OTH radar, since the ionosphere may affect the orthogonality of the transmitted waveforms so that they cannot be separate at the receiver.

It is then clear that a study about the way ionosphere affects the transmitted waveforms is essential for the design of an HF MIMO radar system. In particular, the relation between ionosphere disturbances and the signal variations is essential for the correct design of the system and for an understanding of the capabilities of MIMO technology for OTH applications. For this reason, a proper signal model able to account for ionospheric effects on propagating signals in an HF MIMO scenario is derived in the present thesis. Based on this model, an HF MIMO radar signal simulator is developed, which is able to set the ionosphere state, select the transmitted waveforms and evaluate the signal at the receiver site after ionospheric propagation. Such a simulator is an effective tool for the evaluation of the propagation effects on HF skywave MIMO radar. In particular, the present thesis focuses on three different aspects. The way the ionosphere and its turbulence affect the transmitted waveforms orthogonality is analysed first by means of

correlation matrices.

Then, the effects of ionospheric propagation on DoA estimation are analysed. Simulations for different geometries are performed to test whether the system configuration has an impact on the DoA estimation performance.

The receiver performance are then analysed in terms of ROC curves. In this regard, the case in which ionospheric multipath is present is compared with the case in which there is no multipath, in order to understand the implications on the radar performance.

## 1.2 Objective & Major contributions

The objective of the present thesis is to develop an HF-MIMO radar simulator in order to study the ionospheric propagation effects on HF signals. The theoretical studies about the propagation of HF radio waves through the ionosphere have led to the definition of different block that mirror the capabilities of the simulator. In particular, the developed simulator is able to

- Simulate both unperturbed and perturbed ionosphere accounting for perturbations such as TIDs

- Simulate different sets of transmitted waveforms, both for beamspace and element space HF MIMO radar

- Check the waveform orthogonality after ionospheric propagation in order to understand the effects of the propagation medium and its disturbances on the propagating signals

- Evaluate the radar detection performance by means of the ROC curves in presence of ionospheric multipath

During the research activity, the following papers have been written

- Tomei, S.; Coleman, C.J.; Martorella, M.; Berizzi, F., "The effect of Travelling Ionospheric Disturbances upon the performance of an HF skywave MIMO radar," Radar Conference (RADAR), 2013 IEEE , vol., no., pp.1,6, April 29 2013-May 3 2013 doi: 10.1109/RADAR.2013.6586047
- S. Tomei, M. Martorella, C. J. Coleman, F. Berizzi, "The effect of Travelling Ionospheric Disturbances upon the performance of an HF skywave MIMO radar", submitted to the 2014 International Radar Conferece, Lille, France
- S. Tomei, M. Martorella, C. J. Coleman, F. Berizzi, "Propagation Effects on HF Skywave MIMO Radar", which is a journal paper under revision.

### 1.3 Chapters outline

The chapters of the present thesis are organized as follows.

#### Chapter 2

##### HF, MIMO or HF-MIMO radar?

The aim of this chapter is to understand the real capabilities of HF-MIMO radar. For this reason, a literature review about conventional HF radar technology is provided, in order to have an insight about the advantages and the issues related to this kind of systems, especially for OTH skywave applications. Special attention is given to the problem of spread Doppler clutter, signal losses, fading and carrier frequency selection.

MIMO technology is then introduced for conventional microwave radars. The advantages of both coherent and statistical MIMO radars are discussed and the concept of orthogonal waveforms introduced. Special attention is then given to the concept of virtual array that allows for the synthesis of large phantom arrays by using a reduced number of real antennas.

The advantages of MIMO radars with respect to conventional phased array radars

are explained in order to justify the application of MIMO technology to conventional phased array HF radar systems. At this point, HF MIMO radar is suggested as a viable solution to overcome some of the typical issues of conventional OTH skywave radars. In particular, the transmission of orthogonal waveforms is suggested as an effective alternative to avoid the use of adaptive delayed filters to adapt the waveforms parameters according to the ionospheric channel state and a viable solution for the introduction of spatial directivity by means of beam pattern synthesis achieved via combination of the transmitted waveforms (beam space solution).

## Chapter 3

### HF MIMO radar: Signal Modulation & Demodulation

HF MIMO radars rely on the transmission of linearly independent waveforms and on the separation of these contributions at the receiver. For this reason, this chapter focuses on the problem of modulation and demodulation of the transmitted waveforms.

Two different transmission techniques are introduced, namely the beam space and the element space technique. The concept of waveform orthogonality is investigated and the methods that can be used to achieve waveform orthogonality presented. Special attention is given to the element space technique which is widely used for OTH skywave applications. In this regard, the issues related to the spectral occupancy of the transmitted orthogonal waveforms is investigated since the ionosphere usually supports signal bandwidth of the order of few tens of  $kHz$ .

On the receiver side, the demodulation via conventional matched filter and dechirping are both analysed.

## Chapter 4

### The ionosphere & its effects on propagating signals

This chapter focuses on the morphological structure of the ionosphere in order to understand the physics behind the corruption that HF radio waves experience when passing through this medium.

In particular, the variations of the basic ionospheric structure are analysed and the relation between such variations in the ionospheric structure and signal distortions have been shown. In particular, three type of fading have been identified, namely polarization, amplitude and multipath fading. With regard of the polarization fading, a description of the effect known as Faraday rotation has been provided. Focussing and defocussing effects have been described to explain amplitude fading. At the end, a description of the multipath fading has been provided. Special attention has been given to the effect of TIDs since they are ever present and, hence, pose a significant threat to the operation of OTHR.

## Chapter 5

### HF MIMO Radar Signal Model

The aim of this chapter is to develop a signal model able to account for the ionospheric effects in an HF MIMO radar.

The model is developed starting from the SISO case and extending the result to the MIMO case. The problem of the signal evaluation at the receiver site is split into two sub-problems, the propagation from the transmitter to the target, and from the target to the receiver.

Signal losses, fading and ionospheric multipath are accounted in the signal model.

## Chapter 6

### HF MIMO Radar Simulator

This chapter is about the HF MIMO simulator that consists of the various blocks presented in the previous chapters. The flow chart of the simulator is described to explain the operations performed by the simulator for the evaluation of the signal at the receiver site.

The problem of software routines optimization is faced. In particular, the application of the linear interpolation for waveform parameters approximation is justified by a number of preliminary results.

## Chapter 7

### Results

The results obtained with the simulator described in Ch.6 are shown in this chapter.

In particular, three different aspects of HF MIMO skywave radars are studied. The problem of waveform orthogonality after ionospheric propagation is investigated via the analysis of the correlation matrices of the transmitted signals at the receiver site.

The effects of ionospheric perturbations on the DoA estimation are then analysed via conventional beamforming results. The results are shown for different geometries in order to understand whether the system configuration has an impact on the beamforming results.

At the end, the system performance are analysed in terms of ROC curves. In particular, the case in which only one path is considered is compared with the case in which ionospheric multipath is present.

## **Chapter 8**

### **Conclusions**

This chapter concludes the thesis summarising the results obtained and the major contributions of this research activity. The results analyse three different aspects

- Analysis of the waveform orthogonality after ionospheric propagation
- Conventional beamforming performance evaluation against both perturbed and unperturbed ionosphere
- HF MIMO radar receiver performance analysis in terms of ROC.

# Chapter 2

## HF, MIMO or HF-MIMO radar?

HF-MIMO (*High Frequency - Multiple Input Multiple Output*) radars exploit the advantages typical of MIMO technology to overcome some of the limitations that typically affect HF radars.

The present chapter aims to understand the real capabilities of HF-MIMO radars. For this reason, a general overview of HF radar will be given, with a special attention to the main issues related to the effects of the propagation medium, i.e. the ionosphere, on the propagating signals.

Then, MIMO radars will be considered and the features of these systems described. The advantages that can be obtained by merging the two technologies, i.e. MIMO and HF radar, will be investigated in order to understand what issues can be solved and what issues still remain.

### 2.1 HF radar

Interaction between e.m. waves and the Earth's atmosphere allows for the transmission of energy far beyond the conventional horizon. Radar systems exploiting the aforementioned property are identified by the name of *Over The Horizon* (OTH) radars.

### 2.1.1 Brief history of OTH radar

After World War I, studies of the Earth's atmosphere showed the possibility of transmitting signals far beyond the horizon by exploiting ionospheric refraction at HF frequencies. Up to the 1960s, this property was used mainly for communication purposes. Its application to radar had to wait for the development of powerful computers in the 1970s. The great military interest in such systems led to the development of the firsts HF radar, thanks to new and more capable signal processing. In 1961, the U.S. Naval Research Laboratory (NRL) tested a system capable of detection and tracking of targets at a range up to 200nmi.

The idea of detecting targets over the horizon attracted the military community worldwide so that later in the '70s many different countries invested in the OTH radar research and developed a number of OTH systems.

The AN/TPS-71 and AN/FPS-118 OTH radars were developed by U.S. NRL for air traffic surveillance while the studies pursued by the Australian Defence Science Technology Organization (DSTO) were at the basis of the Jindalee radar [2]. The Jindalee radar was the basis of *JORN*, Jindalee Operational Radar Network [3], which forms a system for the surveillance of the air and surface approaches to Australia.

In Europe, the French ONERA (*Office National d'Etudes et de Recherches Aérospatiales*) developed a system for air traffic surveillance called NOTRADAMUS (*NOuveau Systeme TRAnshorizon Decametrique Appliquant les Methodes Utilisees en Studio*) [4][5].

Russia and China have also hosted major OTH radar programs over the last half century, but little information is available about these systems. In [6] a survey of the active Chinese radars states the presence of OTH radars in China while in the 1982 an article about the Russian Duga-3, known as the *woodpecker*, an OTH radar whose transmissions interfered with other HF systems, appeared in The Miami Herald.

Nowadays, OTH radar systems fall into two basic categories, *Surface-wave* and *Skywave* radars [7].

Surface wave radars exploit the ground wave propagation of vertically polarized

HF waves over highly conductive surfaces, such as the sea water. They are mostly employed for oceanographic remote sensing applications, such as sea spectrum measurements [8] and detection of small vessels [9] up to a range up to 400km.

On the other hand, Skywave radars rely on the refractive properties of the ionosphere to return the e.m. waves back to the Earth's surface at distances beyond the horizon [10], usually in a range from 100km up to 3500km. As well as the detection and tracking of aircraft, ships and missiles [11], skywave radars are also employed for surveillance of large areas [12], sea state diagnostic [13][14], detection of natural phenomena such as tsunami [15] and cyclones [16], and ocean backscatter measurements.

The present work focuses on skywave radar, so a brief review of the refraction mechanism and a survey of the main issues related to OTH Skywave radar will be provided in the next sections.

### 2.1.2 The reflection mechanism

At HF frequencies, over the horizon propagation can occur through the refraction of radio signals by the ionosphere.

The ionosphere is a layer within the Earth's atmosphere which extends from about 50km up to 500km and it is characterized by the presence of free charged particles, in particular electrons. The distribution of free electrons increases with the altitude and different layers of ionization, namely the D, E and F-regions, can be identified. Moreover, the concentration of the electrons varies on a diurnal scale, as well as with the season of year, the solar activity and the geographical position. A description of the median behaviour of the ionosphere and the main features of each region is provided by the *International Reference Ionosphere* (IRI) climatological model [17].

Consider the ionosphere to be divided into thin layers with constant refractive index. When a radio wave at frequency  $f_0$  strikes into the ionosphere with an incident angle equal to  $\phi_{inc,0}$ , the interaction with the free electrons makes the

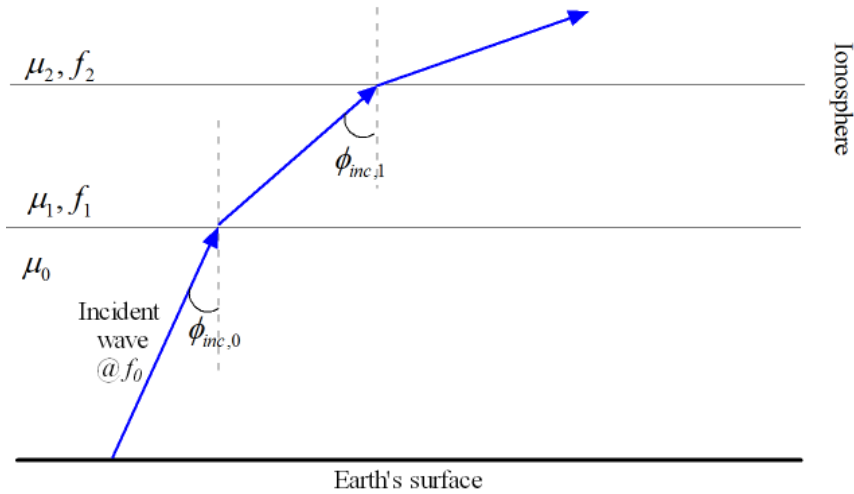


FIGURE 2.1: Representation of an e.m. wave striking into the ionosphere with angle of incidence  $\phi_{inc,0}$

wave progressively bending according to Snell's Law

$$\mu_{i-1} \sin \phi_{inc,i-1} = \mu_i \sin \phi_{inc,i} \quad i = 1, 2, \dots \quad (2.1)$$

where  $\mu_i$  is the refractive index of the  $i^{th}$  layer of the ionosphere. The refractive index depends on the electron density in the layer,  $n_e$ , as shown by the relations in Eq.(2.2)<sup>1</sup>

$$\mu_i^2 = 1 - \left( \frac{f_{p_i}}{f_0} \right)^2 \quad (2.2)$$

$$f_{p_i} \cong 9 \times 10^{-6} \sqrt{n_e}$$

The quantity  $f_{p_i}$  is the *plasma frequency* of the  $i^{th}$  layer in *Hz* and is related to the electron density. Each ionospheric region (D,E and F) is, in fact, characterized by a maximum plasma frequency,  $f_{p_{max}}$ , also known as *critical frequency*, which sets an upper bound to the frequency that can be used in order to achieve the reflection in the same layer.

<sup>1</sup>This formulation is valid for a ionospheric model in which the collisions among molecules and ions can be neglected and there is no imposed magnetic field. For a deep insight see [10].

In fact, the reflection of radio waves with oblique incidence occurs when the product between the transmitted frequency and the cosine of the incident angle is lower than the maximum plasma frequency, i.e.

$$f_0 \cos \phi_{inc,0} < f_{p_{max}} \quad (2.3)$$

When the wave frequency is selected so that the upper bound in Eq.(2.3) is exceeded, then the refractive index  $\mu \cong 1$  and the wave completely crosses the ionosphere without being reflected.

This means that a *blind* region exists, since for a fixed frequency  $f_0$  a maximum elevation angle will exist so that each signal launched for higher elevations will *escape* and there will be no reflection by the ionosphere. This blind region is also called *skip* region and it is not illuminated by radar.

### 2.1.3 Main issues in OTH skywave radar

The ionosphere is fundamental to effective Over The Horizon applications, but it is clear that refraction of radio waves is a very complex mechanism, which is sensitive to changes in the ionosphere structure. A number of aspects has to be considered in the design of an OTH radar in relation the effects of the ionosphere on the waveform propagation:

1. frequency and waveform selection
2. propagation losses
3. spread Doppler clutter
4. fading.

Details of these phenomena will be given in the following paragraphs.

## Frequency and waveform selection

As seen in Sect.2.1.2, the reflection mechanism is strictly related to the waveform frequency. In particular, the wave frequency must comply with the upper bound in Eq.(2.3). It is worth pointing out that because of the instability of the ionosphere, such upper bound must be properly estimated in order to select a proper wave frequency. The estimation of the ionospheric properties is a challenging task because of the variation of the electron density on a diurnal and seasonal scale. Beside the limitations imposed by the ionospheric state, the wave frequency selection must comply also with the spectral occupancy of the HF band, where broadcast transmissions and a number of other users that have the permission to transmit in this range of frequency.

Modern OTH radars exploit the information gathered by an auxiliary system able to analyse both the ionosphere and the availability of free channels in the HF band in order to adaptively select a suitable wave frequency and effectively exploit the refraction and avoid interference from other users[18].

Similarly, HF band occupancy and ionospheric state must be accounted for the selection of the waveform bandwidth. The dispersiveness of the ionospheric channel from one side and the limited range of frequencies in the HF spectrum from the other, seldom allows for transmissions over bandwidth larger than  $100kHz$ .

Typical values of the instantaneous bandwidth supported by the ionosphere are in the range from  $10kHz$  to  $50kHz$  with consequent range resolution values ranging from  $3km$  to  $15km$ .

The peculiar features of the ionospheric channel require additional considerations for the waveform selection when compared with microwave radars. In particular, the ionosphere behaves like a *waveguide*, in which multiple paths are possible and these can interfere either constructively or destructively. Moreover, strong clutter returns must be accounted for selecting a waveform able to achieve the desired

measurements capabilities. The most used waveform in OTH radar is the LFM-CW (*Linear Frequency-Modulated Continuous Wave*) and variations of it.

## Ionospheric propagation losses

Signals propagating through the ionosphere experience a significant amount of losses in the path between the transmitter and the receiver.

First of all, the lower regions of the ionosphere, such as the D region, are responsible for high absorption losses. Ground reflection losses occur when the signal bounces at the Earth's surface in multiple hop propagation.

## Spread Doppler clutter

Spread Doppler clutter can be responsible for masking target returns and arises due to variations in the ionospheric structure. It is caused by ionospheric turbulence of it more across the path of the e.m. wave. This can cause clutter return to spread in Doppler and mask target returns.

Different techniques have been investigated in literature to suppress this phenomenon and enhance target detection, but also to model them for ionosphere investigation [19].

## Fading

Fluctuations in the electron distribution are responsible for fluctuations in the amplitude of the propagating signal, commonly known as *fading*. Depending on the ionospheric state, the fluctuations in the signal amplitude can be so strong to prevent the detection by the receiver. Fading phenomena can be grouped in three different categories

- multipath fading

- polarization fading
- amplitude fading.

*Multipath fading* is due to the presence of multiple paths, also known as *modes*, between the transmitter and the receiver. In fact, in an ideal case, signals corresponding to the lowest elevation angles within the antenna beam are expected to reach the furthest ranges by means of reflection at the highest layers while signals corresponding to the highest elevation angles are expected to reach the nearest ranges, as shown in Fig.2.2(a).

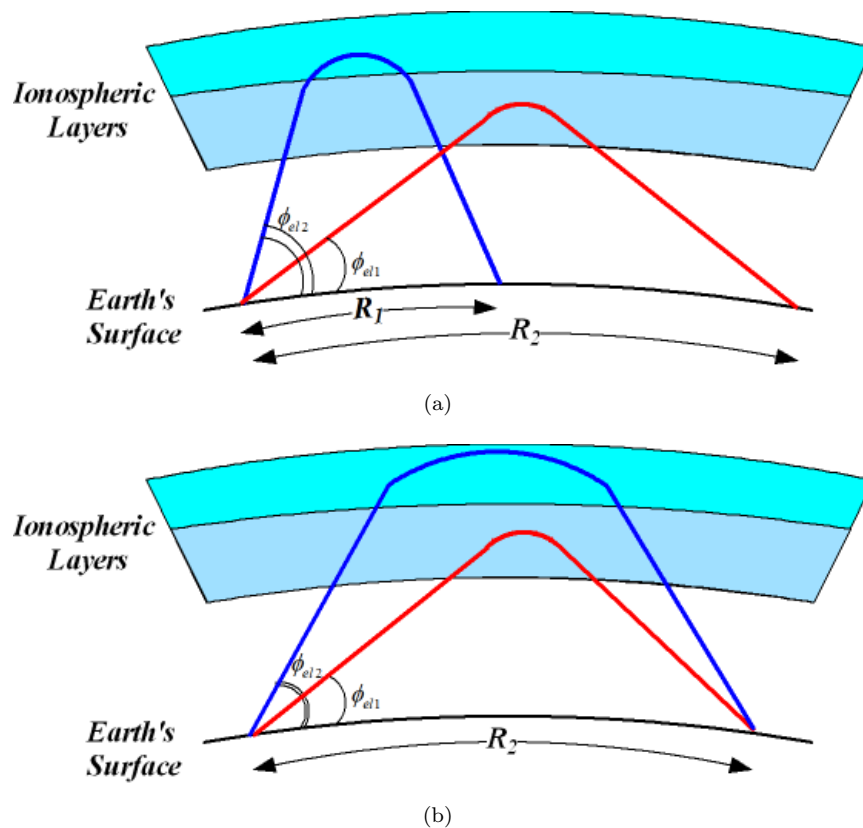


FIGURE 2.2: Representation of an e.m. wave propagating through the ionosphere: (a) ideal propagation for both rays; (b) non ideal propagation for the blue ray.

In a real case, signals at the highest elevation angles may propagate by bouncing few times within the same layer, such that they too reach great ranges, as shown in Fig.2.2(b). In such a scenario, multiple paths with different time delays arrives

at the receiver so that the received signal may appear as the superimposition of different modes. At the receiver, the interference among all the contributions can be either constructive or destructive, leading to unpredictable attenuation in the signal amplitude that varies with ionospheric fluctuations [20].

Different techniques has been investigated in literature to mitigated or actually suppress this phenomenon and improve radar performance, such as in [21].

*Polarization fading* is due to the rotation in the polarization vector of the transmitted wave. It can cause polarization mismatch at the receiver and the associated signal attenuation can be so strong to cause the signal to be lost. Once again, fluctuations in the ionosphere can cause fluctuations in polarization and hence fading. A way to overcome this problem is the use of circularly polarized waves, but this is at high cost solution for practical HF antennas [22].

*Amplitude fading* is related to focusing and defocussing effects that can occur during propagation. Once again, fluctuations in the ionosphere can cause fluctuations in this effect and hence fading.

## Antenna design

OTH radar operation via skywave will require frequencies between  $3MHz$  and  $30MHz$ . Consequently, the wavelength ranges from  $10m$  to  $100m$  and the antenna must be designed accordingly. In fact, the cross range resolution cell dimension ( $\delta_{CR}$ ) at a distance  $R_g$  from the radar depends on the antenna size,  $D_{array}$ , and the radar wavelength,  $\lambda$ , according to the following relation

$$\delta_{CR} = \frac{R_g \lambda}{D_{array}} \quad (2.4)$$

So, the bigger the antenna, the smaller the cross range resolution cell dimension for a fixed frequency. Typical value of cross range resolution cell dimension at a

distance  $R_g = 1200km$  for a frequency equal to  $15MHz$  is equal to  $12km$  to  $8km$ , which implies an antenna size of  $2$  to  $3km$ . Such a big antenna places extreme requirements on the transmitter/receiver sites, as well as in the design of the antenna feeding network.

## 2.2 MIMO radar

The idea of transmitting different coded signals from different transmitter elements to obtain benefits in multipath fading environment has been widely exploited in communications under the name of *Multiple Input Multiple Output* (MIMO) technology [23].

A similar idea has been imported in the radar field of research leading to the concept of *MIMO* radar.

### 2.2.1 Brief history of MIMO radar

Waveform diversity is at the basis of the first studies about MIMO radar.

In fact, during the 1970s, Mehra [24] investigated the problem of selecting different system inputs to improve parameter estimation in a radar system.

The first working system that can actually be called a MIMO radar is the French experimental program RIAS (*Radar a Impulsion et Antenne Synthetique*), in English SIAR (*Synthetic pulse and Antenna Radar*) [25][26], undertaken by the French research agency ONERA during the 1980s for air surveillance task. The RIAS transmitter consists of a circular array in which the elements emit a set of orthogonal waveforms.

### 2.2.2 Basic principles of MIMO radar

During the last two decades, MIMO radar research developed more and more, covering different aspects of the same concept.

The advantages of systems employing *multiple* transmitters and *multiple* receivers have been investigated [27][28][29][30] and the differences between MIMO and phased array radar discussed as well. In fact, the key aspect of MIMO radar is that each element of the MIMO radar transmitter can emit a different waveform instead of a scaled version the same waveform as it happens in conventional phased array radar.

Two different configurations of MIMO radar have been identified, according to their interpretation of the concept of *multiple*.

The first category is often called *statistical* MIMO and is based on a multistatic radar in which the antenna elements are so widely spaced that the target RCS (*Radar Cross Section*) seen from different transmitter-receiver pairs is decorrelated [31]. In other words, this category exploits *multiple* RCS measurements to overcome the RCS fluctuations that can degrade the radar performance [32]. Moreover, this angular diversity is used to collect Doppler estimates from multiple directions allowing for the detection of slow moving targets. It has also been demonstrated that coherent processing in widely spaced MIMO radars allows for high range resolution, far beyond the resolution supported by the waveform bandwidth [33].

The second configuration, called *coherent* MIMO, exploits the transmission of *multiple* linearly independent signals from closely spaced, i.e. colocated, antennas [34]. This waveform diversity enables a significant improvement in target detection and parameter estimation and an enhancement in flexibility for beampattern design.

The fundamental advantage of colocated MIMO radar is related to the concept of *virtual array* [28]. This concept refers to the fact that the number of the processed signals at the receiver is up to  $N_{Rx}$  times the number of transmitted waveforms, where  $N_{Rx}$  indicates the number of receiver elements. In fact, consider a transmitter array with  $N_{tx}$  elements and a receiver array with  $N_{rx}$  elements. Let  $s_m(t)$  be the waveform emitted by the  $n^{th}$  transmitter element and suppose that the  $N_{tx}$  transmitted waveforms are orthogonal

$$\int s_i(t)s_j^*(t)dt = \delta_{ij} \quad (2.5)$$

where  $\delta_{ij}$  is the Kronecker delta function, defined as

$$\delta_{ij} = \begin{cases} 1 & \text{if } i = j \\ 0 & \text{if } i \neq j \end{cases} \quad (2.6)$$

At the receiver, a bank of matched filters is used to separate the signals coming from different transmitters.

The output of the  $k^{th}$  matched filter at the  $n^{th}$  receiver element the received signal can be rewritten as [35]

$$z_{Tn,k}(t) = \sigma(\xi)e^{jk_0\mathbf{u}_t^T(\mathbf{p}_{Tm}+\mathbf{p}_{Rn})} \quad (2.7)$$

where

$k_0 = \frac{2\pi}{\lambda_0}$  is the wavenumber

$\sigma(\xi)$  is a coefficient taking into account the target reflectivity

$\mathbf{p}_{Tm}$  is the location of the  $m^{th}$  transmitter element

$\mathbf{p}_{Rn}$  is the location of the  $n^{th}$  receiver element

$\mathbf{u}_t^T \in \mathbb{R}^3$  is a unit vector along the LoS.

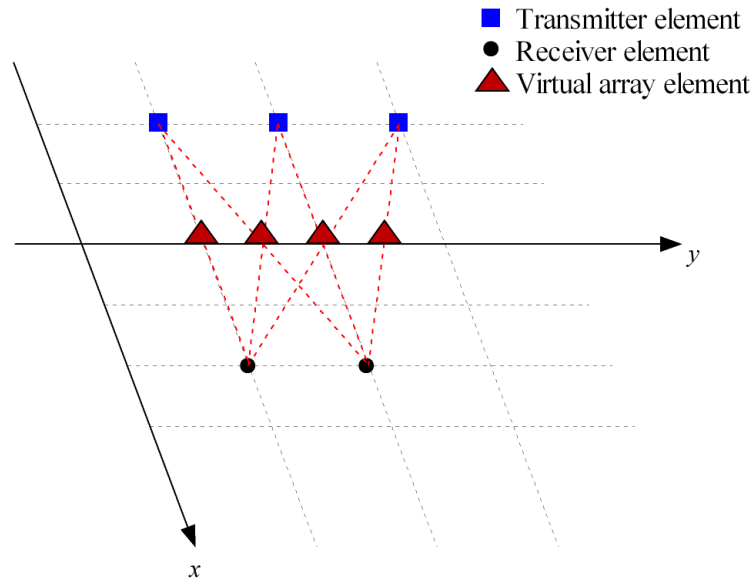


FIGURE 2.3: Representation of the concept of virtual array.

As it can be easily noticed, the phase of the received signal depends on the spatial convolution of the transmitter and the receiver elements locations

$$\{\mathbf{p}_{Tm} + \mathbf{p}_{Rn} | m = 1, \dots, N_{tx}, n = 1, 2, \dots, N_{Rx}\} \quad (2.8)$$

as if the received signals were coming from the elements of an array with locations given by Eq.(2.8).

Thus, it can be concluded that the result is the same of the case in which a transmit-receive array with  $N_{tx}N_{Rx}$  elements is used, but using only a number of real antennas equal to  $N_{tx} + N_{Rx}$  is actually employed.

A graphic representation of the concept of virtual array is given in Fig.2.3, where the blue squares represent the transmitter elements, the black rounds the receiver elements and the red triangles the virtual array elements. From the same figure, it can be easily noticed that the locations of the central elements of the virtual array are *repeated*, which means that the same virtual location is the result of the spatial convolution between the locations of two different transmitter-receiver pairs.

It means that the actual number of virtual array elements is 6, distributed on only 4 different locations, two of them with 2 antennas. The same concept can

be clearly explained considering the notation used in [36] by Forsythe and Bliss. They denote a linear array with the following notation

$$\{1 \ 1 \ 1\} \quad (2.9)$$

where each 1 corresponds to an array element. Suppose the transmitter is the one in Eq.(2.9) and the receiver is  $\{1 \ 1\}$ . Then, the virtual array is given by  $\{1 \ 2 \ 2 \ 1\}$ , where the number 2 means that in the same location two antennas can be found.

In order to avoid repetitions, *sparse* arrays can be used. Suppose the transmitter is  $\{1 \ 1 \ 1 \ 1\}$  and the receiver is a sparse array,  $\{1 \ 0 \ 0 \ 0 \ 1 \ 0 \ 0 \ 0 \ 1 \ 0 \ 0 \ 0 \ 1\}$ .

Then the virtual array is

$$\{1 \ 1 \ 1 \ 1 \ 1 \ 1 \ 1 \ 1 \ 1 \ 1 \ 1 \ 1 \ 1 \ 1 \ 1 \ 1\} \quad (2.10)$$

As it can be easily noticed, in the last example only 8 real antennas have been used ( $N_{tx} = N_{rx} = 4$ ), but the virtual array consists of a linear array of 16 equally spaced antennas. This means that the construction of the virtual array can be used to obtain an actually *filled* array from sparse arrays. The same concept is graphically explained in Fig.2.4. Moreover, the aperture of the virtual array is bigger than the aperture of both the real array used, so that better angular resolution can be obtained by exploiting the MIMO configuration.

So, two important considerations can be drawn

1. considering the concept of virtual array, the actual number of real elements can be reduced
2. larger aperture can be obtained using few transmitter and few receiver elements.

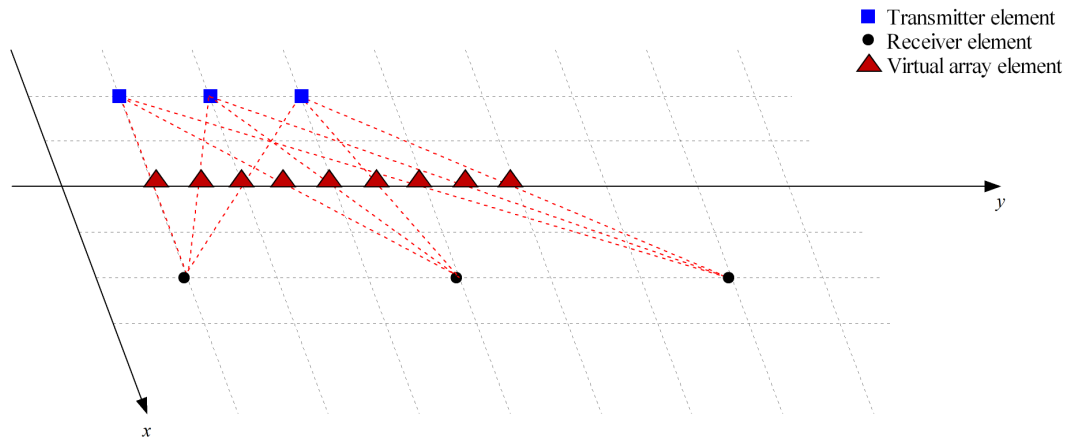


FIGURE 2.4: Representation of the virtual array obtained with sparse array.

The idea of transmitting uncorrelated signals has led to the investigation of signalling techniques in MIMO radar. In many papers, the idea of uncorrelated signals has been translated into the concept of *orthogonality* [37] [38]. Furthermore, it is true that a degree of correlation can be accepted for transmitter beam pattern design [39] [40]. In fact, in [41][42] it has been demonstrated that a desired beam pattern can be approximated by selecting a set of transmitted waveform that allows for a certain degree of cross-correlation.

The waveform design in MIMO radar remains an open topic. A variety of waveform optimization techniques have been studied over the years, leading to the definition of two big categories of MIMO radar signalling techniques: *element-space* (*ES*) and *beam-space* (*BS*) [43].

The element-space MIMO radar is based on the transmission of a number of orthogonal waveforms which is equal to the number of transmitter elements. In this case, at each element of the receiver, a bank of matched filters is used to separate the contributions from all the transmitted waveforms.

On the other side, in beam-space MIMO radar a number of orthogonal beams simultaneously used to focus the energy in different regions of the space. The beams formation is achieved by properly adjusting the degree of correlation of the transmitted waveforms. Also in this case a bank of matched filters is used at each element of the receiver, but each matched filter corresponds to a different beam.

## 2.3 HF-MIMO radar

The applicability of MIMO technology to OTH skywave radars has drawn the attention of the radar community during the last decade.

The advantages than can be achieved have been investigated and tested for a number of applications such as target signature simplification, coordinate registration, clutter mitigation, radar sensitivity enhancement and extension of the coverage area [44].

A detailed overview of the capabilities of HF-MIMO radar is in the next section.

### 2.3.1 HF-MIMO radar: capabilities & issues

In Sect.2.1.3 OTH radars have been presented as an efficient and low-cost solution for the surveillance of wide areas.

The dispersive nature of the ionosphere, its spatial non-homogeneity and temporal non-stationarity are at the basis of the limitations in the system performance. MIMO technology has been suggested as an effective solution to overcome a number of issues typical of OTH skywave radar.

In particular, in [45] MIMO technology was presented as a viable technique for spread Doppler clutter suppression via advanced adaptive processing algorithms that would be complex to implement in radar with higher data volume than in OTH skywave radar.

The problem of applicability of MIMO technology to OTH radar has been widely investigated, in particular [46] the HILOW (*HIgh frequency L-shaped Orthogonal Waveform*) experimental program undertaken by DSTO during the period 2006-2007.

In particular, it has been suggested that MIMO technology may offer advantages in OTH applications for spread Doppler clutter suppression, the introduction of spatial directivity in the radar management subsystem and the efficient use of radar resources by implementing radar-management trade-offs between radar sensitivity and surveillance footprint coverage.

## Spread Doppler clutter suppression

As mentioned in Sect.2.1.3, spread Doppler clutter is the phenomenon arising when the target return cannot be distinguished by the clutter return due to signal degradation. The application of techniques for co-channel interference and noise mitigation, usually employed by conventional OTH radars, are not always effective for spread Doppler clutter suppression.

A possible solution is given by the use of an adaptive filter which processes the information about the ionospheric channel to properly adjust the transmit beam-pattern and avoid the illumination of regions in which the clutter is stronger. Such a solution relies on the information about the ionospheric channel gathered via receiver feedbacks. The main issue is that it may happen that channels variations may occur during the feedback transmission, so that the information about the channel is no longer useful.

The use of orthogonal waveforms (or equivalently beams) typical of MIMO radars is an effective alternative to avoid the use of delayed and causal filters to iteratively adapt the waveform parameters according to the ionospheric channel state [47].

## Spatial directivity

In the beamspace solution (Sect.2.2.2), the correlation between the transmitted waveforms can be set in order to obtain a set of transmitted beams that simultaneously illuminate various regions of the surveillance area. This solution can be exploited to extend the surveillance coverage area or the illumination rate.

## Sensitivity penalty

Adaptive transmit beamforming for clutter suppression, extension of the surveillance area with a number of beams formed simultaneously and the introduction of

spatial directivity into the radar management support sub-system can be achieved. In this regard, it is useful to understand whether these advantages come at the expense of a reduced radar sensitivity.

In order to do so, let consider a MISO (*Multiple Input Single Output*) system with  $N_{tx}$  transmitter elements and a single receiver. When conventional transmit beamforming is applied<sup>2</sup>, the SNR is proportional to  $N_{tx}^2$ . On the other hand, when conventional transmit beamforming is applied, only an area proportional to  $\frac{1}{N_{tx}}$  of the whole angular coverage area that can be illuminated when orthogonal waveforms are transmitted by omnidirectional array elements is under surveillance. In order to cover an equivalent angular coverage region,  $N_{tx}$  beams must be formed so that the actual SNR is scaled by a factor  $N_{tx}$ , leading to an SNR proportional to  $N_{tx}$ . Consider now a MISO system, in which no transmit beamforming is applied. In this case, the whole angular surveillance area is illuminated at the same time, so that the useful signal power is proportional to  $N_{tx}^2$  at the output of a bank of matched filters at the receiver. But at the output of the same bank of matched filters, a noise contribution equal to  $N_{tx}$  must be considered so that the  $SNR_{MISO} = N_{tx}$ . In the MIMO case, a bank of matched filters is used at each of the  $N_{rx}$  receiver elements, so that SNR reduction (by a factor equal to  $N_{rx}$ ) must be considered in both cases, when orthogonal waveforms are used and when conventional transmit beamforming is applied.

It is then clear that the sensitivity of MIMO radars is the same of their phased array counterpart when the same angular surveillance area is considered.

## HF-MIMO waveforms

The selection of the transmitted waveforms in HF-MIMO must comply with the constraints imposed by the ionosphere, as well as the requirement of orthogonality (or specific correlation requirement in the beamspace solution) typical of the

---

<sup>2</sup>Under the hypothesis of zero propagation loss, unit target RCS, unit transmit element power and gain, and the transmitter beam steered toward the target.

MIMO configuration.

Orthogonality can be difficult to achieve because of the interaction between array elements in both transmit and receive systems. [48].

Moreover, the waveform/beam orthogonality is fundamental for the effectiveness of MIMO technology, since the receiver processing is based on the separation of the transmitted waveforms/beams via matched filters. Furthermore, signal corruption due to ionospheric propagation can be so strong so that it also affects orthogonality. With a loss of orthogonality, the matched filters at the receiver are not able to properly separate all the contributions with consequences for radar performance.

For the same reason, it may also happen that fading experienced by some of the signal contributions is so strong that the receiver is not able to detect them. In this case, the loss of those contributions coincides with the loss of the corresponding elements in the virtual array, as it will be better explained in the following chapters.

## Multiple propagation in HF-MIMO radars

Multiple propagation is responsible for multipath fading in OTH skywave radar as shown in 2.1.3, since all the contributions arriving at the receiver with different time delays might interfere constructively or destructively. It has been suggested, and it will be demonstrated in the present work, that MIMO configuration takes advantage of such contribution *diversity* at the receiver for detection purposes.

## 2.4 Summary

In this chapter an overview of the advantages and disadvantages related to OTH, MIMO and HF-MIMO radars has been presented. The objective is to understand how the MIMO technology applied to OTH radar can solve issues that are typical of OTH systems and what the additional constraints are for the design of HF-MIMO radar with respect to conventional OTH skywave systems.

First of all, a review of OTH radar has been presented (Sect.2.1.3). The ionospheric reflection mechanism has been recalled in order to understand how the ionosphere interacts with the propagating signals. It has been clearly underlined that the unstable nature of the ionosphere is one of the main cause of signal corruption and distortions that must be accounted in the design of OTH skywave radars. Then, MIMO radar has been described, with a special attention to the advantages that the waveform orthogonality can offer.

At the end, HF-MIMO radars have been considered and the main issues investigated. It has been seen that MIMO technology can be used for spread Doppler clutter mitigation and that multipath propagation can be exploited for detection purposes. The advantages related to the use of orthogonal waveforms, however, come at the expense of additional constraints on the waveform design.

Moreover, MIMO radars rely on the assumption that the transmitted waveforms can be separated at the receiver to exploit the information of each transmitted waveform. Such an assumption is not always true when signals propagate through the ionosphere. In this case, the corruption of the transmitted waveforms can be so strong so that orthogonality may be affected and the separation at the receiver can fail with consequences on the radar performance.

This chapter has demonstrated that signal design is an important task in the design of HF-MIMO radar. Consequently, we shall look at the following questions in the next chapter

1. *How is the signal generated?*
2. *How is the signal demodulated?*

# Chapter 3

## HF MIMO radar: Signal Modulation & Demodulation

In Ch.2 it has been shown that the waveform selection plays a fundamental rule in HF-MIMO radar. In particular, since MIMO technology relies on the orthogonality of the transmitted waveforms (or beams), this chapter will focus on how the set of transmitted signals can be selected and how they are separated at the receiver. In order to do that, the HF-MIMO radar simulator which is the core idea of the present work will be described, with a special attention to the blocks dedicated to the signal generation and demodulation.

At the end, a critical analysis of the constraints and the limitations which must be accounted in the waveform parameters selection will be provided.

### 3.1 HF MIMO radar simulator

In Ch.2 the advantages of the MIMO technology applied to HF skywave radars has been investigated. As stated in Ch.1, the core idea of the present work is the development of an HF MIMO simulator able to simulate both the radar system

(transmitter and receiver systems) and the propagation channel. In order to understand the key aspects to be considered in the design of such a simulator, it is useful to briefly recall how an HF MIMO radar works.

The functioning of an HF MIMO radar can be simply explained by considering Fig.3.1. A number of transmitter elements emit a set of linearly independent waveforms which propagate through the ionosphere. Effects such as losses, phase shift spread Doppler etc. corrupt the signals during the propagation with consequences on their properties. At the receiver, each element processes all the replica of the transmitted waveforms with the aim of separating the contributions and detect the presence of any target.

This process relies on the separability of all the contributions at the receiver, so that a simulator is a useful tool to study the way the propagation channel, i.e., the ionosphere, changes the orthogonality properties of the transmitted waveforms preventing the correct separation to be performed.

This simple explanation of the basic principle of an HF MIMO radar leads to the construction of an high level block diagram of the simulator, which consist of three main blocks (Fig.3.2)

1. transmitter/waveforms generator, which has the aim of selecting the transmitted waveforms
2. ionospheric channel simulator, which has the aim of simulating the propagation of the signal through the ionosphere
3. receiver, which has the aim of separating the transmitted waveforms for further signal processing.

The transmitter block takes into account the geometry of the transmitter and generates a number of waveforms equal to the number of transmitter elements,  $N_{tx}$ , i.e.,  $\{x_m(t)\}_{m=1}^{N_{tx}}$ , which propagate through the ionosphere.

The propagation channel simulator emulates the ionospheric structure and evaluates the path of the signals through it in order to estimate the effects according

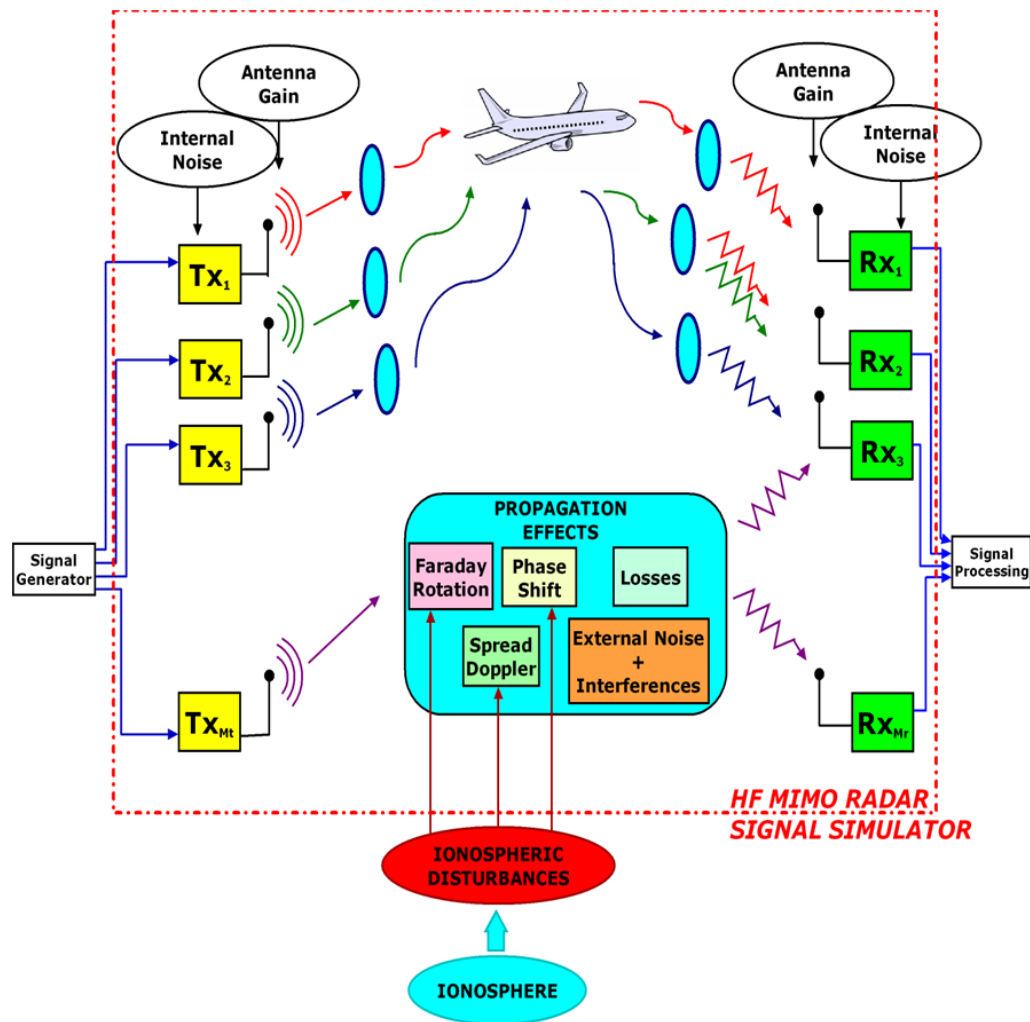


FIGURE 3.1: Representation of the ionospheric propagation and HF MIMO radar simulator

to the ionosphere state. Ionospheric propagation is a very complex process, which deserves to be treated separately in order to explain how the physics of the ionosphere interacts with the propagating signals. For this reason, the propagation channel block will be described in the next chapter.

Suppose that all the transmitted signal propagate through the ionosphere towards the receiver site. Under this assumption, the input of the receiver is a set of waveforms,  $\{z_m(t)\}_{m=1}^{N_{tx}}$ , associated to each signal emitted by all the transmitter elements. The objective of the receiver is that of separating all these contributions in order to fully exploit the advantages of the waveform diversity.

It is worth pointing out that the separation is performed at each of the  $N_{rx}$  receiver elements, so that a number of  $N_{tx}N_{rx}$  signals is theoretically available for

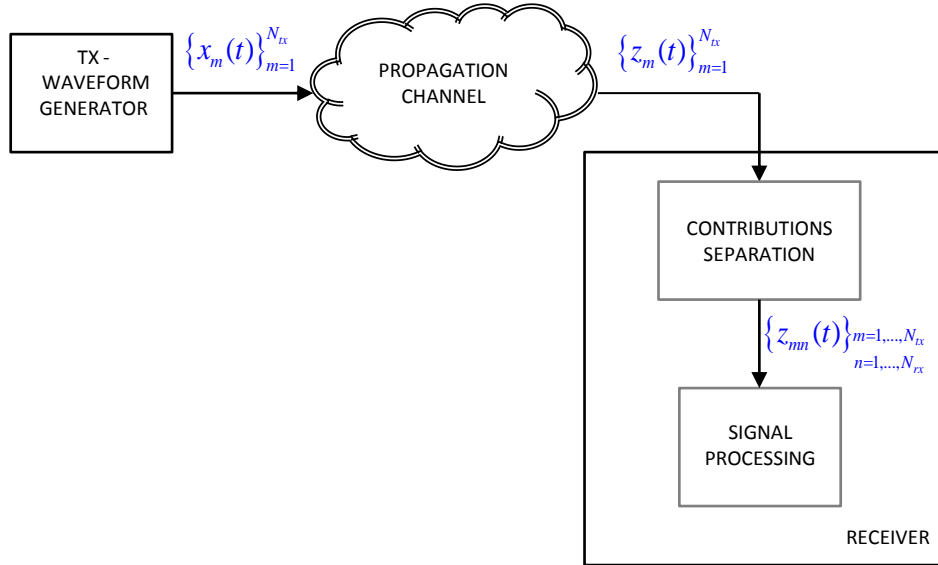


FIGURE 3.2: High level block diagram of the HF-MIMO radar signal simulator

further processing. In a real case, as it will be explained in the next chapter, it might happen that not all the contributions are available at the receiver input due to very high attenuation factors associated to the propagation through the ionosphere. The effects due to this lack of signals will be shown in the chapter dedicated to the simulation results.

It is clear that each of the main blocks in the HF MIMO simulator is a complex system that deserves to be described in details in order to understand what the critical issues are in the design of such a radar.

The following sections will describe the transmitter and the receiver blocks in order to explain the details about the modulation and the demodulation processes, while the ionospheric channel simulator block will be described in the next chapter.

### 3.1.1 The transmitter block

The flexibility offered by the transmission of multiple adjustable waveforms increases the degrees of freedom in the system design that can be used to optimized a desired performance criterion, for example the number of targets that can be

uniquely identified by the radar, or the sidelobe level in the beampattern, as shown in [36].

Fig.3.2 clearly shows that the main objective of the transmitter is to determine the waveform that is emitted by each element of the transmitter, i.e.,  $\{x_m(t)\}_{m=1}^{N_{tx}}$ . This waveform set must comply to all the requirements typical of HF skywave radars as well as the constraints that are typical of MIMO radars, such as waveform orthogonality. The waveform generator embedded in the transmitter block becomes then extremely important since from the correct selection of the transmitted waveforms depends the functioning of the whole radar system.

### 3.1.1.1 Waveform generator

#### **The signalling technique: Element Space or Beam Space**

From Ch.2 it is clear that waveform diversity is fundamental for HF MIMO radars in order to exploit all the processing that is otherwise not possible with conventional phased arrays.

The aspects that the waveforms generator must account for can be summarized in the following classes

- signalling technique, which defines the relationship among the waveforms in the set
- type of waveform, which is selected in order to best suit the application the radar is designed for
- the conventional HF radar requirements, such as range resolution, surveillance area scanning time, etc.

On regard of the signalling technique, two different classes of MIMO radars can be defined according to the way the transmitted waveforms are selected, namely the *element space* (ES) and the *beam space* (BS).

The element space signalling technique refers to the transmission of a number of orthogonal waveforms which is equal to the number of transmitter elements. Let  $x_m(t) = m_m(t)$  for  $m = 1, 2, \dots, N_{tx}$  be the waveform emitted by the  $m^{th}$  transmitter element. The orthogonality among the transmitted waveforms can be expressed considering the cross correlation among the various transmitted waveforms,

$$\int m_i(t)m_j(t)dt = \delta_{ij} \quad (3.1)$$

where

$$\delta_{ij} = \begin{cases} 1 & \text{if } i = j \\ 0 & \text{if } i \neq j \end{cases} \quad (3.2)$$

It is important to say that Eq.(3.1) does not account for the effects associated to time shifted waveforms. In other words, the interferences associated with side-lobes of the range-angle ambiguity function related to adjacent cells are neglected in the present work as the aim is that of understanding the ionospheric effects on propagating signals. Notwithstanding, the effects of such interference are usually more severe than noise and ionospheric disturbances and play an important role in the design of the transmitted waveforms. For this reason, further research must be pursued on this topic in order to find a suitable model for the interferences and include their effects in the simulator.

Different methods have been exploited in order to reach the orthogonality between waveforms. In particular, in [37] an overview of the most common techniques used to achieve orthogonality in FMCW MIMO radars is presented.

The orthogonality can be achieved in the time domain by transmitting different waveforms at different time instants, in the frequency domain by transmitting waveforms that are not overlapped in frequency or in the code domain by transmitting waveforms properly modulated using codes.

The first case, when time multiplexing is used, is the simplest way to achieve waveform orthogonality, but it is not appropriate when multiple pulses are required to be transmitted by all the elements since the PRF (*Pulse Repetition Frequency*) is reduced.

When the orthogonality is achieved in the frequency domain, the signals overlap

in time, but the transmission is performed on different bandwidths so that in this case a large spectral region is required to be sampled for simultaneous reception. In the last case, the signals overlap both in frequency and time domain, since the orthogonality is achieved through the use of codes.

A representation of the element space signalling technique is given in Fig.3.3 where  $x_m(t)$  represents the waveform emitted by the  $m^{th}$  transmitter, which is orthogonal to the other transmitted waveforms in the same set.

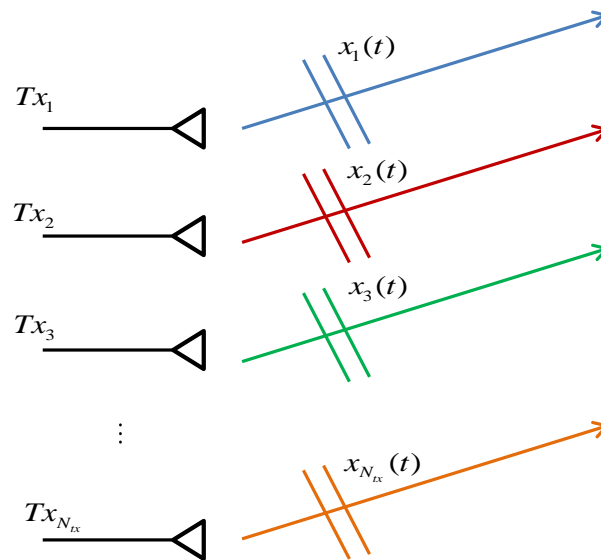


FIGURE 3.3: Representation of the element space signalling technique. Each transmitter element emits a waveform orthogonal to the waveforms emitted by the other elements of the transmitter.

In the beam space case, a degree of correlation between the transmitted waveforms is admitted in order to focus the transmitted energy in specific directions.

The degree of correlation is obtained by linearly combining a number of linearly independent waveforms before transmission, so that this technique can be seen as a variation of the element space technique.

A schematic representation of the beam space signalling technique is given in Fig.3.4, in which  $\beta_i$  denotes the direction in which the  $i^{th}$  beam is formed. The number of beams,  $N_B$ , which can be up to the number of transmitter elements,  $N_{tx}$ .

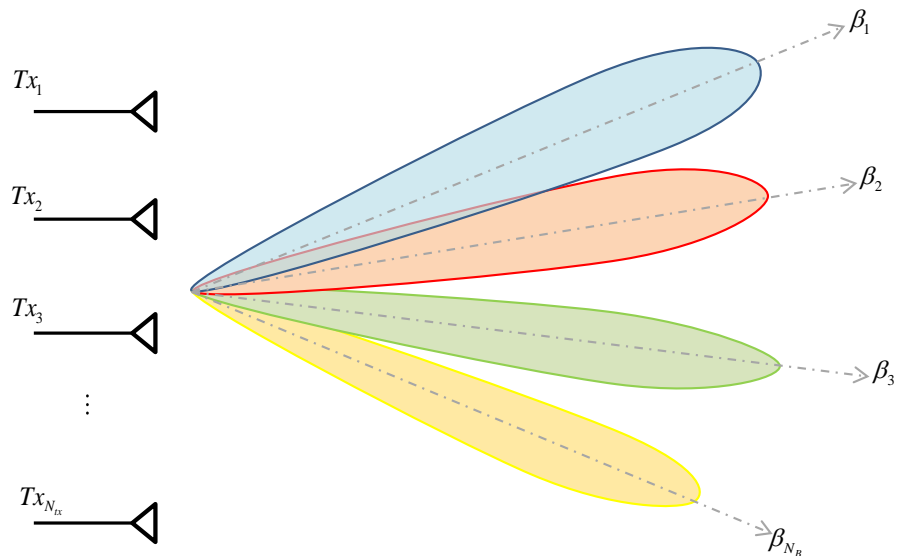


FIGURE 3.4: Representation of the beam space signalling technique. A number of orthogonal beams is synthesized by properly adjusting the waveforms weights.

In particular, in order to generate  $N_B$  beams in directions given by  $\beta_i$ , where  $i = 1, 2, \dots, N_B$ , a number  $N_B$  independent waveforms is linearly combined in order to create  $N_{tx}$  waveforms that focus the energy in the specified directions. Specifically, let  $\{m_i(t)\}_{i=1}^{N_B}$  and  $\{\beta_i\}_{i=1}^{N_B}$  the set of linearly independent waveforms and the set of beam directions respectively. Then, the set of transmitted waveforms  $\{x_m(t)\}_{m=1}^{N_{tx}}$  is given by

$$\begin{bmatrix} x_1(t) \\ x_2(t) \\ \vdots \\ x_{N_{tx}}(t) \end{bmatrix} = \begin{bmatrix} \beta_1 & \beta_2 & \cdots & \beta_{N_B} \end{bmatrix} \begin{bmatrix} m_1(t) \\ m_2(t) \\ \vdots \\ m_{N_B}(t) \end{bmatrix} \quad (3.3)$$

where  $[\beta_1 \beta_2 \cdots \beta_{N_B}]$  is an  $N_{tx} \times N_B$  matrix which defines the directions of the beams [43].

A different way to obtain a similar result is based on the fact that the power associated to the transmitted signals at a generic focal point with location given by  $\theta$  can be written as

$$P(\boldsymbol{\theta}) = \mathbf{a}^*(\boldsymbol{\theta})\mathbf{R}\mathbf{a}(\boldsymbol{\theta}) \quad (3.4)$$

where  $\mathbf{a}(\boldsymbol{\theta})$  is the steering vector accounting for the delays from the transmitter to the focal point considered and  $\mathbf{R}$  is the covariance matrix of the transmitted waveforms, given by

$$\mathbf{R} = E \{x(n)x^*(n)\} \quad (3.5)$$

where  $x(n)$  is the discrete-time version of  $x(t)$ .

It is clear that a set of waveforms can be found such that Eq.(3.4) is satisfied. In particular, the expression of the correlation matrix  $\mathbf{R}$  that allows for a specific  $P(\boldsymbol{\theta})$  to be achieved can be evaluated. A number of ways have been identified in literature for the design of the covariance matrix, in order to find the optimum solution that best fits the desired  $P(\boldsymbol{\theta})$ , and they can be classified in two groups

- methods that aim at finding  $\mathbf{R}$  which maximize the power in specific locations
- methods that aim at approximating a desired beampattern.

Once  $\mathbf{R}$  has been defined, the problem is to find the set of waveforms such that their correlation matrix is equal to  $\mathbf{R}$ . A way to solve such a complex problem is given in [40], in which the authors suggest to set

$$x(n) = \mathbf{R}^{1/2}\mathbf{w}(n) \quad (3.6)$$

where  $\mathbf{R}^{1/2}$  denotes the square root of the correlation matrix  $\mathbf{R}$  and  $\{\mathbf{w}(n)\}$  is a set of  $N_{tx}$  i.i.d. random vectors with zero mean and covariance matrix equal to the identity matrix  $\mathbf{I}$ . Anyway, this is still an open topic for MIMO radar. In [49] a different way to select a set of waveforms with a given covariance matrix is presented. It is worth noting that in the BS case, the orthogonality is achieved in

the space domain among all the beams created by properly adjusting the degree of correlation among the waveforms.

### Waveform type

Considering the waveform type, it is clear that a signal that best suits the application the radar is designed for must be selected. In case of OTH skywave radar, the most used waveform is the LFM-CW. The advantages of the use of LFM-CW waveforms have been investigated in [50], in which this type of waveform is shown to have good low probability of intercept properties. Moreover, LFM-CW waveforms has been proven to have attractive properties also for HF MIMO radar [45]. Moreover, the demodulation can be easily performed by using solid state transmitters. The use of orthogonal LFM-CW waveforms has been studied in literature for HF MIMO in [51], where the way to select a set of orthogonal waveforms has been shown. In particular, the orthogonality can be achieved by properly selecting a time or a Doppler offset among the waveforms in the set. The details about the time and Doppler offset selection to reach orthogonality will be given in Sec.3.2.1. The generic LFM-CW signal can be written as

$$x_m(t) = \begin{cases} \alpha \exp \left\{ j2\pi \left( f_0 t + \gamma \frac{t^2}{2} \right) \right\} & , t \in [0, \dots, T_{sw}] \\ 0 & otherwise \end{cases} \quad (3.7)$$

where

- $\alpha$  is the signal amplitude
- $f_0$  is the carrier frequency
- $\gamma$  is the chirp rate. It is related to the signal bandwidth,  $B$ , and to the sweep pulse time,  $T_{sw}$  as in the following relationship  $\gamma = \frac{B}{T_{sw}}$ .
- $T_{sw}$  is the ramp duration which is usually less or equal to the repetition period,  $T_{rep}$ , ( $T_{sw} \leq T_{rep}$ ).

An accurate selection of the aforementioned waveform parameters is fundamental to achieve the desired radar performances. This is particularly true when talking about HF MIMO, in which  $N_{tx}$  waveforms must be identified for transmission, each with its own parameters in order to achieve the desired degree of orthogonality. The issues related to the waveform parameters selection will be analyzed at the end of this chapter.

It is worth saying that in [45][51], the use of noiselike waveforms in HF MIMO radar is discussed. This type of signals are so widely used in conventional MIMO radars that they are usually referred as *noise MIMO radar*. When noiselike waveforms are used, the orthogonality is reached by selecting a number of i.i.d. noise sources equal to the number of transmitter elements. In the same paper, the authors analyze the problem of the reactive power, which is the power that remains near the transmitter, showing that noiselike waveforms are not suitable for HF-MIMO radar.

## 3.2 The receiver block

The receiver is the last block of the HF MIMO simulator proposed in the present thesis. In order to fully exploit the advantages associated to the transmission of orthogonal waveforms/beams, all the contributions must be separated and properly processed.

The signal at the input of the  $n^{th}$  element of the receiver,  $z_n(t)$  is given by the superimposition of all the contributions associated to the signals emitted by all the elements of the transmitter. Let  $\{z_m(t)\}_{m=0}^{N_{tx}}$  denote all these contributions. Each  $z_m(t)$  is a delayed and attenuated replica of the signal transmitted by the elements of the transmitter, i.e.,

$$z_m(t) = C_{att}x_m(t - \tau) \quad (3.8)$$

where  $C_{att}$  is a constant accounting for all the attenuations and losses undergone by the signal during the propagation and  $\tau$  is the propagation delay. Details about how the signal is attenuated will be given in the next chapter.

The separation process at the receiver is usually implemented at each element of the receiver by means of a bank of matched filters (MF) properly matched to the transmitted waveforms/beams according to the signalling technique used. A representation of this kind of receiver is in Fig.3.5.

Let suppose to consider the ES signalling technique. In this case, the matched filter is designed to match the transmitted waveforms so that the output of the  $k^{th}$  matched filter at the  $n^{th}$  receiver element can be written as

$$z_{Tn,k}(t) = \int_{-\infty}^{+\infty} z_n(t)x_k^*(t - \tau)dt \quad (3.9)$$

When all the incoming contributions are perfectly separated at each element of the receiver,  $N_{tx}N_{rx}$  signals are available for further processing, such as conventional beamforming [52], as shown in Fig.3.5.

When LFM-CW waveforms are used, the same operation can be performed via *deramping* process. This operation consists of a multiplication of the received signal with a replica of the transmitted waveform and it is performed for each transmitted waveform at each receiver element, as shown in Fig.3.6.

The output of the deramping process at the  $n^{th}$  receiver with respect to the  $k^{th}$  transmitted waveform can be written as

$$z_{Tn,k}(t) = z_n(t)x_k^*(t) \quad (3.10)$$

where  $z_{Tn,k}(t)$  is also called *beat signal*, which is a single tone at a frequency, the *beat frequency*, which depends on the propagation delay. In fact, suppose to transmit a single LFM-CW waveform

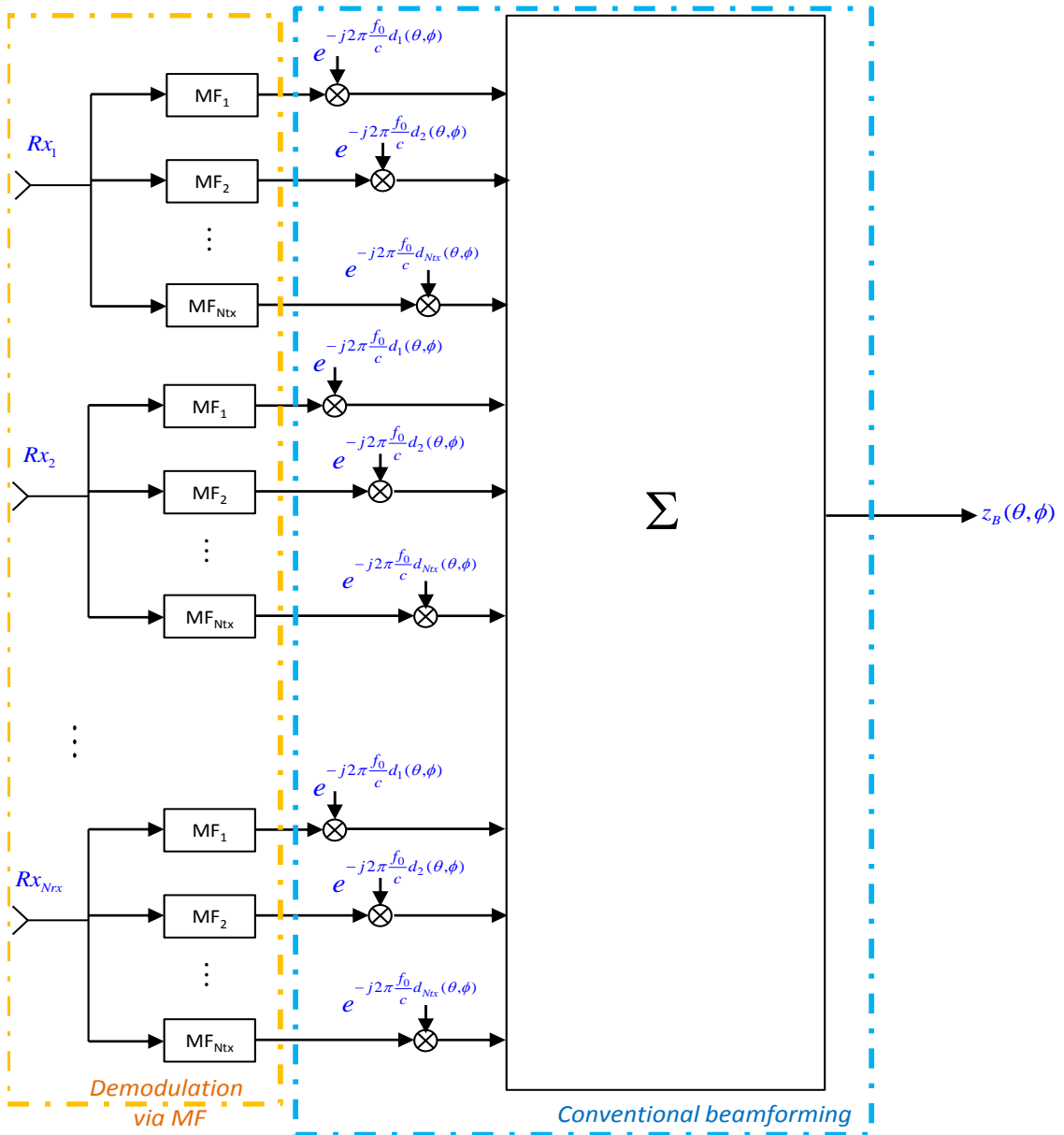


FIGURE 3.5: High level block diagram of the receiver for ES signalling technique

$$x_1(t) = \alpha \exp\left\{j2\pi \left[f_0 t + \frac{\gamma}{2} t^2\right]\right\} \quad (3.11)$$

after propagation, the receiver input will be an attenuated and delayed version of  $x_1(t)$

$$z_1(t) = C_{att} x_1(t - \tau) \quad (3.12)$$

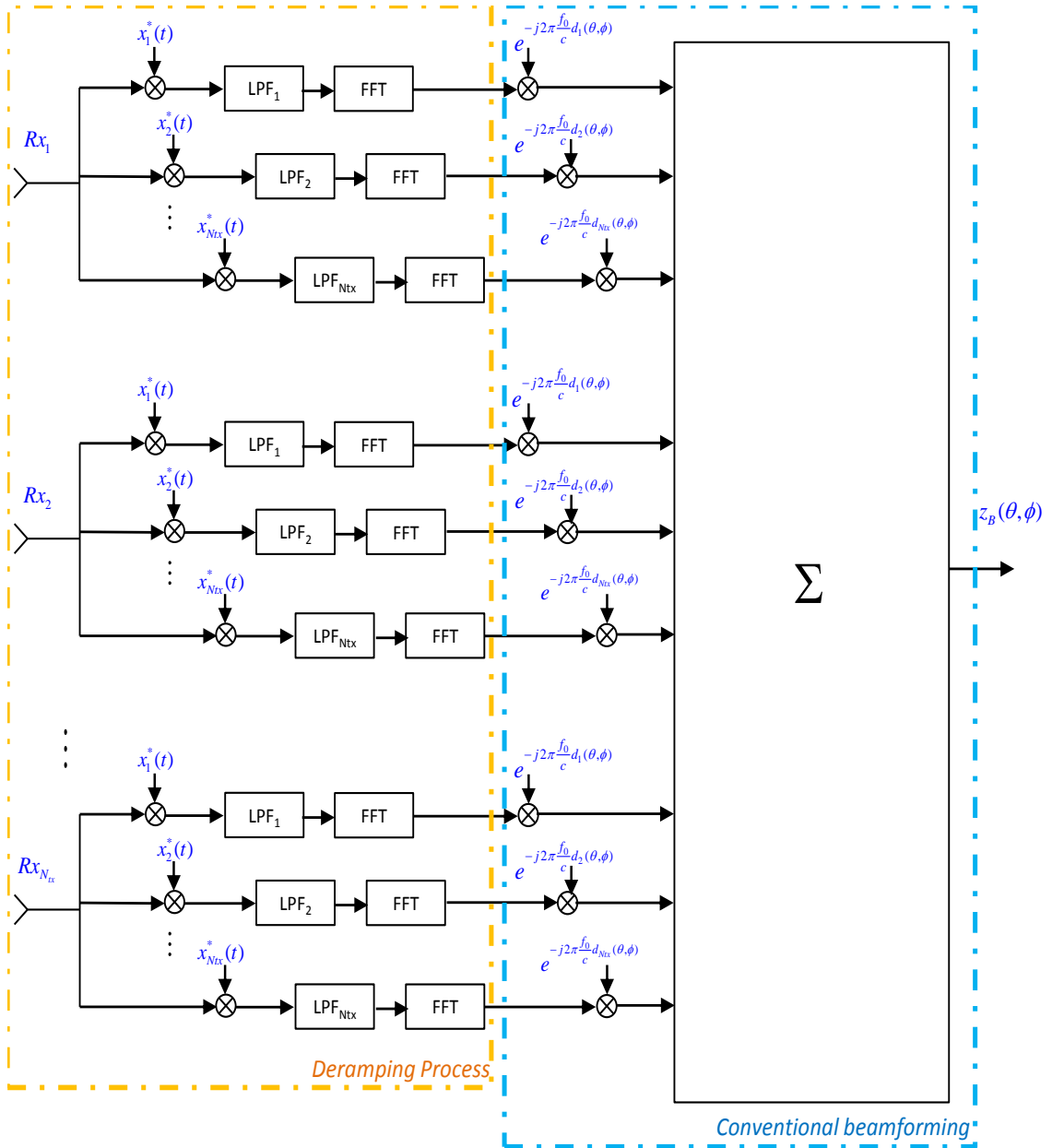


FIGURE 3.6: High level block diagram of the receiver for ES signalling technique via deramping

and the output of the deramping process is

$$z_1(t)x_1^*(t) = C_{att}\alpha^2 \exp\left\{j2\pi \left[-f_0\tau + \frac{\gamma}{2}\tau^2 - \gamma\tau t\right]\right\} \quad (3.13)$$

which can be associated to a single tone signal at the beat frequency, given by  $f_{beat} = \gamma\tau$ , with a fixed phase term depending on the carrier frequency and a term

depending on the chirprate and the propagation delay which is known as *Residual Video Phase* (RVP), which is a term to be compensated before further processing. At this point, in fact, a LPF (*Low Pass Filter*) is used to separate the contributions associated to different propagation delays, i.e., different frequencies.

In fact, assume that the transmitted waveforms can be written as

$$x_m(t) = \alpha_m \exp\left\{j2\pi \left[ f_0 (t - (m - 1)\tau_{off}) + \frac{\gamma}{2} (t - (m - 1)\tau_{off})^2 \right] \right\} \quad (3.14)$$

where  $t \in [(m - 1)\tau_{off}, (m - 1)\tau_{off} + T_{sw}]$ ,  $m = 1, 2, \dots, N_{tx}$  and

- $f_0$  is the carrier frequency
- $\tau_{off}$  is the offset between the transmitted waveforms which is set in order to obtain orthogonality
- $\gamma$  is the chirprate
- $T_{sw}$  is the ramp duration.

The signal at the  $n^{th}$  receiver is given by a replica of the transmitted one, after a propagation delay  $\tau_{p,mn}$ , where  $m$  denotes the transmitter element and  $n$  the receiver element

$$z_m(t) = \alpha_{mn} \exp\left\{j2\pi \left[ f_0 (t - (m - 1)\tau_{off} + \tau_{p,mn}) + \frac{\gamma}{2} (t - (m - 1)\tau_{off} + \tau_{p,mn})^2 \right] \right\} \quad (3.15)$$

where  $\alpha_{mn}$  is the factor which accounts for the attenuation due to ionospheric propagation in the path from the  $m^{th}$  transmitter element to the  $n^{th}$  receiver element.

The output of the demodulation with the  $k^{th}$  transmitted signal is

$$\begin{aligned}
z_{Tn,k}(t) = & \exp \left\{ j2\pi \left[ f_0 (\tau_{p,mn} - \tau_{off} (m - d)) + \frac{\gamma}{2} (\tau_{p,mn} - \tau_{off} (m - d)) 2t \right] \right\} \times \\
& \times \exp \left\{ j2\pi \left[ \frac{\gamma}{2} (\tau_{p,mn} - \tau_{off} (m - d)) (\tau_{p,mn} - \tau_{off} (m - d - 2)) \right] \right\}
\end{aligned} \tag{3.16}$$

From Eq.(3.2) is clear that the signal after demodulation consists of three factors

1. a phase factor depending on the carrier frequency,  $f_0$ , the time offset,  $\tau_{off}$  and the propagation delay,  $\tau_{p,mn}$
2. the beat frequency which depends on the time,  $t$ , the chirprate,  $\gamma$ , the time offset,  $\tau_{off}$  and the propagation delay,  $\tau_{p,mn}$ ,
3. a third factor ( $2^{nd}$  line) which is the *Residual Video Phase* (RVP)

From Eq.(3.2) it is clear that the output of the demodulation is given by a single tone at a frequency  $f_{out} = \gamma (\tau_{p,mn} - \tau_{off} (m - d))$ . The LPF which follows the demodulation is tuned at  $f_{out}$  with a bandwidth  $B_{LPF}$  evaluated in order to filter only the desired contribution and which depends on the maximum beat frequency,  $f_{beat,max}$ , associated to the maximum delay,  $\tau_{max}$ , obtained for the maximum observed range,  $R_{max}$ . As for the case of separation performed via matched filter, at the output if the deramping process  $N_{tx}N_{rx}$  signals are available for further processing.

### 3.2.1 Waveform parameters selection: issues

In Sec.3.1.1.1 the most used waveforms in HF MIMO radar has been introduced. In particular, LFM-CW waveforms have been introduced in order to show the parameters that can be set in order to achieve the desired degree of orthogonality and obtain the desired radar performance. The way these parameters should be set has been omitted in Sec.3.1.1.1 since it is a complex topic to be treated. The

problem will be treated in this section, with a special attention for the ES signalling technique and LFM-CW waveforms that will be used to test the simulator.

### 3.2.1.1 Frequency selection: the Frequency Management System

In Ch.2, the effects of the spatial and time variability of the ionosphere on the waveform parameters have been introduced. In particular, the dispersive nature of the ionosphere is responsible for the shortage of available and wide channels in which the transmission can be performed. Moreover, the variability of the electron density on a daily scale requires the selection of the carrier frequency to be performed as soon as the ionosphere undergoes substantial changes, in order to avoid the waves to cross the ionospheric layers without being reflected.

It is then clear that a system able to check the ionosphere state and select suitable waveform parameters, especially the carrier frequency, is essential for the correct functioning of an HF MIMO radar. Such a system is usually referred as *Frequency Management System* (FMS) and can be represented by the block diagram in Fig.3.7. The inputs of the FMS are data collected by a ionospheric check system about the ionospheric state according to the information about the surveillance area. The ionospheric check system can be based on a oblique and vertical sounder system which collects measurements about the ionospheric state or on a system which estimates the ionospheric state from the data in a database or considering a proper ionospheric model.

The information about the ionospheric state is used by the FMS to evaluate the optimum carrier frequency,  $\hat{f}_{opt}$ . In particular, a criterion is set that allows for the optimum frequency evaluation. In the Australian Jindalee radar [13], the optimum frequency is selected according to the maximum clutter-to-noise ratio (CNR), since the clutter is considered as a measure of the energy flux illuminating the target, i.e., the Earth's surface.

It is worth pointing out that the optimum frequency is evaluated each time that new ionospheric data are available. Once the optimum frequency is available, the

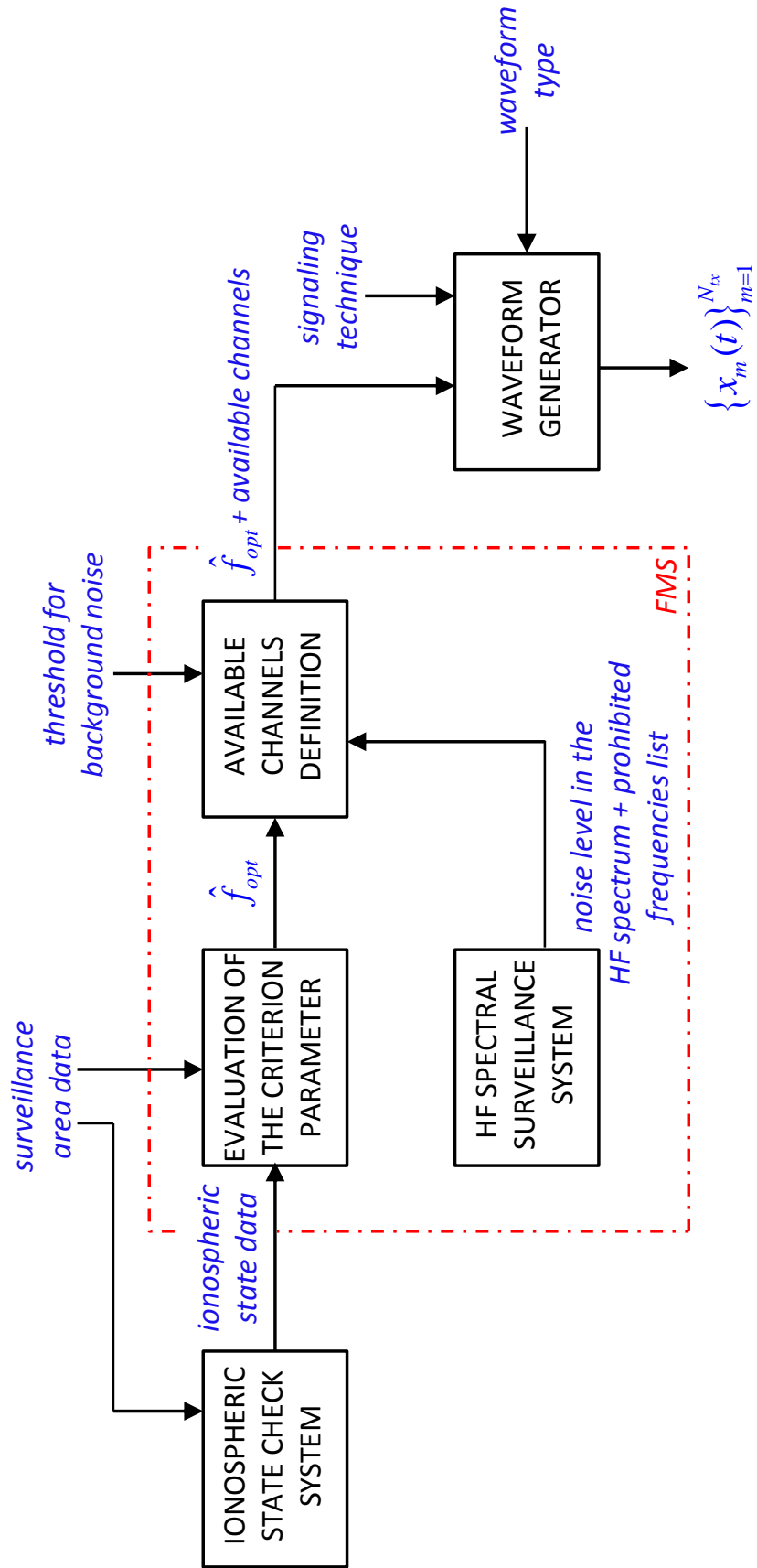


FIGURE 3.7: Representation of the Frequency Management System.

available channels around the optimum frequency must be identified. In this regard, a dedicated system analyses the HF spectral occupancy in order to evaluate the noise and interference level over the HF band. The same system accounts for a list of *prohibited* frequencies, which are usually dedicated to specific services, such as the international distress channels. The channels over which the transmission can be performed are selected among those in which the noise level is lower than a specific threshold. At this point, the optimum frequency and the available channels, from which the waveform bandwidth depends, are available as input for the waveform generator.

### 3.2.1.2 Waveform parameters selection

Suppose the optimum frequency,  $f_{opt}$ , and the available bandwidth,  $B_{av}$ , around  $f_{opt}$ , has been selected by the FMS. Suppose to transmit a set of orthogonal waveforms, i.e., to use the ES signalling technique. So, the set of transmitted waveform is

$$\mathbf{x}(t) = \begin{bmatrix} x_1(t) \\ x_2(t) \\ \vdots \\ x_{N_{tx}}(t) \end{bmatrix} \quad (3.17)$$

It has been shown that the most used waveform in HF MIMO is the LFM-CW waveform. So, suppose that each transmitted waveform is an LFM-CW waveform. The problem is now to understand how to select a set of *orthogonal* LFM-CW waveforms. In [51] it has been demonstrated that the orthogonality among LFM-CW waveforms can be achieved by properly setting a time offset, or a frequency Doppler offset, or a chirprate offset [37]. For HF MIMO radars, the most used technique to achieve orthogonality with LFM-CW via time offset, so let consider a set of transmitted waveforms given by

$$\mathbf{x}(t) = \begin{bmatrix} x_1(t) \\ x_2(t) \\ \vdots \\ x_{N_{tx}}(t) \end{bmatrix} = \begin{bmatrix} x_1(t) \\ x_1(t - \tau_{off}) \\ \vdots \\ x_1(t - (N_{tx} - 1)\tau_{off}) \end{bmatrix} \quad (3.18)$$

where  $x_1(t)$  is the conventional LFM-CW signal expressed in Eq.(3.11).

At the  $n^{th}$  element of the receiver, the received signal corresponding to the waveform transmitted by the  $m^{th}$  transmitter is given by

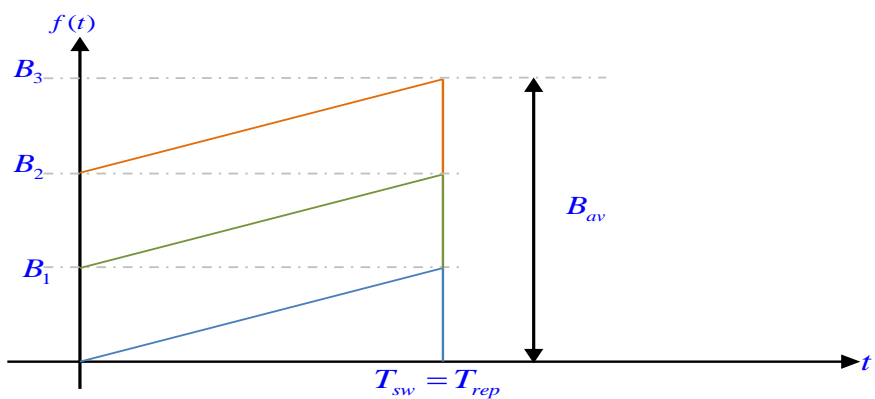
$$z_m(t) = C_{mn}\alpha_m \exp \left\{ j2\pi \left[ f_0 (t - (m - 1)\tau_{off} + \tau_{p,mn}) + \frac{\gamma}{2} (t - (m - 1)\tau_{off} + \tau_{p,mn})^2 \right] \right\} \quad (3.19)$$

where  $t \in [(m - 1)\tau_{off}, (m - 1)\tau_{off} + T_{sw}]$ .

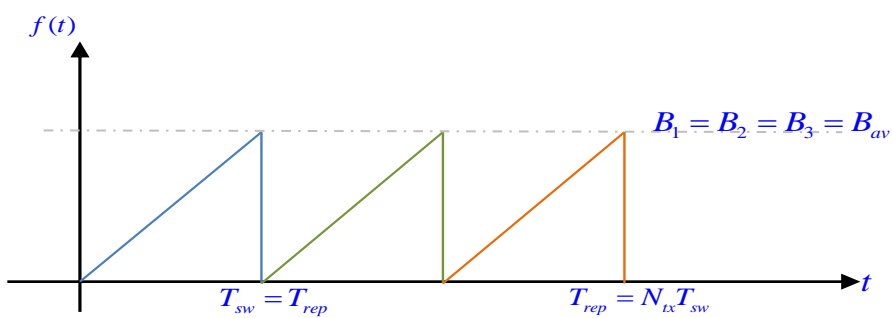
A representation of the frequency as a function of the time for LFM-CW waveforms is in Fig.3.8, where three different offset values are used to obtain different degrees of orthogonality.

In the first case (Fig.3.8(a)), various LFM-CW signals are transmitted at the same time, i.e.,  $\tau_{off} = 0$ , with the same ramp duration,  $T_{sw}$ . In this case, the orthogonality can be achieved in the frequency domain by transmitting the LFM-CW signals at different frequencies, i.e., with a proper Doppler offset. In this case, each channel occupies a portion of the available bandwidth supported by the ionosphere, which is of the order of tens of  $kHz$  and which defines the range resolution of the system. So, the number of transmitted waveforms does not affect the range resolution of the system.

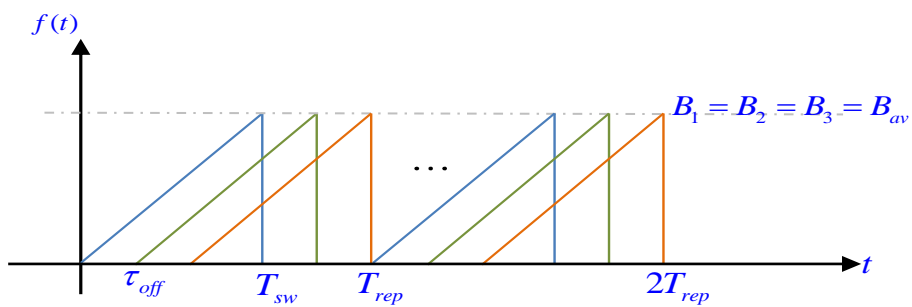
Another way to achieve orthogonality is by setting a time offset equal to the duration of the transmitted ramp,  $\tau_{off} = T_{sw}$ , as in Fig.3.8(b). In this way, time multiplexing is implemented and the orthogonality is achieved in the time domain so that all the transmitted signals can occupy the whole available bandwidth at different time. On the other hand, time division among the different transmitted



(a)



(b)



(c)

FIGURE 3.8: (a)  $\tau_{off} = 0$ ; (b)  $\tau_{off} = T_{sw}$  (c) nearly orthogonal LFM-CW.

waveforms leads to reduced PRF.

A third solution is given by the transmission of *nearly orthogonal* waveforms (Fig.3.8(c)) [53]. In this case, a small time offset is set on order to transmit delayed waveforms. The delay is not big enough to achieve time division and the waveforms occupy the same spectral region, so that they are orthogonal neither in the time domain nor in the frequency domain. In this case the transmitted waveforms can be called *nearly orthogonal* since they occupy different frequencies at different time instants. For the case of  $\tau_{off} = 0$  and  $\tau_{off} = T_{sw}$ , the separation at the receiver site can be performed via matched filter, since the various contributions are separated in the time domain and in the frequency domain respectively. In the third case, when  $0 < \tau_{off} < T_{sw}$ , it is quite obvious that at the receiver they cannot be separated via matched filter since they overlap in frequency as well as in time. An effective way to separate these waveforms is given by the *deramping* process, described in Sec.3.2. In fact, as shown in Sec.3.2, after demodulation the received signal is associated to a single tone with a frequency depending on the propagation delay and the chirprate.

The way the orthogonality is achieved has some drawbacks that should be considered when selected the waveforms parameters.

In the case of orthogonal waveforms in the frequency domain, i.e.,  $\tau_{off} = 0$  and frequency offset  $f_{off} \neq 0$ , it is clear that a way to fully exploit the available channel bandwidth is to set the bandwidth of each single transmitted waveform equal to

$$B_m = \frac{B_{av}}{N_{tx}} \quad (3.20)$$

where  $B_m$  is the bandwidth of the  $m^{th}$  transmitted signal,  $B_{av}$  is the bandwidth supported by the ionosphere at the time of transmission and  $N_{tx}$  is the number of transmitter elements.

At the receiver, all the contributions related to each transmitted waveform are properly separated and coherently processed, so that the ambiguity function is

reconstructed for all the frequencies within the available bandwidth,  $B_{av}$ , as shown in Fig.3.9. This implies that the range resolution is not affected by the number of transmitted waveforms,  $N_{tx}$ . On the other hand, when a specific frequency is associated to each different channel, the portion of ambiguity function associated to each channel is weighted by a different factor, so that the spectrum is not flat within  $B_{av}$ , as shown in Fig.3.9. As a consequence, the ambiguity function is not optimal and sidelobes appear in range.

In order to reduce these sidelobes, LFM stepped frequency transmitted waveforms can be used, as shown in Fig.3.10. In this way, the reconstructed ambiguity function is almost flat within  $B_{av}$  since each channel provide a contribution for each frequency value in the available bandwidth, as depicted in Fig.3.11.

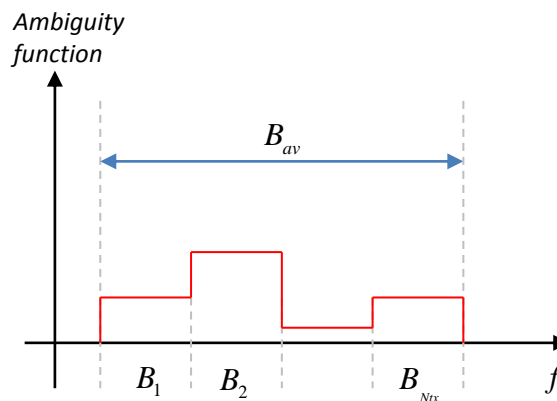


FIGURE 3.9: Schematic representation of the reconstructed ambiguity function when a single frequency is associated to each single transmitted waveform.

In the second case, Fig.3.8(b), each signal can be transmitted with a bandwidth equal to the available bandwidth,  $B_m = B_{av}$ , so that the range resolution is not reduced as the number of transmitted waveforms increases. However, a special attention should be given to the time length of the single waveforms, since

$$T_{rep} = \frac{1}{PRF} = T_{sw} N_{tx} \quad (3.21)$$

where the PRF defines the non ambiguous Doppler region and, hence, the target maximum detectable velocity.

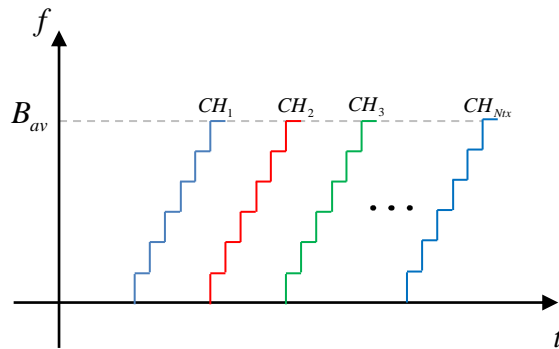


FIGURE 3.10: Schematic representation of LFM CW stepped frequency waveforms.

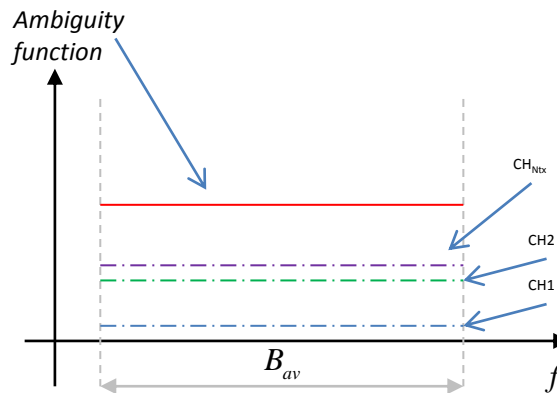


FIGURE 3.11: Schematic representation of the reconstructed ambiguity function when LFM CW stepped frequency transmitted waveforms are used.

The last case, Fig.3.8(c), corresponding to  $0 < \tau_{off} < T_{sw}$ , is quite different from the previous ones, so that similar conclusions cannot be drawn. First of all, considerations about the lower bound of the time offset should be drawn. In fact, the time offset must be greater than the maximum round trip delay,  $\tau_{max}$ . On the other hand, the duty cycle sets an upper bound so that the selection of the time offset should obey to the following relationship

$$\tau_{max} \leq \tau_{off} < \frac{T_{rep}}{N_{tx}} \quad (3.22)$$

In order to make an example, let consider a system in which  $PRF = \frac{1}{T_{rep}} = 4kHz$  which coincides with a non ambiguous detectable target radial velocity  $v_{r,max} =$

$30m/sec$ . The same PRF corresponds to a period  $T_{rep} = 250msec$  in which all the  $N_{tx}$  waveforms must be transmitted. Suppose to have a maximum range  $R_{max} = 3000km$  which corresponds to a maximum delay  $\tau_{max} = 20msec$ . Under these assumptions,  $20msec \leq \tau_{off} < \frac{250msec}{N_{tx}}$ . So, considering Eq.(3.22) it is clear that considering the fact that all the waveforms are transmitted within a period equal  $T_{rep}$  with a delay equal to  $\tau_{off}$ , the number of waveforms that can be transmitted is subject to the following limitation

$$N_w \leq \frac{T_{rep}}{\tau_{off}} \quad (3.23)$$

that leads to  $N_w = \frac{250msec}{20msec}$  that under the above mentioned assumptions is  $N_w = 12$ .

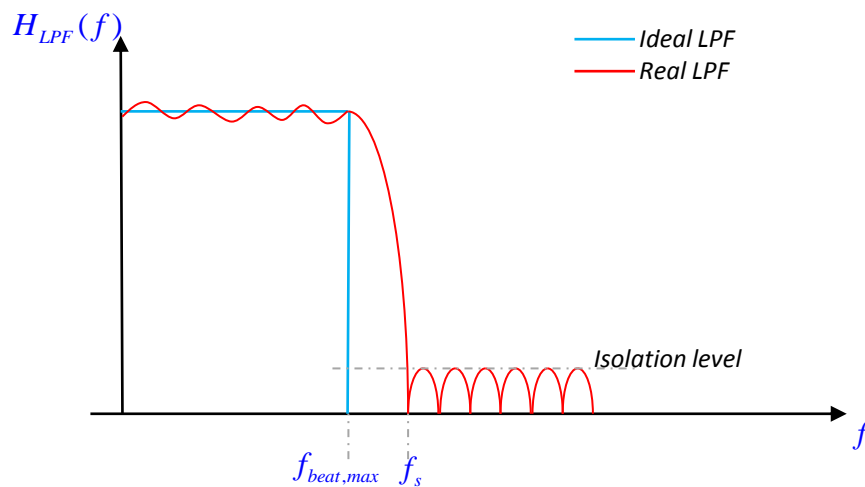


FIGURE 3.12: Ideal vs real LPF amplitude-frequency response function.

In regard of the level of orthogonality that can be achieved, it depends upon the level of separability that can be achieved at the receiver. In theory, an ideal LPF allows for an unlimited level of separability, i.e., orthogonality, as shown in Fig.3.12. In reality, a LPF is characterized by a guard bandwidth,  $B_g = f_s - f_{beat,max}$  and an isolation level, given by the amplitude of the response function of the LPF for  $f > f_s$ . As the guard bandwidth increases, the level of orthogonality

that can be achieved becomes larger. On the other hand, as  $B_g$  increases, the number of orthogonal waveforms that can be selected decreases

$$N_w \leq \frac{T_{rep}}{\left(\tau_{max} \frac{f_s}{f_{beat,max}}\right)} \quad (3.24)$$

It is then clear that the waveform selection, and especially the waveform parameters selection, is a crucial aspect to be addressed in the design of an HF MIMO radar.

### 3.3 Summary

In this chapter, the issues related to the waveform generation and demodulation have been investigated.

The simulator which is the core idea of the present thesis has been presented. The high level block diagram has been described, and three main blocks identified. The transmitter and the receiver blocks have been described while the propagation channel simulator block has been treated as a black box in order to focus the attention on the signal modulation and demodulation.

The key operations of the transmitter have been described and the issues related to the waveforms generation have been presented and analysed in order to find a possible solution. In particular, the most common used waveform in HF MIMO radars have been presented, with a special attention to the LFM-CW waveforms. Then the attention has been focused on the problem of the waveform parameters selection for orthogonal LFM-CW waveforms in order to understand the limitations and the constraints that must be considered in the design of an HF MIMO radar. A special attention has been dedicated to the problem of the carrier frequency selection which is tackled by the FMS. A block diagram of the FMS has been proposed in order to highlight the critical aspects that must be accounted for in the selection of the carrier frequency.

The receiver has been then described and the processing at the basis of the waveforms separation has been explained. Two different approaches have been described. The conventional matched filter based approach has been described as a general way to demodulate orthogonal waveforms in HF MIMO radars. Then, the deramping process has been presented as a valid alternative to demodulate LFM-CW waveforms. The consequences on the way the signals are demodulated on the design of the transmitted waveforms have then been analysed.

At the end, the issues related to the waveform parameters selection in order to obtain a set of orthogonal signals has been analysed. In this regard, LFM-CW waveforms have been considered and the concept of *nearly orthogonal* waveforms introduced.

All the consideration drawn in this chapter are based on the fact that the received signal after propagation through the ionosphere is an attenuated and delayed version of the transmitted one. This is not completely true as the ionosphere may introduce distortions that corrupt the transmitted waveforms, with consequences on the radar performance, as it will be shown in the next chapter.

# Chapter 4

## The ionosphere & its effects on propagating signals

In Ch.3 an HF MIMO simulator was described from both the transmitter and receiver perspective.

Both the waveform generation and separation processes were investigated in order to understand the issues that could be encountered in the design of an HF MIMO radar. In this regard, the signal at the receiver, after ionospheric propagation has been treated as combination of attenuated and delayed replicas of the transmitted signal.  $N_{tx}$  signals are available at each of the  $N_{rx}$  elements of the receiver input and, hence,  $N_{tx}N_{rx}$  signals are available for further processing after separation.

In reality, the variability of the ionospheric structure on both spatial and temporal scales can be so strong that the propagating signals will be attenuated and distorted such that they cannot be properly separated and detected at the receiver.

It is clear that an understanding of the ionospheric behaviour is fundamental in the design of an OTHR a system in order to properly set the radar parameters as a function of the prevailing ionosphere. Such a management system will maintain the desired system performance and help mitigate against ionospheric conditions. This chapter will focus on the effects that a signal undergoes during propagation through the ionosphere. For this reason, a description of the ionosphere from a physical point of view will be given, in order to understand the mechanisms that

can cause corruption. A brief review of the most common models used to predict the ionospheric behaviour will be given and the phenomena responsible for ionospheric irregularities will be described. At the end, special attention will be given to how the signal changes while propagating through the ionosphere from the transmitter to the receiver.

## 4.1 The ionosphere

The uppermost part of the Earth's atmosphere is characterized by the presence of free charged particles, in particular ions, and it is usually referred to as *ionosphere*. The refraction properties of the ionosphere have been widely exploited for communications purposes since Marconi's experiments on radio propagation at the end of the 19<sup>th</sup> century, but the first studies of the reflection of radio waves by the ionosphere were pursued in the early 1920s. The demonstration of the reflection of radio waves propagating through the ionosphere was provided almost simultaneously by Appleton and Barnett in England and Breit and Tuve in America [54] in 1924, when they investigated the use of nearly vertical radio waves as a tool for ionospheric investigation.

In the following years many studies were carried out in order to understand the morphology and variability of the ionosphere.

These investigations have led to the identification of a basically layered structure of the ionosphere and a number of anomalies and disturbances that it was subject to.

The following section will describe ionospheric morphology while Sec.4.1.3 will focus on the disturbances. The effects of such disturbances on propagating radio waves will be demonstrated in Sec.4.2.

### 4.1.1 Ionosphere structure

The presence of free ions is the result of the photo-ionization process that happens when the solar radiation interacts with the molecules in the ionosphere causing

the production of free electrons [10]. Since this depends on the incident solar radiation, the ionization process occurs during day while during night free electrons tend to recombine with ions forming uncharged atoms and leading to a depletion of the ionization.

The concentration of free electrons, i.e., electron density ( $n_e$ ), is closely related to the ability of the ionosphere to reflect radio waves in the HF band as shown in Eq.(2.2). In particular, as the electron density increases the plasma frequency,  $f_p$ , increases and so higher frequencies can be reflected by the ionosphere at higher altitudes allowing for the coverage of greater ground ranges. A representation of the plasma frequency values for different altitudes along a fixed bearing direction is in Fig.4.1. As it can be noticed, the value of plasma frequency increases as the altitude increases, meaning that at higher altitudes higher HF frequencies can be reflected by the ionosphere.

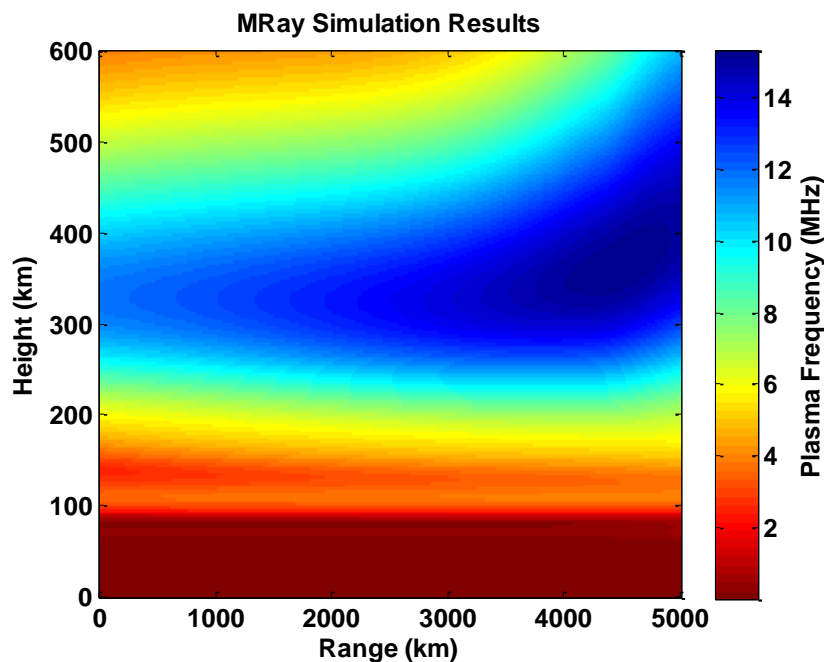


FIGURE 4.1: Representation of plasma frequency variations in altitude and range for a quiet ionosphere. Results are based on a Matlab routine created by C.J. Coleman.

The analysis of the electron density profiles in altitude for a fixed range in an unperturbed ionosphere show a trend that allows the identification of different layers with different physical characteristics, namely *D*, *E* and *F regions* [55], as

shown in Fig.4.2.

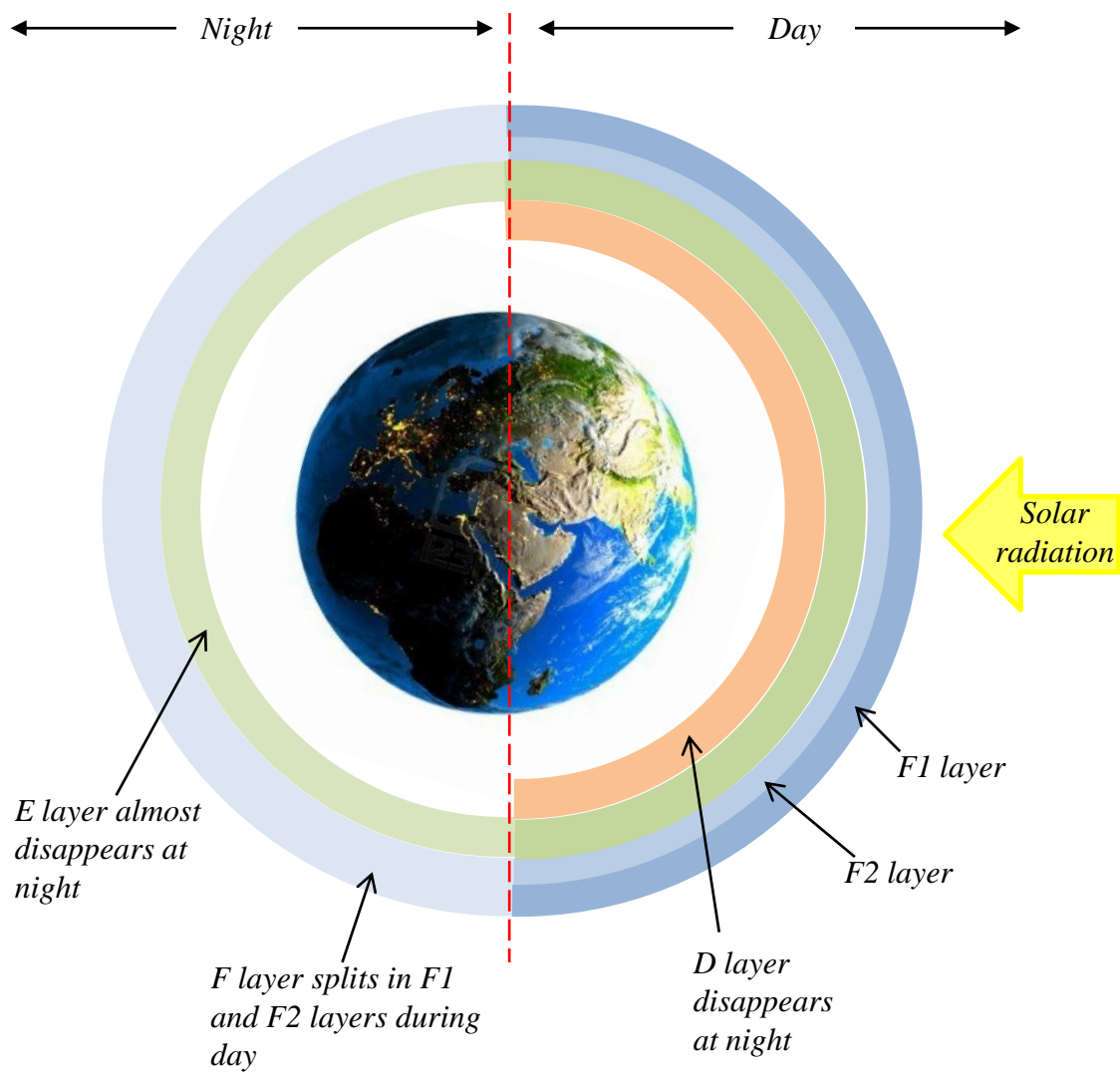


FIGURE 4.2: Day and night representation of ionospheric layers.

The D region is the portion of the ionosphere closest to the Earth's surface and extends from 50 up to 90km. It is mainly responsible for signal attenuation due to large absorption experienced by the waves during propagation through this layer. Moreover, the level of ions concentration in this region is not high enough for wave reflection at HF (3 – 30MHz) so that the D region is often not represented in ionospheric models in which the path losses are included as absorption effects. It is worth pointing out that since the free electron density in this portion of the

ionosphere strictly depends on the solar radiation, the D layer tends to disappear at night with signal absorption becoming lower.

Immediately adjacent to the D layer is the E region, also known as *Kennelly-Heaviside* layer from the names of the American electrical engineer Arthur Edwin Kennelly and the British physicist Oliver Heaviside who first predicted the existence of this layer [56]. It extends from 90 to 130km and has the ability to reflect radio waves at frequencies belonging to the lower part of the HF spectrum allowing for the coverage of ground ranges up to 2000km. For higher frequencies it can only slightly change the direction of travel of the waves as they cross the layer.

From a propagation perspective, the most important ionospheric region is the F layer, also known as *Appleton* layer, from the name of the English physicist Edward Victor Appleton who demonstrated its existence. It extends from 130 up to about 500km above the Earth surface, allowing for propagation up to ranges of tens of thousands of kilometres. Two sublayers, the *F1* and *F2* layers, can often be distinguished and are the result of variations in the chemical concentration between the lower and the upper parts of the *F* layer. Electron density of both F1 and F2 layers is subject to a depletion at night, when the solar radiation is absent, with the F2 layer being the dominant feature at night.

From the above description of the ionosphere structure it is clear that a proper model should be used to evaluate how the level of ionization in each layer affects the propagation of radio waves. This is necessary in order to properly set the radar parameters and ensure the desired radar performance. In this process, special attention needs to be given to the variation that the ionization is subject to. The following section will present a brief review of the models that can be found in literature to describe the ionosphere.

### 4.1.2 Ionospheric models

An ionospheric channel simulator is a necessary tool if we are to estimate the effects of the ionosphere upon the propagating signal for different ionospheric states without expensive measurement campaigns. On the other hand, the simulation of the ionosphere and all the phenomena that lead to ionization variations, requires a very complex model.

As the ionosphere is described by means of ionized layers, models usually represent the ionosphere via a number of concentric layers, each one with different characteristics.

An ionospheric channel simulator will consist of two key components

1. models which focus on the physics of the ionosphere
2. algorithms that calculate the propagation of radio waves through the ionosphere.

The ionospheric model provides an estimation of the physical parameters that describe the ionosphere.

When these parameters are the result of the analysis of measurements collected by sounder systems, rockets or satellites, the model is referred to as *climatological model*. Examples of this kind of model are PRIM, PRISM and FAIM and IRI [57]. It is worth pointing out that the information provided by such models is not real-time since they are derived by an accurate analysis of collected data and only provide an average description of the ionosphere without accounting for irregularities. In order to account for such irregularities, additional models must be used. On the other hand, the ionospheric parameters can be evaluated by exploiting the equations that describe the physics of how the electron density changes as a function of variables related to the solar activity, the geographical location and the Earth's magnetic field. This latter type of ionospheric model is often referred as *physics-based* or *first principle model* and USC GAIM and JPL/USC GAIM are some examples [7].

The second component of the simulator provides a description of the radiowaves propagation through the ionized layers described by the model. This description is usually based on ray-tracing methods, which provide a theoretical description of the electromagnetic field associated to the propagating waves. Ray-tracing methods can be based on *analytical* or *numerical* solutions of the ray-tracing equations. Analytical ray-tracing methods are fast and useful for computationally intensive studies since they provide a closed form solution for the expressions of group range, phase path and other radio wave parameters. On the other hand, they cannot be used when magnetoionic effects are present and the ionosphere varies geographically.

Numerical ray-tracing methods are computationally expensive, but they can evaluate propagation for almost arbitrary ionospheric conditions. Different implementations can be found in literature, and the most widely used are the implementation by Jones' and Stephenson's and the variation proposed by Coleman [58][59]. Examples of ionospheric radiowave propagation programs are VOACAP and ASAPS.

### 4.1.3 Ionospheric variation and disturbances

The morphological structure of the ionosphere described in Sec.4.1.1 accounts for a basic electron density distribution, which is usually associated with an undisturbed ionosphere.

In real situations, though, a number of events may occur and affect the ionization level with consequences for the electron concentration in the ionosphere.

Phenomena responsible for electron density variations in the ionosphere can be periodic, such as diurnal and seasonal variations, or can occur unexpectedly due to unpredictable events that change the structure of the propagation channel.

The first type of phenomena is also referred as *structural* or *slow variability* since they can be considered quasi static during the observation process typical of an OTH radar. The latter, are also called *dynamic* or *fast variability* [7].

Diurnal variations are examples of structural variability. They are mostly due to the day and night cycle of the solar radiation according to the Sun rise and fall. Specifically, as the Sun goes down the ionization process ends because of the lack of solar radiation and, due to the recombination process, the number of free electrons decreases in all the ionospheric layers.

A schematic representation of the of the electron density as a function of the altitude for a fixed range at different hours of the day is if Fig.4.3. As can be seen, the electron density is subject to a remarkable reduction during night hours. In particular, it is possible to notice that the E layer corresponding to the electron density peak around an altitude of about  $120\text{km}$  almost disappears at night.

Similarly, the level of incident radiation is strictly related to the season of the

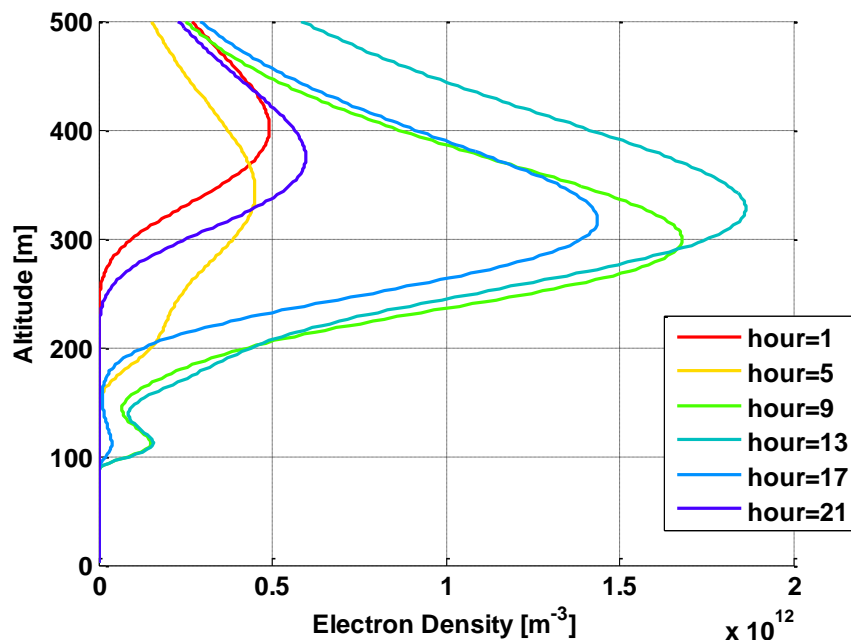


FIGURE 4.3: Electron density profiles vs altitude for different hours of the day.

year so that the electron density of the ionospheric layers is subject to monthly variations as shown in Fig.4.4.

Moreover, solar activity changes with a period of about 11 years, commonly known as *solar cycle*. When the solar activity reaches its minimum, the ionization of the ionosphere goes through a minimum causing a reduction of the frequencies that can be reflected, i.e., supported, by the ionospheric layers and, hence, the ranges that can be covered by the radar. When solar activity reaches its maximum, the

ionization of the ionosphere increases allowing for the support of higher frequencies.

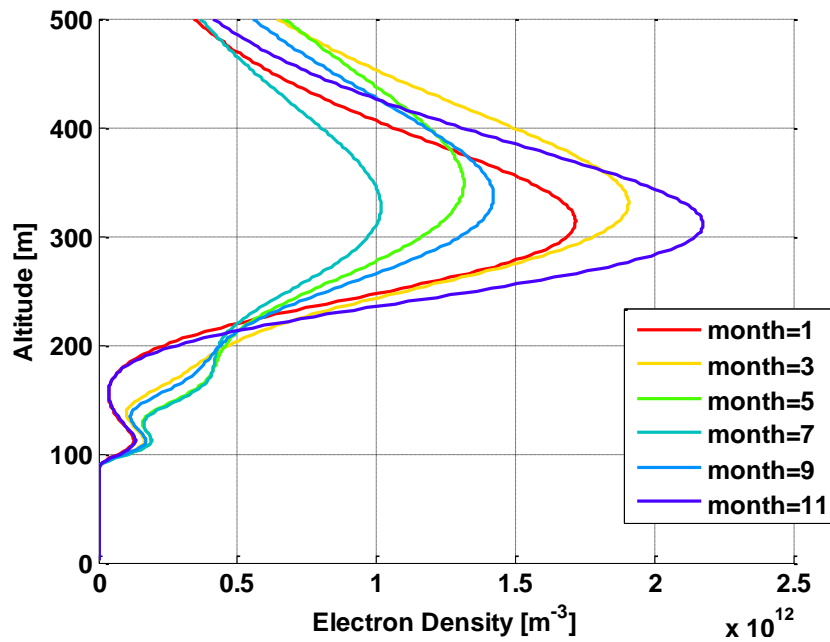


FIGURE 4.4: Monthly variation of the electron density profiles vs altitude at midday.

It is important to underline that the geographical location of the site of interest plays a fundamental role in the amount of variation that the level of ionization is subject to. In particular, geographical variations of the ionospheric structure are mainly related to the latitude. In fact, at higher latitudes, the effects of the solar radiation are reduced by the fact that the angle with the incident solar radiation strikes into the Earth atmosphere is more oblique. This means that the higher the latitude, the smoother the effect of the solar radiation and the lower the ionization level. The peak of the electron density would be expected to correspond to the equatorial regions where the solar radiation is almost perpendicular to the ionospheric layers, but it is instead at latitudes ranging from  $15^\circ$  to  $20^\circ$ . This phenomenon is known as *equatorial anomaly*. A similar anomaly has been observed at the poles, when the minimum of the electron density is not reached at their latitudes, but occurs at latitudes of around  $60^\circ$  with respect to the equator and it is referred as *mid-latitude trough*.

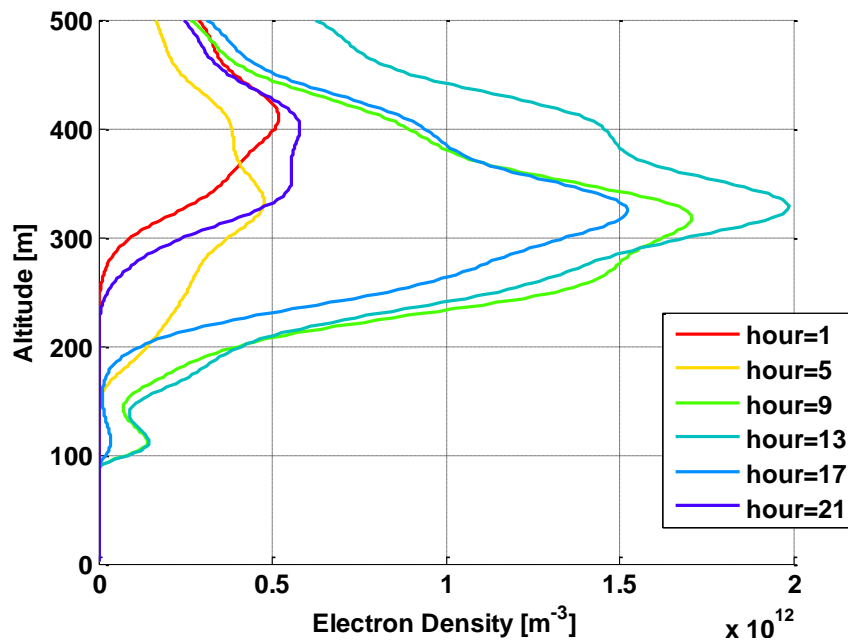


FIGURE 4.5: Electron density profiles vs altitude for different hours of the day in case of ionospheric perturbation (TIDs).

Besides periodic variations, electron density experiences dynamic variations that can cause long range communication and radar disruption due to the high signal corruption or loss. In the literature, a number of processes responsible for these variations in the ionosphere structure have been identified [10] and classified as

1. *Sudden Ionospheric Disturbances* (SIDs) and *Polar Cap Absorption* (PCA)
2. disturbances associated with ionospheric storms
3. *Travelling Ionospheric Disturbances* (TIDs)
4. scintillation.

SIDs are usually associated to bursts of solar radiation that can cause a sudden and rapid increase of charged particle concentration with consequences in terms of signal absorption and radio waves reflection. The bursts of solar radiation are mainly associated with *solar flares*. Solar flares are explosions on the Sun's surface that are usually associated with a large amount release of energy which is responsible for a sudden increase of the photoionization process in the ionized layers, especially in the D region. Such a sudden ionization of the D layer can be so

massive to cause the total absorption of the propagating waves.

Similarly to solar flares, atomic explosions caused by rockets at an height of about  $100\text{km}$  can cause a stream of charged particles that oscillates in the ionosphere due to the forces imprinted by the magnetic field and cause an increase of the absorption in the D layer near the location of the explosion.

Moreover, the effects of such explosions may last up to 10 days, especially at polar latitudes, where they are responsible for the *Polar Cap Absorption*(PAC) phenomenon which is related to an increase of the D layer absorption caused by a stream of protons that can hit the ionosphere several hours after the solar flares happened.

Delayed effects can be also caused by cosmic particles and ionospheric storms that may occur after a solar flare and are responsible also for a depression of critical frequency in the upper layers of the ionosphere, as well as for *sporadic E* and *spread F*.

Depression of the critical frequencies of the higher layers in the ionosphere, specifically in the *F2* layer, means that the range of frequencies that can be transmitted is reduced since higher HF frequencies will pass through the layers without being reflected.

*Sporadic E*, sometimes called *storm E<sub>s</sub>*, because of its correlation to magnetic storms, consists of the presence of anomalous regions within the E layer in which the level of electron concentration is almost equal to the level in the F layer. They are usually few *kms* thick and last for up to  $1h$ , but they can provide a mean for stable HF propagation over Coherent Integration Intervals (CITs) typical of OTH propagation. On the other side, since they are at an altitude of about  $100\text{km}$ , they provide a means for propagation at ranges only up to about  $2000\text{km}$ .

*Spread F* consists of regions within the F layer in which the ionization is highly disturbed and, as a consequence, results in multipath that heavily distorts radiowave propagation. Ionospheric storms are the main causes of Spread F . They

are caused by a stream of charged particles that interact with the earth magnetic field in the auroral regions.

Travelling Ionospheric Disturbances (TIDs) are the manifestations of Atmospheric Gravity Waves (AGWs) that lead to plasma density fluctuations, especially in the F layer [60, 61]. According to their wavelength, TIDs are classified as follows:

1. Large Scale TIDs (LSTIDs), with wavelengths greater than 1000km, periods ranging from few tens of minutes to 3 hours and horizontal phase velocities of 300-1000m/s. They originate in the auroral zone at an height around 100km due to geomagnetic disturbances such as particle precipitations, ionospheric storms, etc.,
2. Medium Scale TIDs (MSTIDs), with wavelengths from 100 to 300km, periods ranging from about 10 minutes to 1 hour and horizontal phase velocities of 100-300m/s. They mostly originate in the lower atmosphere due to meteorological processes such as tropical storms and cyclones
3. Small Scale TIDs (SSTIDs), which originates in the lower atmosphere and have parameters that are smaller than MSTIDs.

The fluctuations in the electron density related to TIDs can be modelled as a modulation of the plasma frequency in unperturbed ionospheric condition [62]. In [62], the plasma frequency in case of TIDs is written as

$$f_p^2 = f_{p0}^2 (1 + \epsilon \sin(kx - \omega_0 t + \vartheta_0)) \quad (4.1)$$

where

- $f_{p0}$  is the plasma frequency related to the quiet ionosphere
- $\epsilon$  is the amplitude of the modulation
- $k$  is the wavenumber

- $\omega_0$  is the angular carrier frequency
- $\vartheta_0$  is the initial phase
- $x$  represents the horizontal direction of the modulation

A representation of the modulation induced by TIDs on plasma frequency can be observed in Fig.4.6, where two different instants of time have been considered. Fig.4.6(a) has been obtained considering the same time instant and the same geographic location of Fig.4.1 so that a comparison can be easily done. Fig.4.6(b) has been obtained for the same geographical location for a different instant of time, so that the time variations of the plasma frequency can be easily observed. the modulation of the ionosphere will also cause modulation of radiowave propagation through this ionosphere and can have a significant impact on OTHR.

Under certain conditions the ionosphere can become highly unstable and this can result in fluctuations (both spatially and temporally) that can extend down to very small scales. When, the electron density distribution is subject to rapid fluctuations in a disturbed patch of ionosphere along the path between the radar and the target, this can cause random variations in the amplitude and phase of the propagating signal [63]. They are usually referred as *scintillation* and their effects on radio-frequency signals propagating through the ionosphere are classified in

1. Intensity scintillations, which result is the signal power being scattered into or out the LoS
2. Angular scintillations, which make the signal appear to come from a direction different with respect to the true direction of the target
3. Phase scintillations, which consist of fluctuations of the phase of the signal due to time and frequency dependent changes in propagation velocity.

The magnitude of scintillations strongly depends on a variety of factors, such as the geographical coordinates of the site of interest, the time of the day, the season, the solar cycle and the wavelength. In particular, scintillations have their

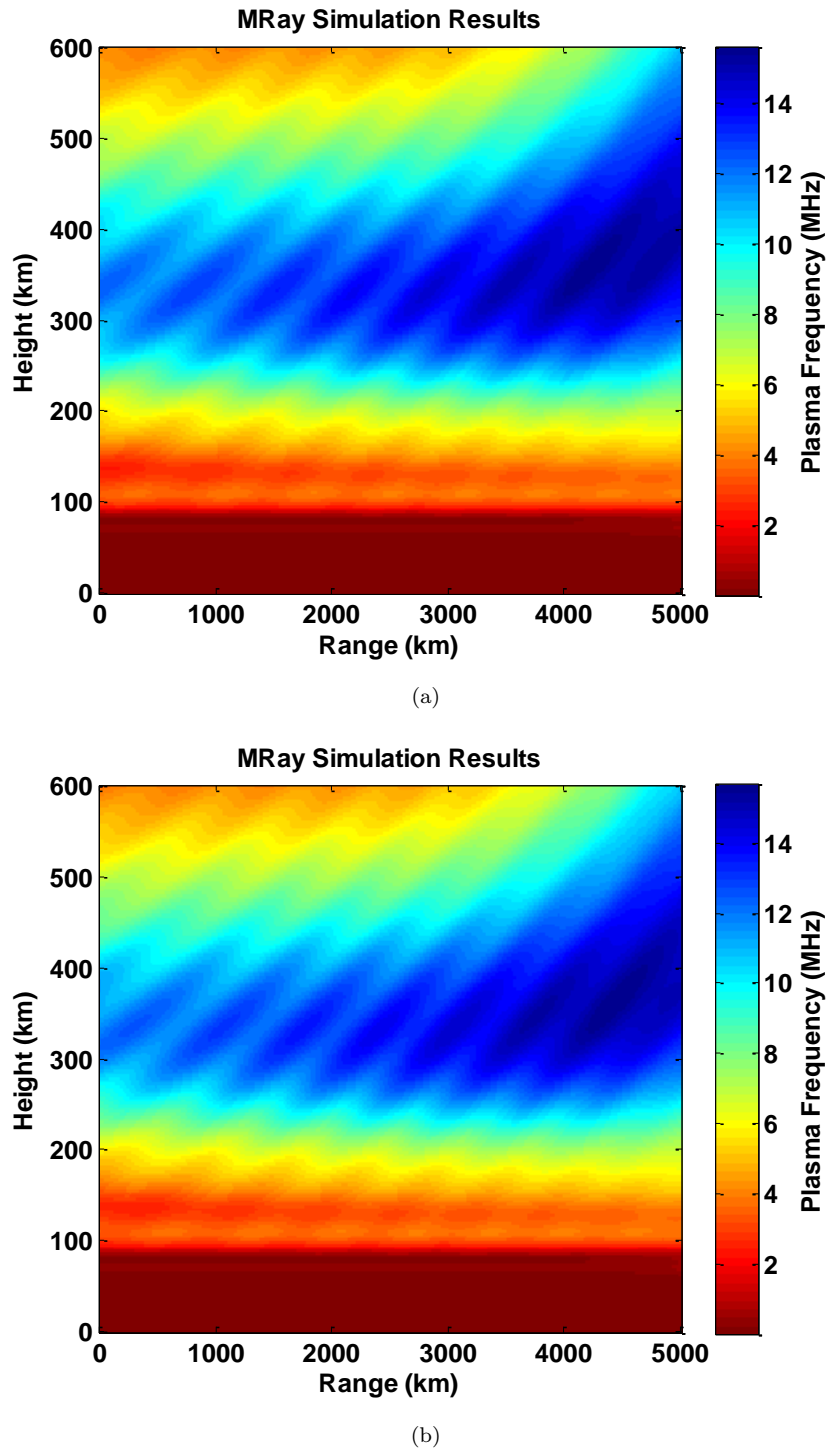


FIGURE 4.6: Representation of plasma frequency variations in altitude and range in presence of TIDs for two different instants of time. Results are based on a Matlab routine created by C.J. Coleman.

maximum in a region within  $10^\circ$  of the magnetic equator and at high latitudes while are lost at mid latitudes. Scintillations is usually worst during night time and at the equinox, showing their maximum when solar activity is high. Ionospheric

scintillation levels are usually higher at longer wavelengths (HF-U/VHF) band and their effect reduces at shorter wavelength becoming almost negligible at X-band.

## 4.2 Ionospheric effects on radiowave propagation

The interaction of radio waves with the free charged particles in the ionosphere is at the basis of radio wave refraction. On the other hand, the very interaction that allows for the reflection to occur is also responsible for signal attenuation and distortion.

An analysis of the effects that a signal undergoes as it travels through the ionosphere, especially considering the disturbances that affect the ionization distribution, is crucial for an HF MIMO radar simulator.

In this section we discuss how the ionosphere, and its fluctuations, impact upon radiowave propagation.

### 4.2.1 Signal Losses

As radio waves cross the ionospheric layers they give up some energy due to the absorption phenomena that occur mainly in the lowest region of the ionosphere. Signal absorption, which defines the *absorption losses*, is one of the most degrading effects that radio waves experience as travelling through the ionized layers of the ionosphere. It occurs mainly in the D layer during the day and its effect is higher at low and mid latitudes. The absorption effect is bigger when solar activity reaches its maximum and rapidly increases when solar flares occur, as described in Sec.4.1.3. In particular, it may happen that the amount of absorption is so high that the level of transmitted signals at the receiver is so low to prevent the detection to be done. This phenomenon is known as *short wave fade out*.

It is worth saying that a signal is subject also to other kind of losses that are not strictly related to the ionosphere structure but they are worth to be mentioned since they contribute to the signal corruption, such as *spreading losses* and *ground*

*reflection losses.*

Spreading losses, or free space losses, are due to the fact that during the propagation the area occupied by the wavefront increases as the distance from the transmitter increases and, as a consequence, the energy for unit area proportionally decreases.

Ground reflection losses occur for multi-hop propagation since they account for the energy that a wave loses each time it bounces on the Earth surface. The amount of ground reflection losses depends on the characteristics of the surface on which the waves bounce.

## 4.2.2 Fading

Fading phenomena are ever present and have been extensively studied in literature especially for conventional OTH Skywave radars [64].

Fading is a general term used to denote signal fluctuations in phase and amplitude caused by irregularities in the ionosphere structure. In particular, three different classes of fading effects can be identified

1. polarization fading, caused by a rotation of the polarization vector,
2. amplitude fading, due to focussing/defocussing effects,
3. multipath fading, related to the presence of more than one propagation path between the transmitter and the receiver.

### 4.2.2.1 Polarization fading: Faraday Rotation effect

Polarization fading consists of a rotation in the polarization vector, which is known as *Faraday rotation* effect. The ionosphere is a birefringent medium, which means that the refractive index depends on the polarization as well as on the angle of incidence of the wave. So, when a linearly polarized wave strikes into ionosphere

it splits into two different modes, the Ordinary (O) and Extraordinary (X) modes, with opposite circular polarizations that travel along slightly different ray paths. Different refractive indexes exist for the O and X rays and so they propagate with different phase velocities through the medium.

The resulting wave that exits the ionosphere is linear, but the polarization vector will be tilted by a quantity which depends on the characteristics of the medium at the time of propagation. As a consequence, polarization mismatch between the receiver antenna system and the incoming wave exists, so that the signal strength is not fully captured in most cases.

It is worth pointing out that the space, time and frequency variability of the ionosphere leads to continuous and unpredictable changes of the phase velocities of the O and X rays and, hence, continuous variations of the polarization vector of the wave arriving at the receiver.

The amount of rotation in radians can be expressed as [65]

$$\Phi = \frac{-e^3}{2m_e^2\epsilon_0c\omega^2} \int_0^d n_e \mathbf{B} \cdot d\mathbf{s} \quad (4.2)$$

where

- .  $e$  is the electron charge [ $C$ ]
- .  $m_e$  is the electron mass [ $kg$ ]
- .  $\epsilon_0$  is the vacuum permittivity [ $\frac{F}{m}$ ]
- .  $c$  is the speed of light [ $\frac{m}{sec}$ ]
- .  $\omega$  is the angular frequency [ $rad$ ]
- .  $\mathbf{B}$  is the Earth's magnetic induction field [ $T$ ]
- .  $d\mathbf{s}$  is the unit vector of length along the wave path [ $m$ ].

The value of Faraday rotation is proportional to the Earth's magnetic field and it is inversely proportional to the square of the frequency and this is the reason why it can be ignored at higher frequencies.

The effect of such polarization mismatch on the received signal can be modelled with an attenuation factor in the amplitude of the signal which is proportional to the amount of rotation, which can be expressed as

$$A_{FR} = |\cos(\Phi)| \quad (4.3)$$

Fluctuations due to TIDs will cause fluctuations in the Faraday rotation and hence fluctuations in amplitude that are part of the above mentioned fading. Moreover, it is worth pointing out that radio waves travelling along different paths may experience very different amplitude attenuations due to Faraday rotation. This is particularly true when considering an HF MIMO radar, in which the signals emitted by the elements of the transmitter can *see* a different ionosphere due to the space variability of the propagation channel and, hence, experience very different degrees of corruption. So, it may happen that the signal received by one of the element of the receiver is so dramatically attenuated that it cannot be detected while other elements of the receiver will be able to detect the replica of the transmitted waveforms. Such event can be associated to the effective loss of some elements of the virtual array, as it will be shown in Ch.6.

#### 4.2.2.2 Amplitude Fading

Amplitude fading refers to fluctuation of the amplitude of waves travelling through the ionosphere that are not associated to polarization mismatch.

It is mainly related to focusing and defocusing effects that occur accordingly to the level of perturbation of the ionosphere. In fact, irregularities in the ionosphere structure can lead to fluctuations in the plasma frequency distribution so that the ionosphere may act as a concave or convex *mirror* resulting in signal focusing or defocusing, with strong variation in the signal amplitude.

### 4.2.2.3 Multipath Fading

Multipath fading refers to the signal strength variation related to the presence of more than one path between the transmitter and the receiver.

In fact, ionospheric propagation is characterized by the presence of more than one path between two end points. At the receiver, all the signals travelling along these different paths are superimposed, each one with its own amplitude and phase. Since the phase strongly depends on the propagation path, it may happen that the signals add coherently or incoherently. This leads to constructive or destructive interference according to the phase differences of the signal contributions and their amplitudes.

It is obvious that irregularities in the ionospheric structure, especially TIDs, have an influence on the phase shifts of propagation modes. In particular, in the case of quiet ionosphere, i.e., without perturbations, the phase shift  $\Delta\varphi$  can be written as a function of the total phase path length,  $P_{total}$ , and the angular frequency,  $\omega_0$ , as [66]

$$\Delta\varphi = -\frac{\omega_0}{c} P_{total} \quad (4.4)$$

where  $c$  is the speed of light in a vacuum and the phase path can be evaluated as the integral along the unperturbed ray path (U.P.) of the refractive index  $\mu$

$$P_{total} = \int_{U.P.} \mu ds \quad (4.5)$$

In case of TIDs, the plasma frequency of the ionosphere is subject to fluctuations that lead to perturbations of the refractive index. In this regard, it can be said that the ionospheric refractive index in presence of irregularities can be seen as the composition of two contributions

$$\mu_p = \mu + \delta\mu \quad (4.6)$$

where  $\mu$  is the refractive index which refers to a quiet ionosphere and  $\delta\mu$  is a refractive index contribution accounting for the variations experienced due to the presence of TIDs.

So, when ionospheric irregularities are present, the total phase path traveled by the wave can be expressed as

$$\begin{aligned} P_{total} &= \int_I^F \mu_p ds \\ &= \int_{U.P.} \mu ds + \int_{P.P.} \delta\mu ds \end{aligned} \tag{4.7}$$

where  $I$  and  $F$  denote the initial and the final point of the ray path through the perturbed ionosphere, respectively.

The integral in the left hand side of Eq.(4.7) can be seen as the superimposition of two contributions, the first related to the phase path that a wave travels in an unperturbed ionosphere plus a term which accounts for the phase path variations due to ionospheric irregularities. In this regard, it should be noted that this latter term should be evaluated on the perturbed path (P.P.) which is subject to ionospheric variations caused by TIDs. This is a very complex task since the evaluation of the path traveled by a wave in a perturbed ionosphere changes continuously according to the intensity of TIDs. However, by exploiting the Fermat principle [62], the phase path variations can be evaluated via integration along the unperturbed path, so that the total phase path can be rewritten as

$$\begin{aligned} P_{total} &= \int_I^F \mu_p ds \\ &= \int_{U.P.} \mu ds + \int_{U.P.} \delta\mu ds \end{aligned} \tag{4.8}$$

From Eq.(4.8) it is clear that the phase shift of a signal propagating through the ionised layers of the ionosphere consists of the superimposition of two terms, one accounting for the phase path that the wave would have travelled in the quiet ionosphere, and another which accounts for the irregularities induced by ionospheric perturbations.

### 4.3 Summary

In the present chapter, the ionosphere has been described from a morphological point of view.

The physics behind the corruption that radio waves experience when passing through the ionosphere has been explained in order to understand the relation between physical events and signal distortion.

In particular, the variations of the basic ionospheric structure have been analysed and classified in slow and fast variability processes. For the first class, diurnal variations, seasonal changes and long period variations, such the ones related to the 11-year solar activity cycle have been described. In regard of the second class, SIDs, TIDs, scintillation and effects due to ionospheric storms and solar flares have been analysed from a ionospheric structure point of view.

The relation between such variations in the ionospheric structure and signal distortions have been shown. In particular, we have discussed the phenomena of fading. Three type of fading have been identified, namely polarization, amplitude and multipath fading. With regard of the polarization fading, a description of the effect known as Faraday rotation has been provided. Focussing and defocussing effects have been described to explain amplitude fading. At the end, a description of the multipath fading has been provided. Special attention has been given to the effect of TIDs on the fading of radio waves. TIDs are ever present and, hence, pose a significant threat to the operation of OTHR.

A proper signal model that is able to account for all these phenomena is essential to an design a HF MIMO simulator and it will be developed in the next chapter.

# Chapter 5

## HF MIMO Radar Signal Model

In the previous chapters the main blocks of the HF MIMO simulator object of the present thesis have been introduced. The transmitter block has been analysed from the signal generation perspective. In this regard, methods for the selection of a set of transmitted waveforms with a desired degree of orthogonality have been presented. The attention has then been focused on the issues concerning the selection of the transmitted waveforms, especially for orthogonal waveforms.

Concerning the receiver, the problem of waveforms separation has been investigated. Two methods have been presented, the first based on matched filtering techniques and the second based on deramping process.

Then a description of the ionospheric channel simulator has been provided with a special attention to the relation between ionospheric disturbances and the level and type of signal corruption.

The next step is to propose a signal model able to account for signal fading and losses in a HF MIMO scenario.

This chapter is so organized as follows. A signal model for an HF MIMO radar is derived starting from the SISO case. Attenuation factors, losses and phase shift factors are accounted by the model in a multipath scenario, considering all the available paths between the transmitter and the receiver. The vector formulation is then proposed to simplify the notation and allow for the evaluation of the HF radar detection performance via Neyman-Pearson detector.

## 5.1 Signal Model

The aim of this section is to propose a signal model which properly describes the evolution of the signals transmitted by the elements of an HF MIMO radar transmitter in their travel through the ionosphere. For this reason, the model will focus on the

- definition of the set of transmitted signals,
- expression of the signal at the target location,
- definition of the signal at the receiver site after ionospheric propagation,
- the expression of the signal after the matched filter at each receiver element.

It is worth pointing out that the signal model will be derived considering the range cell in which the target is, under the assumption of no interference. Under this assumption, the sidelobes due to interference in adjacent range cells are not directly included in the model. On the other hand, it is true that when an interference is present in a cell near the cell of interest, the sidelobes of the ambiguity function cause corruption the useful signal at the input of the matched filter bank in each receiver channel. As a consequence, the design of the transmitted waveforms in a MIMO system must account for the range-angle ambiguity function and suitable waveforms must be selected as a function of the level of sidelobes. In addition, such an assumption does not consider the fact that signal corruption from interferences in near cells is usually much more severe than ionospheric degradation. For this reason, this topic deserves further studies in order to create an appropriate model of the interference and include it in the proposed simulator.

Let consider a system with  $N_{tx}$  transmitter elements and  $N_{rx}$  receiver elements and a far field target with location denoted by  $\mathbf{p}_T = (p_T, q_T, r_T)$  in a Cartesian local reference system embedded on the phase centre of the transmitter system.

In order to clearly explain the way the model is derived, the signal model for the simple SISO (*Single Input Single Output*) case, i.e.  $N_{tx} = N_{rx} = 1$ , is considered first while the model form the MIMO case will be derived later.

Suppose to consider an HF SISO radar which transmits a single waveform which will propagate through the ionosphere, interact with the far field target and then propagate towards the receiver.

Moreover, since ionospheric propagation is characterised by multipath, the transmitted signal may propagate from the transmitter to the receiver via a number of paths which depends on the modes supported by the ionosphere at the time of transmission. It is then obvious that the signal model must account for all the paths travelled by the transmitted waveform and evaluate the corresponding attenuation and phase distortion. At the receiver, the total signal is evaluated as the superimposition of all the received contributions due to multiple propagation<sup>1</sup>.

For the sake of simplicity, the problem concerning the propagation from the

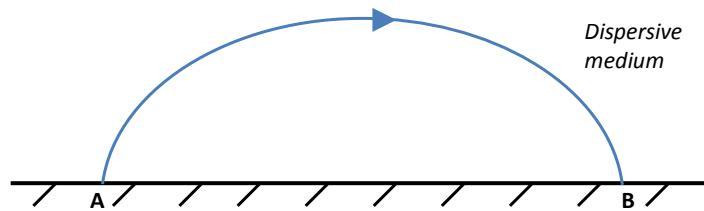


FIGURE 5.1: Schematic representation of the propagation between two end points through a dispersive medium.

transmitter to the receiver via target, can be split into two sub-problems, i.e., the propagation from the transmitter to the target, and then the propagation from the target to the receiver. Suppose  $M(f)$  is the baseband signal emitted by the transmitter element in the frequency domain, so that the signal in the time domain can be expressed as follows

$$m(t) = \int_{-B}^B M(f) e^{j2\pi ft} df \quad (5.1)$$

<sup>1</sup>Under the hypothesis of neglecting the mutual coupling among the element of the transmitter and the elements of the receiver.

where  $B$  is the signal bandwidth, so that  $x(t) = \Re\{m(t)e^{j2\pi f_0 t}\}$

Let  $y_T(t)$  be the signal at the target location,  $\mathbf{P}_T$ , which is given by the superimposition of all the contributions corresponding to the different paths travelled by the transmitted signal, i.e.

$$\begin{aligned} y_T(t) &= \sum_{r=1}^R y_T^{(r)}(t) \\ &= \sum_{r=1}^R \frac{A_T^{(r)}}{L_T^{(r)}} \int_{-B}^{+B} M(f) e^{j2\pi(f+f_0)(t-\tau_T^{(r)}(\mathbf{P}_T, f+f_0))} df \end{aligned} \quad (5.2)$$

where

- $R$  is the number of ray paths between the transmitter and the target
- $A^{(r)}$  is the attenuation due to Faraday rotation along the  $r^{th}$  path
- $L^{(r)}$  comprises all the losses along the  $r^{th}$  path
- $f_0$  is the carrier frequency
- $\tau_T^{(r)}(\mathbf{P}_T, f + f_0)$  is the phase delay between the transmitter and the target along the  $r^{th}$  ray at the frequency  $f + f_0$  with  $f \in [f_0 - \frac{B}{2}] \cup [f_0 + \frac{B}{2}]$ .

It is worth pointing out that, as the transmitted wave travels along each of the  $R$  paths, it experiences an amount of fading and losses that are specific to the ray path. This explains the dependence of the attenuation due to Faraday rotation,  $A^{(r)}$ , the signal losses,  $L^{(r)}$ , and the phase delay,  $\tau_T^{(r)}(\mathbf{P}_T, f + f_0)$ , from the index  $r$  which denotes the specific ray path.

Suppose that the transmitted waveforms are narrowband, i.e.,  $B \ll f_0$ . In this case, the delay factor  $\tau_T^{(r)}(\mathbf{P}_T, f + f_0)$  can be approximated using its Taylor expansion up to the first order term<sup>2</sup>

<sup>2</sup>Higher order terms can be used to model signal distortions that are typical for signal propagating near the skip zone.

$$\bar{\tau}_T^{(r)}(\mathbf{p}_T, f + f_0) \cong \bar{\tau}_T^{(r)}(f_0) + f \frac{d\bar{\tau}_T^{(r)}}{df} + \dots \quad (5.3)$$

Considering Eq.(5.3) and after a few mathematical manipulations, the signal at the target location can be rewritten as

$$\begin{aligned} y_T(t) &= \sum_{r=1}^R \frac{A^{(r)}}{L^{(r)}} \int_{-B}^{+B} M(f) e^{j2\pi f_0(t-\tau_{P,T}^{(r)}(f_0))} e^{j2\pi f(t-\tau_{G,T}^{(r)})} df \\ &= \sum_{r=1}^R \frac{A^{(r)}}{L^{(r)}} e^{j2\pi f_0(t-\tau_{P,T}^{(r)}(f_0))} m\left(t - \tau_{G,T}^{(r)}\right) \end{aligned} \quad (5.4)$$

where Eq.(5.5) and Eq.(5.6) are the phase delay and the group delay, respectively

$$\tau_{P,T}^{(r)}(f_0) = \bar{\tau}_T^{(r)}(f_0) \quad (5.5)$$

$$\tau_{G,T}^{(r)} = \bar{\tau}_T^{(r)}(f_0) + f_0 \frac{d\bar{\tau}_T^{(r)}}{df} \quad (5.6)$$

At this point the signal scattered by the target is proportional to the incident one according to a proportionality factor given by the target reflectivity, which is a function that depends on the target features as well as the direction of arrival and departure of the signal. It is important to underline that during its travel towards the receiver, the signal is subject to multipath, so it can reach the receiver via multiple paths. Assume that  $Q$  is the number of paths from the target to the receiver and let  $q = 1, 2, \dots, Q$  be the index which denotes these paths. So, the signal backscattered from the target at the receiver location can be written as

$$\begin{aligned}
z_{\text{siso}}(t) &= \sum_{q=1}^Q \frac{A^{(q)}}{L^{(q)}} \sigma^{(r,q)} e^{-j2\pi f_0(\tau_P^{(q)})} y_T(t - \tau_G^{(q)}) \\
&= \sum_{q=1}^Q \sum_{r=1}^R \frac{A^{(r,q)}}{L^{(r,q)}} \sigma^{(r,q)} e^{j2\pi f_0(t - \tau_P^{(r,q)})} m(t - \tau_G^{(r,q)})
\end{aligned} \tag{5.7}$$

where

- $A^{(r,q)} = A^{(r)}A^{(q)}$  is the total attenuation due to Faraday rotation undergone by the signal propagating along the path given by the  $r^{\text{th}}$  path between the transmitter and the target and the  $q^{\text{th}}$  path between the target and the receiver
- $L^{(r,q)} = L^{(r)}L^{(q)}$  is the total loss undergone by the signal propagating along the path given by the  $r^{\text{th}}$  path between the transmitter and the target and the  $q^{\text{th}}$  path between the target and the receiver
- $\sigma^{(r,q)}$  is the target reflectivity, for the signal propagating along the path given by the  $r^{\text{th}}$  path between the transmitter and the target and the  $q^{\text{th}}$  path between the target and the receiver
- $\tau_P^{(r,q)} = \tau_P^{(r)} + \tau_P^{(q)}$  is the total phase delay undergone by the signal propagating along the path given by the  $r^{\text{th}}$  path between the transmitter and the target and the  $q^{\text{th}}$  path between the target and the receiver
- $\tau_G^{(r,q)} = \tau_G^{(r)} + \tau_G^{(q)}$  is the total group delay undergone by the signal propagating along the path given by the  $r^{\text{th}}$  path between the transmitter and the target and the  $q^{\text{th}}$  path between the target and the receiver.

Suppose now to have more than one transmitter, i.e. an HF MISO (*Multiple Input Single Output*) system with  $N_{tx}$  transmitter elements. The signal at the single receiver can be easily derived by the SISO case. In fact, assuming to neglect the coupling effects among the transmitter elements, the signal at the receiver location is given by the superimposition of all the replica of the transmitted waveforms.

So, assume  $m = 1, 2, \dots, N_{tx}$  denotes the transmitter elements and that  $M_m(f)$  is the baseband signal emitted by the  $m^{th}$  transmitter element in the frequency domain and that the transmitted waveforms are orthogonal

$$\int m_i(t)m_j(t)dt = \delta_{ij} \quad (5.8)$$

where  $\delta_{ij}$  is the Kronecker delta defined in Eq.(3.2).

As stated above, the signal at the receiver is given by the superimposition of the signals coming from all the elements of the transmitter, each one with its own phase shift and amplitude attenuation, according to the whole path travelled. In order to account for the fact that attenuation and phase shift depend on the transmitter location, let denote  $z_{siso,m}$  the signal contribution at the receiver corresponding to the signal emitted by the  $m^{th}$  transmitter element

$$z_{siso,m}(t) = \sum_{q=1}^Q \sum_{r=1}^{R_m} \frac{A_m^{(r,q)}}{L_m^{(r,q)}} \sigma_m^{(r,q)} e^{j2\pi f_0(t - \tau_{P,m}^{(r,q)})} m(t - \tau_{G,m}^{(r,q)}) \quad (5.9)$$

where

- $R_m$  defines the number of paths available between the  $m^{th}$  transmitter and the target
- $A_m^{(r,q)}$  and  $L_m^{(r,q)}$  are the attenuation and the loss factors related to the signal emitted by the  $m^{th}$  transmitter that travels along the path defined by  $r$  and  $q$
- $\tau_{P,m}^{(r,q)}$  and  $\tau_{G,m}^{(r,q)}$  are the phase and the group delays corresponding to the signal emitted by the  $m^{th}$  transmitter travelling along the path defined by  $r$  and  $q$
- $\sigma_m^{(r,q)}$  is target's RCS for the signal emitted by the  $m^{th}$  transmitter and propagating along the path identified by  $(p, q)$  in the SISO case

Considering Eq.(5.9), the contribution of all the  $N_{tx}$  transmitter elements, the total signal at the receiver is given by

$$z_{miso}(t) = \sum_{m=1}^{N_{tx}} z_{siso,m}(t) \quad (5.10)$$

At this stage, the evaluation of the expression of the signal for an HF MIMO radar system is straightforward. In fact, the difference with a MISO system is that in a MIMO radar a number  $N_{rx}$  of receivers are available. Two considerations can be drawn from this fact:

1. for each receiver element, the signal assumes the form of the expression in Eq.(5.10). The only difference is that in this case the number of available rays between the target and the receiver depends on the receiver location, i.e., from  $Q = Q_n$
2. by neglecting the mutual coupling between the receiver elements, the global signal at the receiver is given by the superimposition of all the signal received at each single element of the receiver, as in Eq.(5.11).

After the above considerations, the signal at the  $n^{th}$  receiver element can be written as

$$z_n(t) = e^{j2\pi f_0 t} \sum_{m=1}^{N_{tx}} \sum_{r=1}^{R_m} \sum_{q=1}^{Q_n} \frac{A_{mn}^{(r,q)}}{L_{mn}^{(r,q)}} \sigma_{mn}^{(r,q)} e^{-j2\pi f_0 \tau_{P,mn}^{(r,q)}} m_m \left( t - \tau_{G,mn}^{(r,q)} \right) \quad (5.11)$$

It is worth pointing out that all the factors defining the attenuation, the loss factor, the phase delay and the group delay depend on both the transmitter and the receiver location. Moreover, since multipath is present, each of the above mentioned factors strictly depends on the specific path travelled by the e.m. wave and which is identified by the pair  $(r, q)$ .

At this point, in order to fully exploit the advantages of the transmission of multiple orthogonal waveforms, the contributions related to the transmitted waveforms must be separated. In order to simplify the notation, the signal after the separation process will be written in a vector notation in the next section.

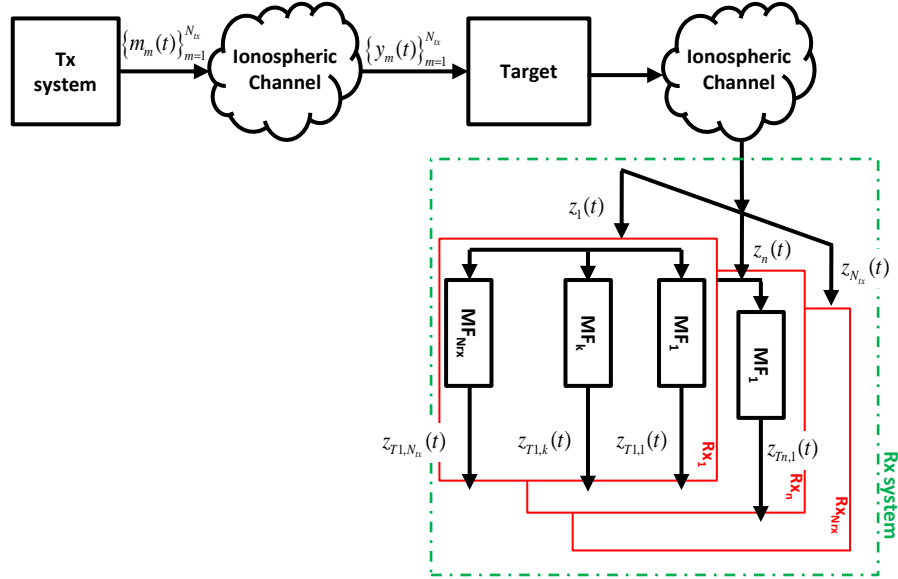


FIGURE 5.2: Block diagram of the path travelled by the transmitted signals in a HF MIMO radar.  $y_m(t)$  denotes the contribution from the  $m^{th}$  transmitter to the target.

### 5.1.1 Vector Notation

In order to understand the detection capabilities of a HF MIMO radar it is useful to write the signal model in a vector notation.

As explained in Sec.3.2, at each receiver element, a bank of matched filters is used to separate the contributions relative to each transmitted waveforms. Under the assumption that the transmitted signals are mutually orthogonal<sup>3</sup>, the output of the  $k^{th}$  matched filter at the  $n^{th}$  receiver is given by

$$\begin{aligned}
 z_{Tn,k}(t) &= \int_{-\infty}^{+\infty} z_{miso}(\tau) m_k^*(\tau - t) dt \\
 &= \sum_{m=1}^{N_{tx}} \sum_{r=1}^{R_m} \sum_{q=1}^{Q_n} \frac{A_{mn}^{(r,q)}}{L_{mn}^{(r,q)}} \sigma_{mn}^{(r,q)} e^{-j2\pi f_0 \tau_{P,mn}^{(r,q)}} \int_{-\infty}^{+\infty} m_m(\tau - \tau_{G,mn}^{(r,q)}) m_k^*(\tau - t) dt
 \end{aligned} \tag{5.12}$$

<sup>3</sup>This hypothesis does not account for interferences among time-shifted waveforms, as explained at the beginning of this very chapter.

where  $*$  denotes the complex conjugate.

Under the assumption that the matched filter perfectly matches the transmitted signal, then the integral in Eq.(5.12) is non-zero only if  $m = k$ . So, the output of the  $k^{th}$  matched filter at the  $n^{th}$  receiver element for the range cell in which the target is present, is given by

$$u_{kn} = \mathbf{h}_{kn}^T \boldsymbol{\sigma}_{kn} + w_{kn} \quad (5.13)$$

where

- $\mathbf{h}_{kn}$  is a  $\left(Q_n \sum_{k=1}^{N_{tx}} R_k\right) \times 1$  vector containing the all the factors that can be associated with the propagation through the ionospheric channel. In particular, it accounts for multipath propagation, attenuation due to Faraday rotation, signal losses and phase delay.  $T$  denotes the transpose operator.
- $\boldsymbol{\sigma}_{kn}$  is a  $\left(Q_n \sum_{k=1}^{N_{tx}} R_k\right) \times 1$  vector containing the target reflectivity seen by every signal bouncing on the target
- $w_{kn}$  is the noise at the output of the  $k^{th}$  matched filter. This terms account for all the noise and interference contribution relative to an HF MIMO radar.

The generic element of  $\mathbf{h}_{kn}$  and  $\boldsymbol{\sigma}_{kn}$  can be written as follows

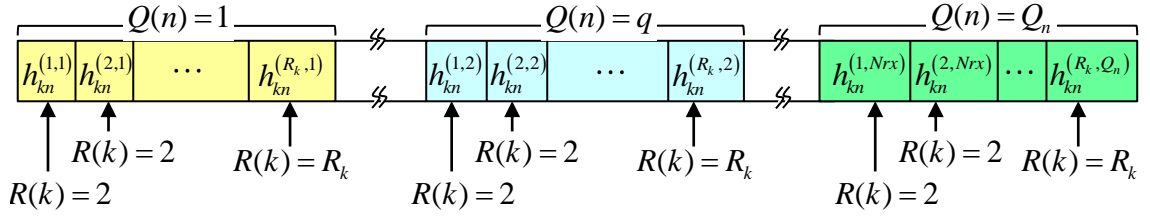
$$\begin{aligned} \left[ h_{kn}^{(r,q)} \right]_{\substack{r = 1, \dots, R_k \\ q = 1, \dots, Q_n}} &= \frac{A_{kn}^{(r,q)}}{L_{kn}^{(r,q)}} e^{j2\pi f_0 \tau_{P,kn}^{(r,q)}} \end{aligned} \quad (5.14)$$

$$\begin{aligned} \left[ \sigma_{kn}^{(r,q)} \right]_{\substack{r = 1, \dots, R_k \\ q = 1, \dots, Q_n}} &= \sigma_{kn}^{(r,q)} \end{aligned} \quad (5.15)$$

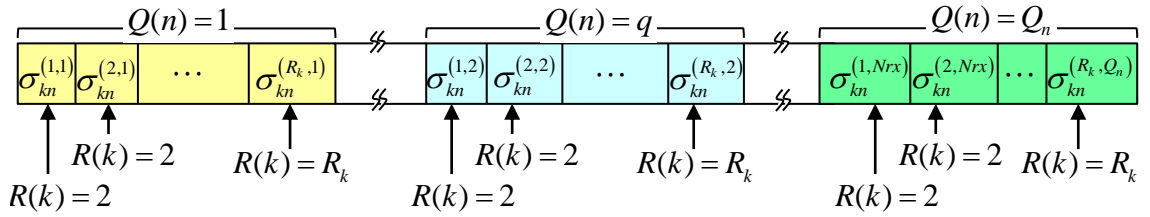
that is

$$\mathbf{h}_{kn} = \left[ h_{kn}^{(1,1)} \quad h_{kn}^{(2,1)} \quad \dots \quad h_{kn}^{(R_k,1)} \quad h_{kn}^{(1,2)} \quad \dots \quad h_{kn}^{(R_k,Q_n)} \right]^T \quad (5.16)$$

$$\boldsymbol{\sigma}_{kn} = \left[ \sigma_{kn}^{(1,1)} \quad \sigma_{kn}^{(2,1)} \quad \dots \quad \sigma_{kn}^{(R_k,1)} \quad \sigma_{kn}^{(1,2)} \quad \dots \quad \sigma_{kn}^{(R_k,Q_n)} \right]^T \quad (5.17)$$



(a)



(b)

FIGURE 5.3: Schematic representation of the structure of  $\mathbf{h}_{kn}$  and  $\boldsymbol{\sigma}_{kn}$  as they appear in Eq.(5.16) and Eq.(5.17) respectively. Both the schematic representation refer to the output of the generic  $k^{th}$  matched filter in the  $n^{th}$  receiver chain.

The outputs of all the  $N_{tx}$  matched filters at the generic  $n^{th}$  element of the receiver can be stacked in a vector as follows

$$\mathbf{u}_n = \begin{bmatrix} u_{1n} \\ u_{2n} \\ \vdots \\ u_{N_{tx}n} \end{bmatrix} \in \mathbb{C}^{N_{tx} \times 1} \quad (5.18)$$

which can be rewritten as

$$\mathbf{u}_n = \mathbf{H}_n \boldsymbol{\sigma}_n + \mathbf{w}_n \quad (5.19)$$

where

- $\mathbf{H}_n$  is a matrix which contains all the factors affecting the signal during propagation from the transmitter system towards the generic  $n^{\text{th}}$  element of the receiver
- $\boldsymbol{\sigma}_n$  is a stacked version of all the  $\boldsymbol{\sigma}_{kn}$  vectors defined in Eq.(5.17)
- $\mathbf{w}_n$  is an  $N_{tx} \times 1$  vector containing the noise contributions at the output of each matched filter at the  $n^{\text{th}}$  receiver.

The structure of all the vectors and matrix in Eq.(5.18) are as follows

$$\begin{aligned} \mathbf{H}_n &= \text{blockdiag} \left\{ \mathbf{h}_{1n}^T, \mathbf{h}_{2n}^T, \dots, \mathbf{h}_{N_{tx}n}^T \right\} \\ &= \begin{bmatrix} \mathbf{h}_{1n}^T & 0 & \cdots & \cdots & 0 \\ 0 & \mathbf{h}_{2n}^T & 0 & \cdots & \vdots \\ \vdots & 0 & \ddots & 0 & \vdots \\ \vdots & & 0 & \ddots & 0 \\ 0 & \cdots & \cdots & 0 & \mathbf{h}_{N_{tx}n}^T \end{bmatrix} \in \mathbb{C}^{N_{tx} \times Q_n \sum_{k=1}^{N_{tx}} R_k} \end{aligned} \quad (5.20)$$

$$\boldsymbol{\sigma}_n = \left[ \boldsymbol{\sigma}_{1n}^T, \boldsymbol{\sigma}_{2n}^T, \dots, \boldsymbol{\sigma}_{N_{tx}n}^T \right]^T \in \mathbb{C}^{Q_n \sum_{k=1}^{N_{tx}} R_k \times 1} \quad (5.21)$$

$$\mathbf{w}_n = \left[ w_{1n}, w_{2n}, \dots, w_{N_{tx}n} \right]^T \in \mathbb{C}^{N_{tx} \times 1} \quad (5.22)$$

Since a bank of  $N_{tx}$  matched filters is used at each of the  $N_{rx}$  receiver element, the global signal at the receiver site is given by  $N_{tx}N_{rx}$  contributions and can be written as

$$\mathbf{u} = \mathbf{H}\boldsymbol{\sigma} + \mathbf{w} \quad (5.23)$$

where

$$\begin{aligned} \mathbf{H} &= \text{blockdiag} \left\{ \mathbf{H}_1, \mathbf{H}_2, \dots, \mathbf{H}_{N_{rx}} \right\} \\ &= \begin{bmatrix} \mathbf{H}_1 & 0 & \cdots & \cdots & 0 \\ 0 & \mathbf{H}_2 & 0 & \cdots & \vdots \\ \vdots & 0 & \ddots & 0 & \vdots \\ \vdots & & 0 & \ddots & 0 \\ 0 & \cdots & \cdots & 0 & \mathbf{H}_{N_{rx}} \end{bmatrix} \in \mathbb{C}^{N_{tx}N_{rx} \times \sum_{n=1}^{N_{rx}} \sum_{k=1}^{N_{tx}} Q_n R_k} \end{aligned} \quad (5.24)$$

$$\boldsymbol{\sigma} = \left[ \boldsymbol{\sigma}_1^T, \boldsymbol{\sigma}_2^T, \dots, \boldsymbol{\sigma}_{N_{rx}}^T \right]^T \in \mathbb{C}^{\sum_{n=1}^{N_{rx}} \sum_{k=1}^{N_{tx}} Q_n R_k \times 1} \quad (5.25)$$

$$\mathbf{w} = \left[ \mathbf{w}_1^T, \mathbf{w}_2^T, \dots, \mathbf{w}_{N_{rx}}^T \right]^T \in \mathbb{C}^{N_{tx}N_{rx} \times 1} \quad (5.26)$$

It is worth pointing out that the matrix  $\mathbf{H}$  in Eq.(5.24) provides a description of the propagation channel between the transmitter and the receiver at the time of transmission. So, it is clear that this matrix changes accordingly to the ionosphere state variation. The vector  $\boldsymbol{\sigma}$  provides a description of the target as it is seen by the transmitter and the receiver.

## 5.2 Target Detection

Once the expression of the signal at the receiver is available, the problem of target detection in an HF MIMO radar can be formulated considering two hypotheses,  $H_0$  for which there is no target in the range cell considered,  $H_1$  for which the target is present.

So, the problem can be rewritten as [67]

$$\begin{aligned} H_0 : \mathbf{u} &= \mathbf{w} \\ H_1 : \mathbf{u} &= \mathbf{H}\boldsymbol{\sigma} + \mathbf{w} \end{aligned} \quad (5.27)$$

In this case, the optimum detector in the Neyman-Pearson sense is given by the Likelihood Ratio Test (LRT) that is

$$\frac{f_{\mathbf{u}|H_1}(\mathbf{u}|H_1)}{f_{\mathbf{u}|H_0}(\mathbf{u}|H_0)} \underset{H_0}{\overset{H_1}{\gtrless}} \chi \quad (5.28)$$

where  $f_{\mathbf{u}|H_1}(\mathbf{u}|H_1)$  and  $f_{\mathbf{u}|H_0}(\mathbf{u}|H_0)$  are the probability density functions of the measured signal under the hypothesis  $H_1$  and  $H_0$  respectively and  $\chi$  is a threshold.

Suppose to model the noise at the output of the matched filters and the radar cross section as Gaussian vectors with zero mean and covariance matrix  $\mathbf{R}_w$  and  $\mathbf{R}_\sigma$  respectively, so that

$$f_{\mathbf{w}}(\mathbf{w}) = \frac{1}{[2\pi \det(\mathbf{R}_w)]^{\frac{1}{2}}} \exp \left\{ -\frac{1}{2} (\mathbf{w}^H \mathbf{R}_w^{-1} \mathbf{w}) \right\} \quad (5.29)$$

and

$$f_{\boldsymbol{\sigma}}(\boldsymbol{\sigma}) = \frac{1}{[2\pi \det(\mathbf{R}_\sigma)]^{\frac{1}{2}}} \exp \left\{ -\frac{1}{2} (\boldsymbol{\sigma}^H \mathbf{R}_\sigma^{-1} \boldsymbol{\sigma}) \right\} \quad (5.30)$$

where  $H$  denotes the Hermitian operator.

Under these assumptions, the probability density functions in Eq.(5.28) can be written as

$$f_{\mathbf{u}|H_0}(\mathbf{u}|H_0) = \gamma_0 \exp \left\{ -\frac{1}{2} (\mathbf{u}^H \mathbf{R}_w^{-1} \mathbf{u}) \right\} \quad (5.31)$$

where

$$\gamma_0 = \frac{1}{[2\pi \det(\mathbf{R}_w)]^{\frac{1}{2}}} \quad (5.32)$$

and

$$f_{\mathbf{u}|H_1}(\mathbf{u}|H_1) = \int_{-\infty}^{+\infty} f_{\mathbf{u}|H_1}(\mathbf{u}|H_1, \boldsymbol{\sigma}) f_{\boldsymbol{\sigma}}(\boldsymbol{\sigma}) d\boldsymbol{\sigma} \quad (5.33)$$

The solution to Eq.(5.33) can be found considering that

$$f_{\mathbf{u}|H_1}(\mathbf{u}|H_1, \boldsymbol{\sigma}) = \gamma_1 \exp \left\{ -\frac{1}{2} (\mathbf{u} - \mathbf{H}\boldsymbol{\sigma})^H \mathbf{R}_w^{-1} (\mathbf{u} - \mathbf{H}\boldsymbol{\sigma}) \right\} \quad (5.34)$$

where

$$\gamma_1 = \frac{1}{[2\pi \det(\mathbf{R}_\sigma)]^{\frac{1}{2}}} \quad (5.35)$$

Now, by substituting Eq.(5.34) and Eq.(5.30) in (5.33) it can be easily found that

$$\begin{aligned} f_{\mathbf{u}|H_1}(\mathbf{u}|H_1) &= \gamma_0 \gamma_1 \int_{-\infty}^{+\infty} \exp \left\{ -\frac{1}{2} \left[ (\mathbf{u} - \mathbf{H}\boldsymbol{\sigma})^H \mathbf{R}_w^{-1} (\mathbf{u} - \mathbf{H}\boldsymbol{\sigma}) + \boldsymbol{\sigma}^H \mathbf{R}_\sigma \boldsymbol{\sigma} \right] \right\} d\boldsymbol{\sigma} \\ &= \gamma_0 \gamma_1 \exp \left\{ -\frac{1}{2} \mathbf{u}^H \mathbf{R}_w^{-1} \mathbf{u} \right\} \times \\ &\quad \times \int_{-\infty}^{+\infty} \exp \left\{ -\frac{1}{2} (\mathbf{u}^H \mathbf{R}_w^{-1} \mathbf{H}\boldsymbol{\sigma} - \boldsymbol{\sigma}^H \mathbf{H}^H \mathbf{R}_w^{-1} \mathbf{u} + \boldsymbol{\sigma}^H \mathbf{M}\boldsymbol{\sigma}) \right\} d\boldsymbol{\sigma} \end{aligned} \quad (5.36)$$

where

$$\mathbf{M} = \mathbf{H}^H \mathbf{R}_w^{-1} \mathbf{H} + \mathbf{R}_\sigma^{-1} \quad (5.37)$$

After a few mathematical manipulations, Eq.(5.36) can be rewritten as

$$\begin{aligned} f_{\mathbf{u}|H_1}(\mathbf{u}|H_1) &= \gamma_0 \gamma_1 \exp \left\{ -\frac{1}{2} \mathbf{u}^H \mathbf{R}_w^{-1} \mathbf{u} \right\} \exp \left\{ \mathbf{u}^H \mathbf{R}_w^{-1} \mathbf{H} \mathbf{M}^{-1} \mathbf{H}^H \mathbf{R}_w^{-1} \mathbf{u} \right\} \times \\ &\times \int_{-\infty}^{+\infty} \exp \left\{ -\frac{1}{2} (\boldsymbol{\sigma} - \boldsymbol{\eta}_\sigma)^H \mathbf{M} (\boldsymbol{\sigma} - \boldsymbol{\eta}_\sigma) \right\} d\boldsymbol{\sigma} \\ &= \gamma_0 \gamma_1 \exp \left\{ -\frac{1}{2} \mathbf{u}^H \mathbf{R}_w^{-1} \mathbf{u} \right\} \exp \left\{ \boldsymbol{\mu}_u^H \mathbf{M}^{-1} \boldsymbol{\mu}_u \right\} \end{aligned} \quad (5.38)$$

where

$$\begin{aligned} \boldsymbol{\eta}_\sigma &= \mathbf{M}^{-1} \boldsymbol{\mu}_u \\ \boldsymbol{\mu}_u &= \mathbf{H}^H \mathbf{R}_w^{-1} \mathbf{u} \end{aligned} \quad (5.39)$$

So, the LRT of (5.28) becomes

$$\left( \boldsymbol{\mu}_u^H \mathbf{M}^{-1} \boldsymbol{\mu}_u \right) \underset{H_0}{\overset{H_1}{\gtrless}} \chi_1 \quad (5.40)$$

where

$$\chi_1 = \chi - \log \{ \gamma_2 \} \quad (5.41)$$

is the modified threshold.

### 5.3 Summary

In the present chapter a signal model for the HF MIMO radar which is object of the present thesis has been provided.

Firstly, the simple SISO case has been treated in order to find a proper formulation

for the effects experienced by the signal in a multipath ionospheric environment. The SISO model has been exploited then to find the expression of the signal in the MISO and MIMO cases. It is worth saying that the problem of range-angle ambiguity function sidelobes has been neglected since the signal model focuses on the range cell where the target is, under the assumption of no interference from adjacent cells. This is a simplifying assumption that has been done to focus the attention on the propagation effects on the transmitted signals. On the other hand, such an assumption does not consider the fact that signal corruption from interferences in near cells is usually much more severe than ionospheric degradation. For this reason, this topic deserves further studies in order to create an appropriate model of the interference and include it in the proposed simulator.

A vector formulation has been provided and the expression of the signal detector under the Neymann-Pearson sense evaluated. In this regard, two simple Gaussian distribution have been used to model the radar cross section and the noise at the output of the matched filters.

# Chapter 6

## HF MIMO Radar Simulator

The HF MIMO radar simulator proposed in Ch.3 consists of three macro-blocks, namely the transmitter, the ionospheric channel simulator and the receiver. All the three blocks have been described from a functional perspective, in order to understand the issues that can be encountered in the the signal generation, propagation and separation processes.

This chapter aims to bring together these various blocks into a simulator that can evaluate the signal received by an element of the receiver. In particular, a flow chart will be given in order to clarify the steps that allow the evaluation of the effects that signal experiences as it travels from the transmitter to the receiver via the ionosphere.

A number of software routines have been implemented in MatLab<sup>®</sup> <sup>1</sup> according to the steps showed in the flowchart. However, a number of issues have been encountered during the development of this software and this will be described in the present chapter. The flowchart will be described first, and then the various elements of the flowchart will be explained from an implementation perspective. Special attention will be given to the evaluation of the skip distance as this sets the limits of propagation. At the end, some sample results will be shown.

---

<sup>1</sup>MatLab<sup>®</sup> version R2007b - Further info at <http://www.mathworks.it/products/matlab/>

## 6.1 HF MIMO simulator steps

The problem of the evaluation of the signal at the receiver site after ionospheric propagation is the key of the HF MIMO simulator presented in this thesis. It is worth remarking that the attention is focused on the range cell where the target is located, without considering the interferences coming from other cells. These interferences are associated to the sidelobes of the range-angle ambiguity function and usually have a severe impact on the radar performance. This topic is of great interest when dealing with OTH MIMO radars and deserves further studies in order to model the interference and include their effects in the proposed simulator.

Under this assumption, the above mentioned problem can be split into two sub-problems, the first that accounts for the propagation from the transmitter to the target and the second that accounts for the propagation from the target to the receiver. In fact, from a propagation perspective, the two sub-problems can be treated in the same way since, in both cases, the problem reduces to finding the available ionospheric paths between two end points, from the transmitter element to the target in the first case, and from the target to the receiver element in the second case.

For this reason, attention will be focused on the problem of the signal propagating from the transmitter to the target, while for the second problem only the differences will be highlighted.

The steps of the HF MIMO simulator for the evaluation of the received signal at the target location are as follows:

1. Define the transmitter geometry and target location, i.e., the end points of the problem, in a proper system of reference
2. Define the set of transmitted waveforms according to the signalling technique selected
3. Select of the start point of the problem, i.e., a transmitter element. At each iteration of the software, a different start point (transmitter element)

is selected in order to evaluate the contributions from all the elements of the transmitter system.

4. Evaluate the ionosphere between the selected start point and end points. During this phase, a plasma frequency grid is created according to the level of disturbances desired.
5. Evaluate the skip distance in order to test if the end point is within the blind region of the radar. If so, the process stops and starts again from point 3 of the present list of steps, selecting a new start point
6. Evaluate the available paths between the start point and the end point via Coleman's raytracing
7. Evaluate ionospheric propagation effects on propagating signals for each of the available path. The signal at the target location is then calculated as in Eq.(5.4).

The above listed points are summarized in a flowchart in Fig.6.1 which explains the steps to evaluate the signal after ionospheric propagation between the two end points.

It should be noted that the evaluation of the signal at the receiver site requires a second application of the above process, in which the target becomes the start point and the elements of the receiver are the end points. So, since the start point is fixed, when no paths are available between the target and the selected receiver element, the simulator selects a new end point (receiver element), rather than a new start point as it happens in the first problem. Moreover, the set of waveforms emitted by the start point, i.e., backscattered by the target, are the waveforms that have travelled along the various available paths from the transmitter elements to the target because of ionospheric multipath (the total number of paths for a radar return are the number of paths to the target from the transmitter times the number of paths from the target to the receiver). At the end, it is important to note that the amplitude of the signals backscattered by the target are scaled by a

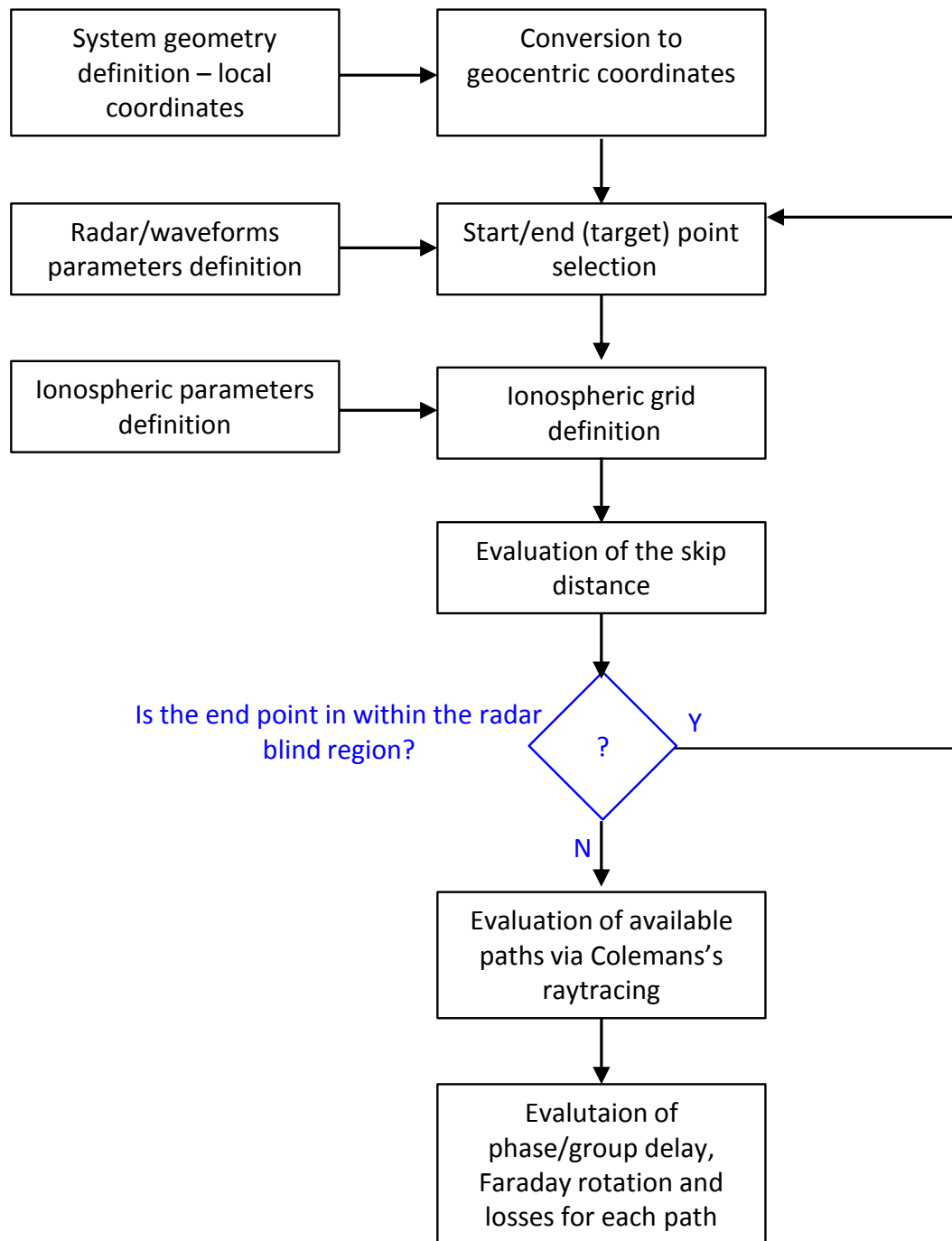


FIGURE 6.1: HF MIMO simulator flow chart

factor that which is proportional to the target RCS.

### 6.1.1 System Geometry Definition

Fig.6.1 clearly shows that the first step consists of the definition of the system geometry in a suitable system of reference. Assume the Earth can be approximated to a sphere and suppose that  $O$  is a point on the Earth's surface, with geocentric coordinates given by  $(\theta_O, \phi_O, R_O)$ , as shown in Fig.6.2(a). Let  $T_p(p, q, r)$  be a local Cartesian system of reference with its center in  $O$  and axes oriented as follows

- the  $p$  axis is oriented towards East along the parallel in  $O$
- the  $q$  axis is oriented towards North along the meridian in  $O$
- the  $r$  axis is the extension of the normal to the Earth's surface in  $O$ .

The local system of reference is used for the system geometry definition. In particular, the number of transmitter elements,  $N_{tx}$ , is defined and the location of the generic  $m^{th}$  element,  $\mathbf{p}_{Tx,m} = (p_{Tx,m}, q_{Tx,m}, r_{Tx,m})$ , is given with respect to the center of the local system of reference. The target location is defined in the local system of reference as well. For the sake of simplicity, the target location is given in spherical coordinates in order to easily select the target range and the orientation with respect to the radar system, as shown in Fig.6.2(b).

The geocentric system of reference is used to set the geographical locations of the radar transmitter and receiver, which are used as input by the raytracing routine to evaluate the available paths as it will be shown in the following.

It can be easily demonstrated that the relationship between the local coordinates and the geocentric coordinates is given by the following

$$\mathbf{x} = \mathbf{x}_O + \mathbf{M}_P \mathbf{p} \quad (6.1)$$

where

- $\mathbf{x}$  is a vector containing the coordinates of the considered point in the geocentric system of reference  $T_x(x, y, z)$
- $\mathbf{x}_O$  is a vector containing the geocentric coordinates of the point  $O$  which coincides with the centre of the local system of reference  $(p, q, r)$
- $\mathbf{p}$  is the vector containing the coordinates of the considered point in the local system of reference
- $\mathbf{M}_P$  is a matrix accounting for the rotation due to the geographical longitude and latitude of the point  $O$ , and it is given by

$$\mathbf{M}_P = \begin{bmatrix} -\sin(\theta_O) & -\cos(\theta_O)\sin(\phi_O) & \cos(\theta_O)\cos(\phi_O) \\ \cos(\theta_O) & \sin(\theta_O)\sin(\phi_O) & \sin(\theta_O)\cos(\phi_O) \\ 0 & \cos(\phi_O) & \sin(\phi_O) \end{bmatrix} \quad (6.2)$$

where  $\theta_O$  and  $\phi_O$  are the longitude and the latitude of the point  $O$ , respectively.

Once the geometry is defined, the transmitter unit within the simulator defines the set of transmitted waveforms, according to the signalling technique desired as seen in Sect.3.1.1.1.

## 6.1.2 Evaluation of available paths

At this point, the simulator separately focuses on each single element of the transmitter array in order to find the paths that link them to the target. The existence, and the number, of available paths is function of the transmitter element and target location and changes according to the ionosphere state as well as to the carrier frequency. In particular, if the target is within the blind region of the radar, there will be no paths available. Consequently, the next operation performed by the simulator is the evaluation of the skip distance in the system bearing direction, in

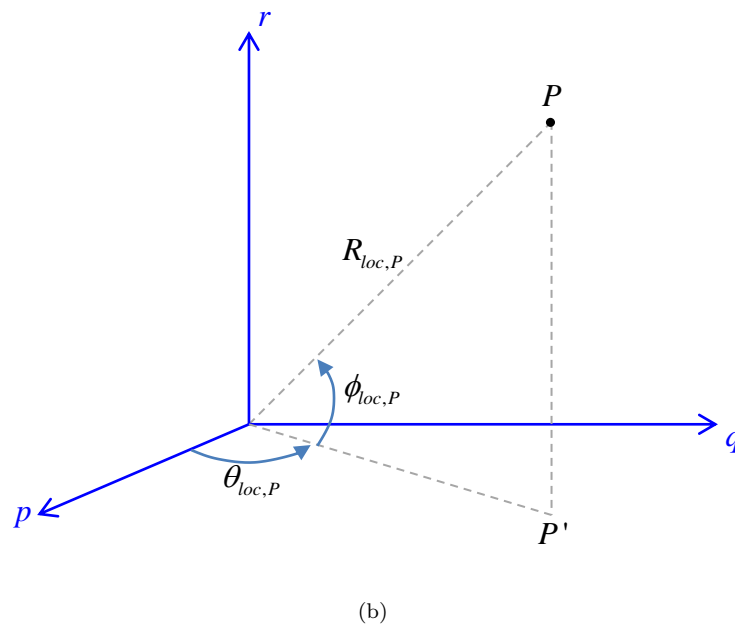
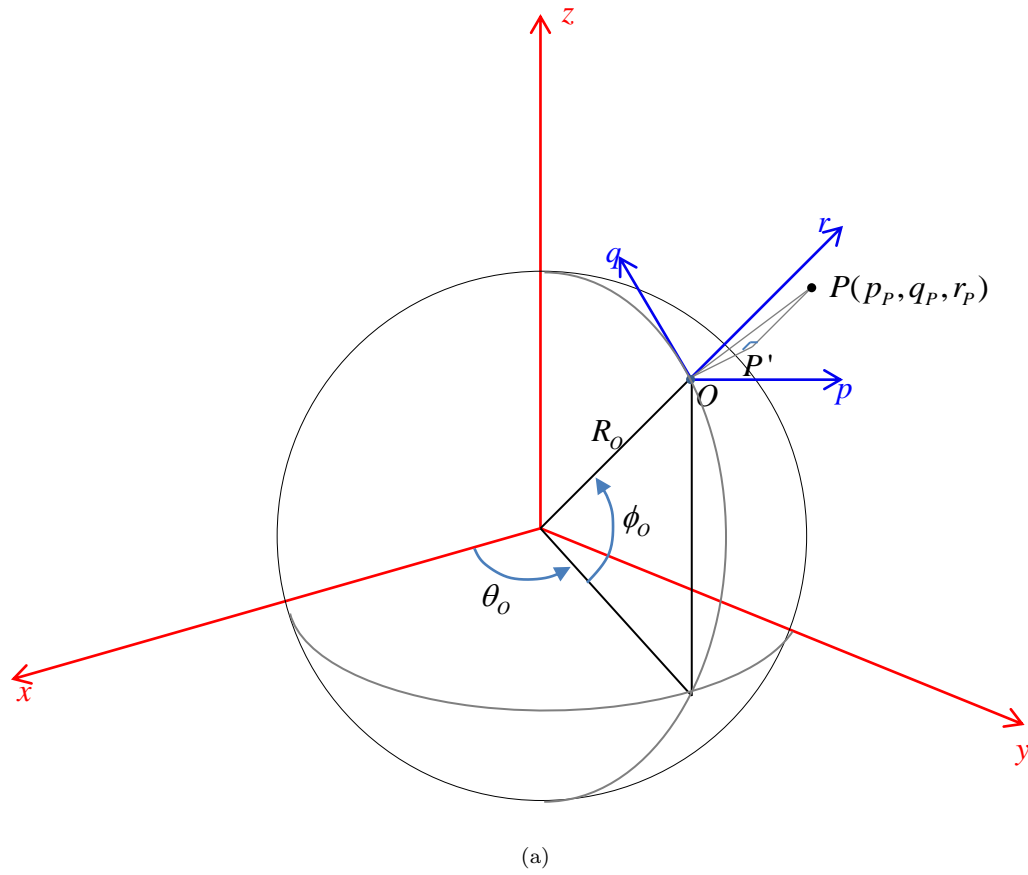


FIGURE 6.2: Representation of the geocentric system of reference  $(x, y, z)$  and the local system of reference  $(p, q, r)$

order to evaluate if the target is in the blind region of the radar system.

The blind region of an HF Skywave MIMO radar is defined to be the region between the transmitter site and the minimum reachable ground range via ionospheric propagation. In fact, as it has been shown in Sect.2.1.2, the ability of the ionosphere of reflecting radio waves depends on the carrier frequency,  $f_0$ , and the incident angle,  $\phi_{inc}$ , of the waves striking into the ionosphere, and the maximum plasma frequency  $f_{pmax}$

$$f_0 \cos \phi_{inc} < f_{pmax} \quad (6.3)$$

This can also be rewritten as

$$f_0 \cos \left( \frac{\pi}{2} - \phi_{el} \right) < f_{pmax} \quad (6.4)$$

where  $\phi_{el}$  is the elevation angle of the emitted radio wave with respect to the ground surface under the approximation of flat Earth's surface, as shown in Fig.6.3.

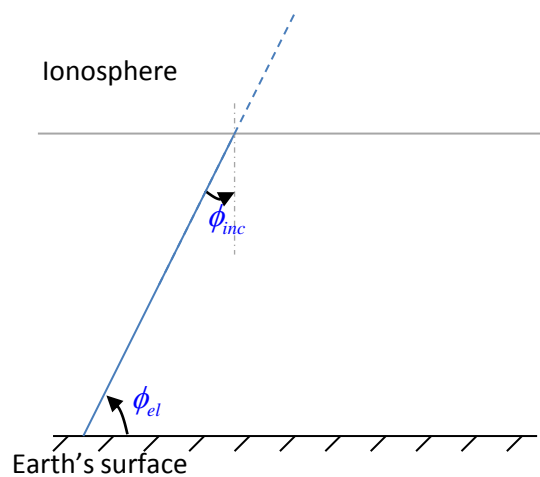


FIGURE 6.3: Elevation angle,  $\phi_{el}$ , and incident angle,  $\phi_{inc}$ , for a radiowave striking into the ionosphere

It is clear that for a fixed carrier frequency  $f_0$ , and a given ionosphere state, as the elevation angle increases the left hand term in Eq.(6.4) increases and the wave is reflected at generally higher altitudes reaching lower ground ranges. The maximum elevation angle which allows for the wave to be reflected correspond to the lowest ground range, i.e., the minimum distance that can be reached via ionospheric propagation, also known as *skip distance*. The skip distance identifies a region that cannot be seen by the radar which is usually referred as *blind region*.

### 6.1.2.1 Ionospheric state definition

In order to evaluate the skip distance, the ionosphere state must be first evaluated. At this stage, the knowledge of the geographical location of the transmitter and the bearing direction of the system is needed in order to evaluate the correct region of the ionosphere. Moreover, the solar activity and the magnetic storm activity must be specified since they affect the electron density and, as a consequence, the frequency supported by the ionosphere. In the simulator, the solar activity is represented by the Sun Spot Number (SSN), which accounts for the intensity of the solar activity and periodically changes accordingly. Typical values of the SSN vary from 0 to 200 <sup>2</sup>. The geomagnetic activity in the Earth's atmosphere, in particular the level of geomagnetic perturbation, is represented by the index  $K_p$  which ranges from 0 to 9 <sup>3</sup>.

The ionosphere in the simulator is described in terms of plasma frequency. In particular, the plasma frequency for the unperturbed ionosphere is defined as a function of the electron content as shown in Sec.2.1.2. The case of perturbed ionosphere is defined starting from the unperturbed case and adding a modulation of the unperturbed plasma frequency as explained in Sec.4.1.3. It has been explained that the raytracing routines is based on the plasma frequency grid as input. This grid defines a *slice* of ionosphere, i.e., a 2D (range-altitude) plane of the ionosphere where each point of the grid coincides with a value of plasma frequency for a specific

<sup>2</sup><http://solarscience.msfc.nasa.gov/SunspotCycle.shtml>

<sup>3</sup>[http://www.ngdc.noaa.gov/stp/geomag/kp\\_ap.html](http://www.ngdc.noaa.gov/stp/geomag/kp_ap.html)

range-altitude pair, as shown in Fig.6.4. This grid is defined for each ray start-end point pair in order to account for the variations of the ionosphere related to geographical changes.

In order to take into account all the aspects which strongly affect the ionosphere, the following parameters are given as input to the routine that evaluates the plasma frequency

- geographical location, i.e., latitude, longitude and altitude, of the start point and of the end point
- bearing direction from the start point to the end point
- the period of the year considered, in particular, the month and the hour of the day
- the level of sun activity and geomagnetic perturbation, in terms of SSN and  $K_p$
- the level of ionospheric disturbances in terms of Atmospheric gravity Waves (AGWs) parameters

Once the Plasma frequency grid has been defined, the raytracing routine can be used to evaluate the skip distance and the available paths.

### 6.1.2.2 Skip distance evaluation

The evaluation of the skip distance is performed by exploiting a raytracing routine implemented by C. J. Coleman. This routine takes as input the ionospheric plasma frequency grid, the start point coordinates, the bearing direction of the system and the elevation of the transmitted waves and returns a table containing the data of each available path. In particular, each path is identified by a number of samples given in terms of local range and altitude. For a given ionospheric state and a fixed carrier frequency, different elevation angle values are used as input for the raytracing routine finding different ground range values.

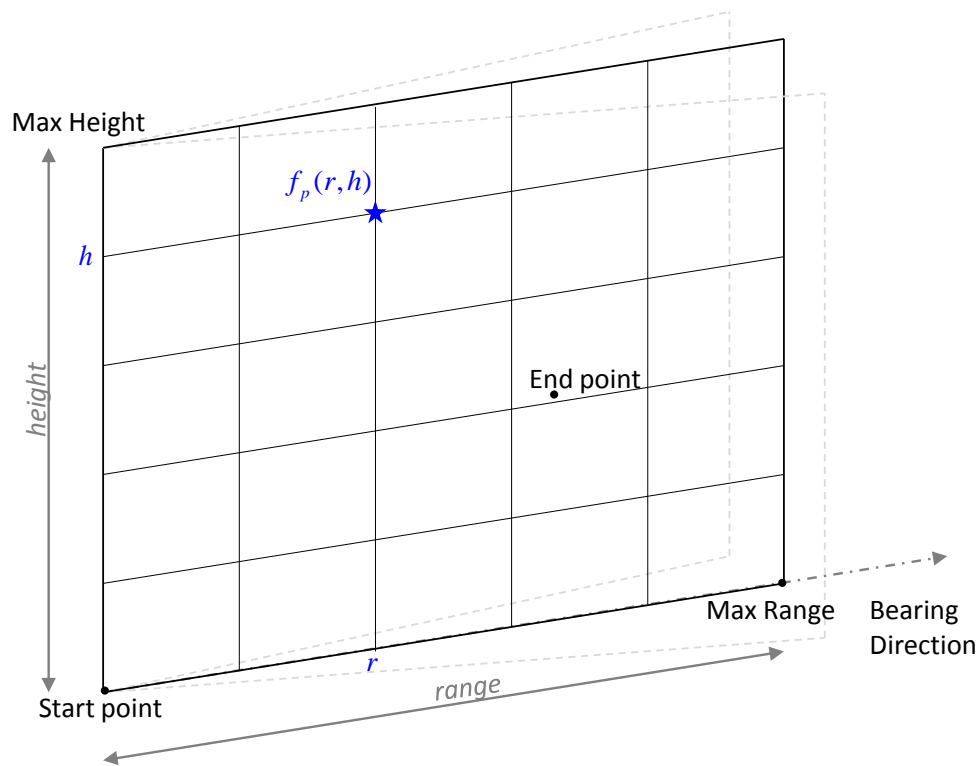


FIGURE 6.4: Plasma frequency grid representation

At this point, the minimum ground range, usually associated to the highest elevation angle, is selected as skip distance and it is used to check if the target is within the blind region.

Unperturbed Ionospheric State Parameters	
Month	3
Hour	12
Minute	00
SSN	150
$K_p$	3

TABLE 6.1: Parameters defining the unperturbed ionosphere

It is worth noting that the blind region strictly depends on the ionospheric state and so it changes on the same time scale as the ionosphere. In Fig.6.5 the skip distance for different frequencies in the HF band at different hours of the day is

<b>AWGs parameters</b>	
Period	300s
Latitudinal and Longitudinal velocity	$0.1 \frac{km}{s}$ $0.02 \frac{km}{s}$
Latitudinal and longitudinal wavelength	500km 100km

TABLE 6.2: AWGs parameters

<b>Tx geographical coordinates</b>	
Longitude	10.3°
Latitude	43.6°

TABLE 6.3: Geographical coordinates of the transmitter site.

<b>Target Local Spheric Coordinates</b>	
Local Longitude, $\theta_{loc}$	60°
Local Latitude, $\phi_{loc}$	5°
Distance, $R_{loc}$	1000km

TABLE 6.4: Target local coordinates.

plotted. The ionosphere state is summarized by the parameters in Tab.6.1 and Tab.6.2, which define the unperturbed ionosphere state and the level of perturbation respectively. The coordinates of the start point and the end points are given in Tab.6.3 and Tab.6.4 respectively.

It will be noted that the value of the skip distance increases with frequency for a fixed hour of the day. This is due to the fact that as the frequency increases, the ionosphere becomes progressively more transparent. When the frequency is larger than the maximum frequency supported by the ionosphere, the wave completely crosses the ionospheric layers and the skip distance tends to infinity. From the same figure it can be seen that for a fixed frequency, the skip distances is bigger during night-time hours. This is due to the fact that during night the electron density in the ionosphere is lower than during day time because of the lack of solar radiation. In this case, the frequency supported by the ionosphere is low so that only few frequencies in the HF range can actually be reflected, as will be noticed

from Fig.6.5. Moreover, the lower the electron density, the higher the wave penetration in the ionosphere and so the higher the skip distance.

It is worth noticing that for low frequencies the skip distance is really low, of the order of tens of kms, because higher elevation angles can be used in transmission, as shown in Fig.6.6. Tab.6.5 shows the values of the elevation of the rays corresponding to the skip distance. Values equal to *NaN* (Not a Number) correspond to the hour/frequency pairs for which the wave completely crosses the ionosphere.

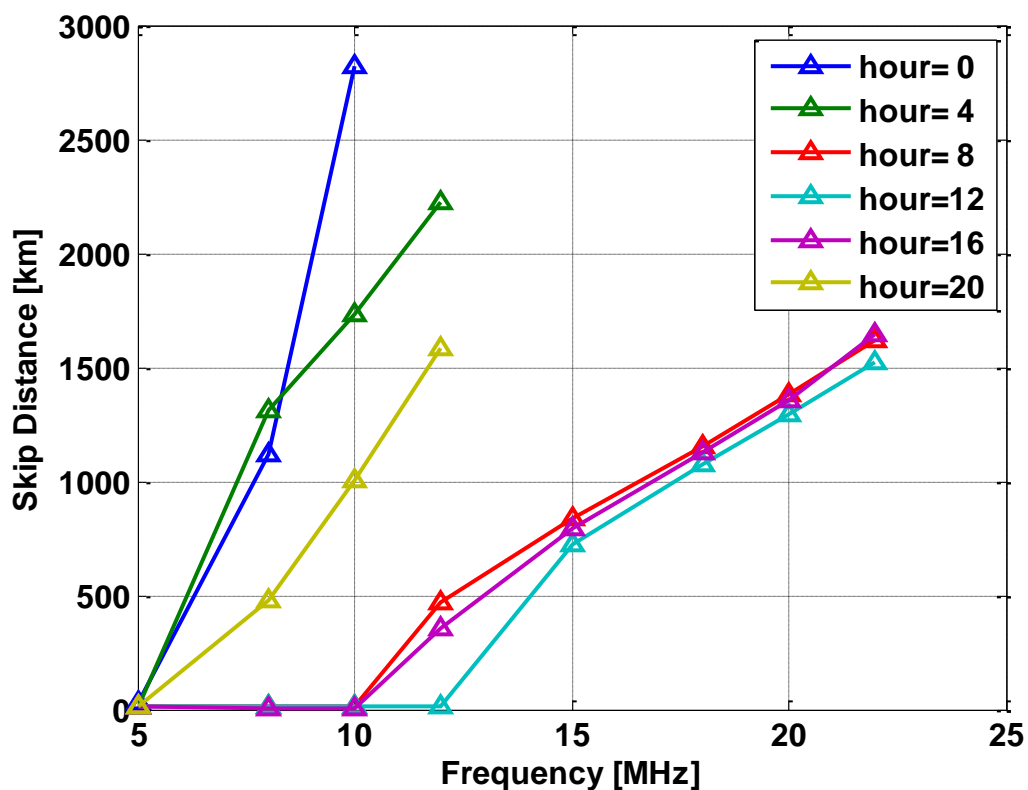


FIGURE 6.5: Skip distance values for a same ionosphere at different hour of the day vs frequency. Missing frequencies in some plots are frequencies that completely cross the ionosphere without being reflected.

Once the skip distance is evaluated, the simulator checks if the target is within the skip distance. If this is so, the simulator selects another transmitter element and evaluates the ionosphere grid between the new start point and the target. It may happen that, according to the transmitter element location with respect to the one considered at the previous step, the ionosphere has changed sufficiently to

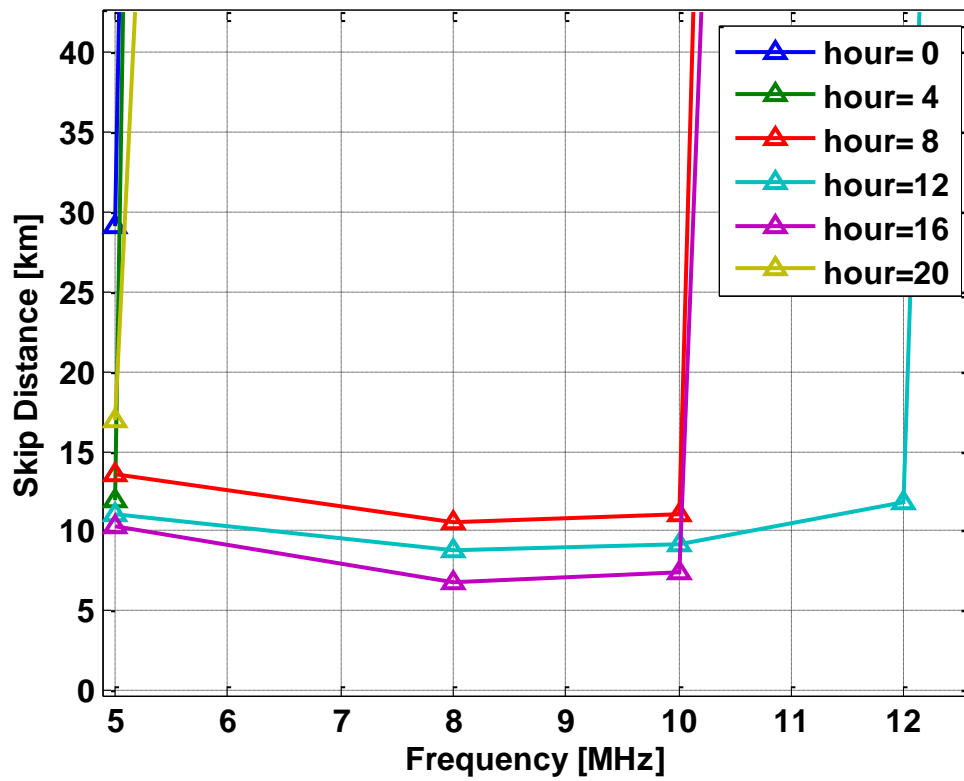


FIGURE 6.6: Zoom of Fig.6.5 for low frequencies.

<i>Frequency</i> [MHz]	5	8	10	12	15	18	20	22
<i>Hour</i> 00	90°	34,9°	9,6°	NaN	NaN	NaN	NaN	NaN
<i>Hour</i> 04	90°	16,1°	10,9°	6,7°	NaN	NaN	NaN	NaN
<i>Hour</i> 08	89,4°	89,8°	89,9°	54,7°	37,8°	28,1°	23,6°	20°
<i>Hour</i> 12	89,5°	89,9°	89,4°	89,5°	48,3°	34,8°	29,1°	24,7°
<i>Hour</i> 16	89,5°	89,8°	89,8°	67,8°	41,8°	30,5°	24,6°	18,5°
<i>Hour</i> 20	90°	61,4°	37,3°	22,9°	NaN	NaN	NaN	NaN

TABLE 6.5: Elevation angle values corresponding to each frequency and hour considered in Fig.6.5

allow propagation.

## 6.2 Preliminary results

During the implementation of the software of the HF MIMO simulator, a number of issues have been tackled which have led to some interesting results that will be shown in the present section.

First of all, it has been noticed that Coleman's raytracing routine which evaluates the available paths between two end points is computationally expensive and leads to very large time processing. With the aim of reducing time processing, simulations have been performed in order to understand whether it is possible to use the linear interpolation to evaluate the signal propagation parameters, such as phase path, group path etc.. In particular, the use of linear interpolation has been analysed in order to evaluate the signal propagation parameters for the various elements of the array and for different frequencies. Before showing the results, it is worth pointing out that the use of linear interpolation is a first simple approach for dealing with the software optimization. Notwithstanding it is obvious that higher order interpolation methods might be appropriate for the estimation of the signal parameters as function of the frequency or as a function of the array dimension. For this reason, further studies are necessary in order to find the most appropriate solution to optimize the software of the simulator and reduce the processing time.

### 6.2.1 Signal parameters vs frequency

This section aims at showing how the phase delay, the group delay, the signal losses and the Faraday rotation change with frequency. In fact, as the carrier frequency increases, the ability of the ionosphere of reflecting radio waves is reduced and all the signal propagation parameters are, somehow, affected. It has been explained in Sec.4.2 that signal losses, especially absorption losses, dramatically increase when the electron density increases. The Faraday rotation, the phase path and the group path are subject to changes as well.

The aim of this section is to show the way the above mentioned parameters change

with frequency and investigate the use of the linear interpolation to approximate and reduce the processing time. Simulations have been performed with both perturbed and unperturbed ionosphere.

### 6.2.1.1 Scenario Definition

Simulations have been performed considering a single transmitter point and a single target point. The signal propagation parameters have been evaluated for a single available path between these two end points for various frequency values in the HF range.

The transmitter point is in the center of a local system of reference (Fig.6.2) and coincides with a point on the Earth's surface with geographical coordinates shown in Tab.6.3. The target is located  $1000km$  away from the transmitter point with local coordinates given in Tab.6.4.

The ionosphere unperturbed state is defined according to the parameters in Tab.6.1, where the month and the hour of the day as well as the parameters defining the Sun activity and the storm activity are shown. The AGW characteristics from which the plasma frequency modulation are shown in Tab.6.2.

The results in Fig.6.7 show the trend of the signal propagation parameters for different frequency values in an unperturbed ionosphere as defined in the previous section. In particular, the real values and the interpolated values are shown on the same figure in order to compare the results. It is evident that the linear interpolation performs well only for the phase path and the Faraday rotation, while the results obtained for the group path and the signal losses are not good. It is worth saying that in case of unperturbed ionosphere, the Faraday rotation is really low and almost constant for all the frequencies in the HF band. Otherwise in case of perturbed ionosphere, as shown in Fig.6.8, the Faraday rotation is very high. However, the linear interpolation cannot be used to evaluate the value of Faraday rotation as it happens for the unperturbed case. Moreover, it can be noticed

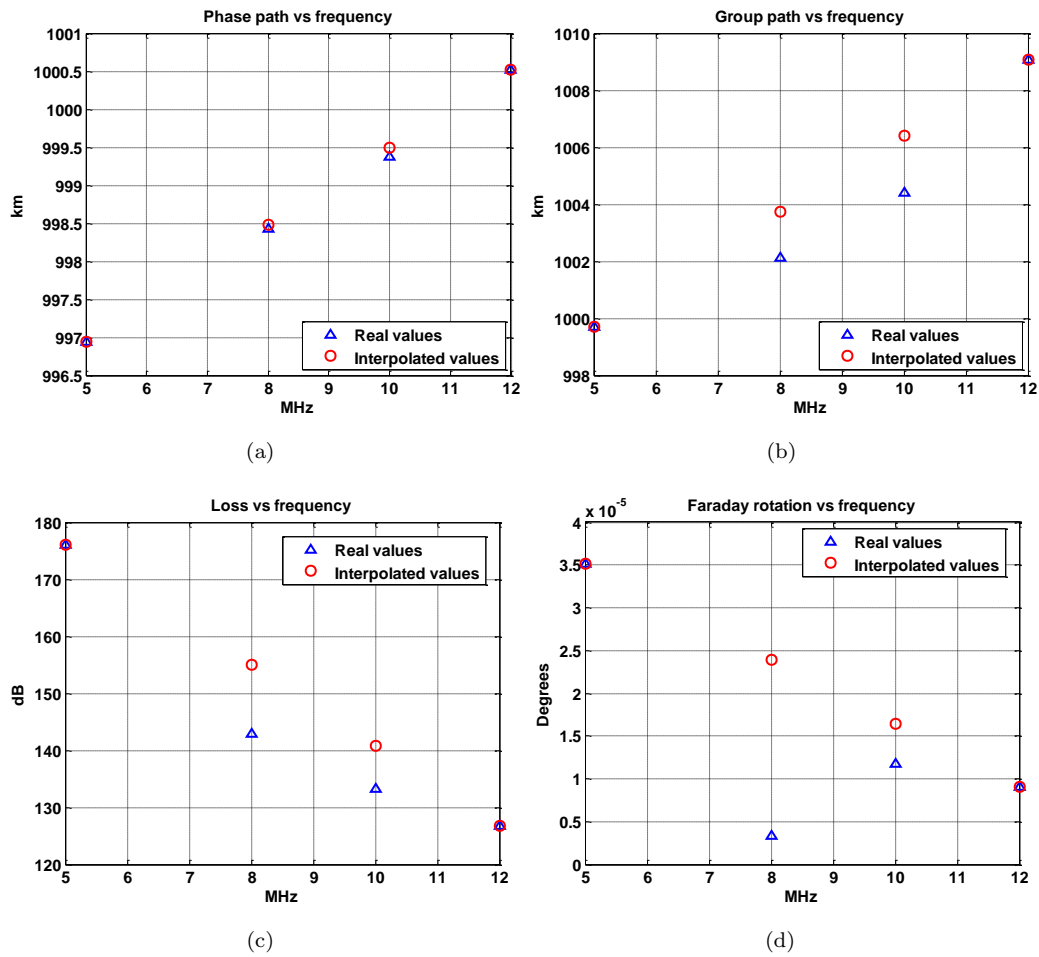


FIGURE 6.7: Phase path (a), group path (b), losses (c) and Faraday rotation (d) trend vs frequency in an unperturbed ionosphere

that as the frequency increases the Faraday rotation decreases according to the theory in Sec.2.1.2. It should be noted that the frequency values in the plots in Fig.6.8 cover only part of the HF range. This is due to the fact that only for those frequencies there are paths available between the start point and the end point.

## 6.2.2 Signal parameters vs array dimension

The aim of this section is to show how the signal propagation parameters change when the array dimension increases.

In fact, it is important to find a bound to the use of linear interpolation in terms of array dimension in order to understand the limitations of the HF MIMO simulator when the linear interpolation is enabled.

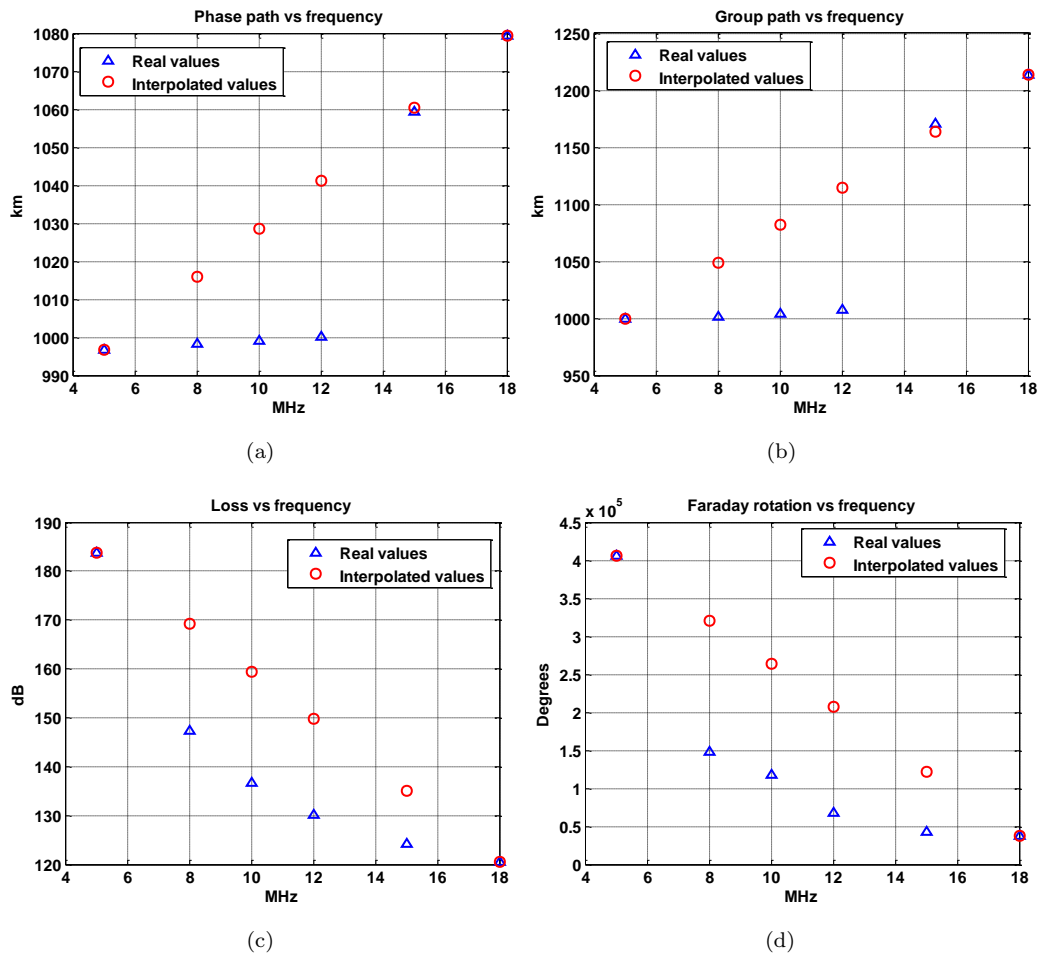


FIGURE 6.8: Phase path (a), group path (b), losses (c) and Faraday rotation (d) trend vs frequency in presence of TIDs.

Most of the simulations have been performed for a perturbed ionosphere, but at the end of this section a simulation for an unperturbed ionosphere will be shown in order to make a comparison.

The simulation scenario is the same described in Sec.6.2.1.1, except for the fact that in this case a Uniform Linear Array (ULA) is considered. The array elements are located along the  $q$  axis of the local system of reference and the centre of symmetry of the array coincides with the centre of the local system of reference. For the sake of simplicity, the number of transmitter elements is fixed,  $N_{tx} = 11$ , while the inter-element spacing,  $d_{tx}$ , changes in order to emulate a different array size. The target location is in Tab.6.4.

Fig.6.9 shows the results for the above described ULA, with  $d_{tx} = 0.5\lambda$ , where  $\lambda$  is the wavelength, which coincides to an array of length equal to  $0.15km$ . As it can

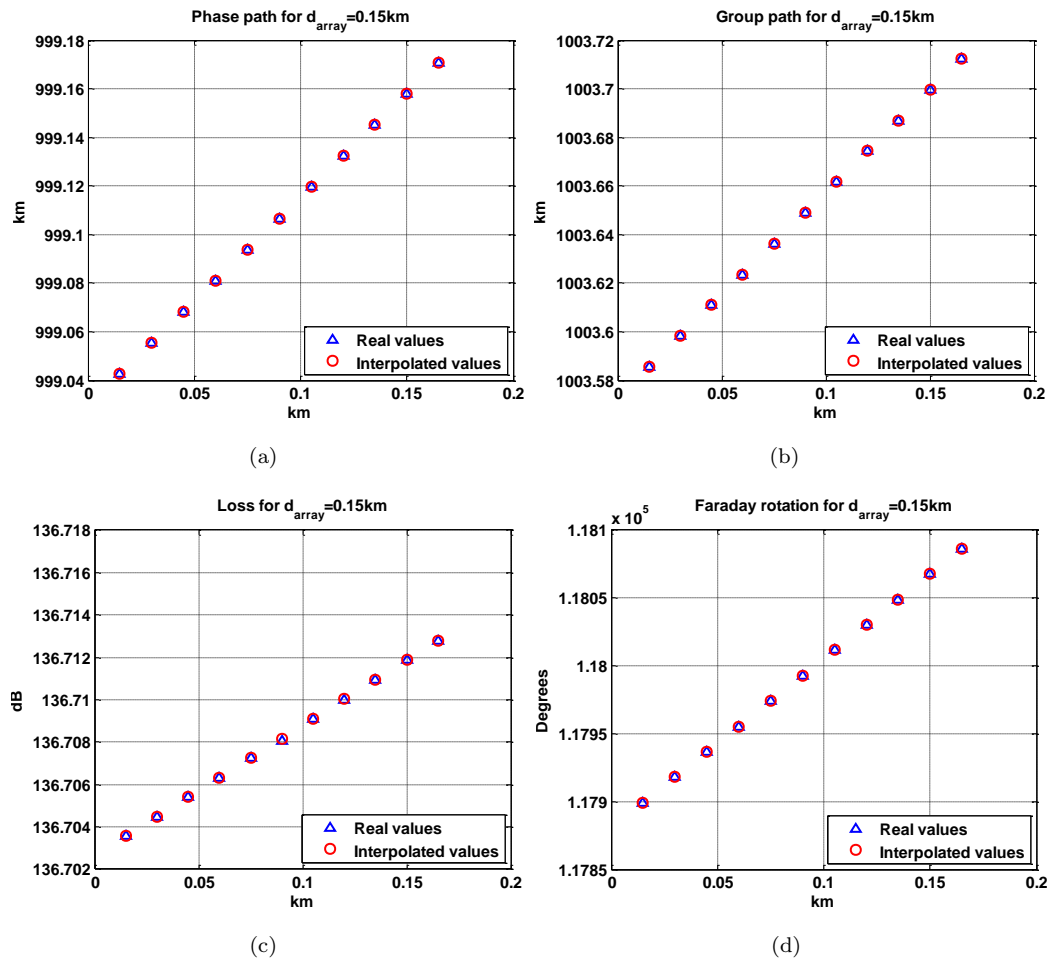


FIGURE 6.9: Phase path (a), group path (b), losses (c) and Faraday rotation (d) trend vs array dimension in presence of TIDs

be noticed, the linear interpolation performs well. The same conclusion can be drawn for an array of length equal to  $1.8\text{km}$ , where only minor errors are present in the evaluation of the signal losses, as shown in Fig.6.10.

For bigger arrays, as shown in Fig.6.11 Fig.6.12, where the array is  $3, 5\text{km}$  and  $18\text{km}$  long respectively, the linear interpolation can still be used for the evaluation of the group delay, phase delay and losses, but it completely fails when dealing with the Faraday rotation. This is likely to be associated with the fact that points that are far away can see a very different ionosphere when looking in a direction so that signals travelling can be subject to very different amount of Faraday rotation. The above described results refer to a perturbed ionosphere. It is useful to show whether the linear interpolation can be used to evaluate the signal propagation parameters in presence of unperturbed ionosphere. As can be seen in Fig.6.11, the

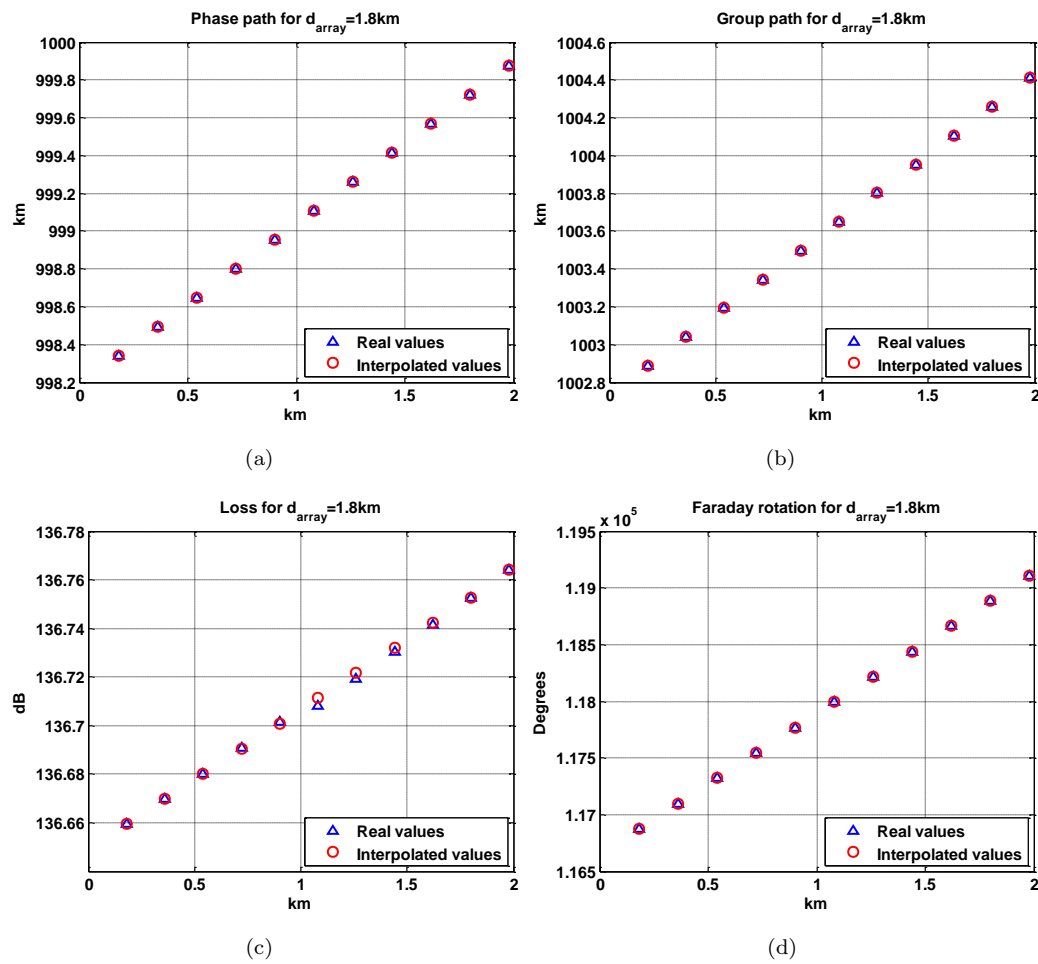


FIGURE 6.10: Phase path (a), group path (b), losses (c) and Faraday rotation (d) trend vs array dimension in presence of TIDs

linear interpolation can still be used with minor errors on the signal losses.

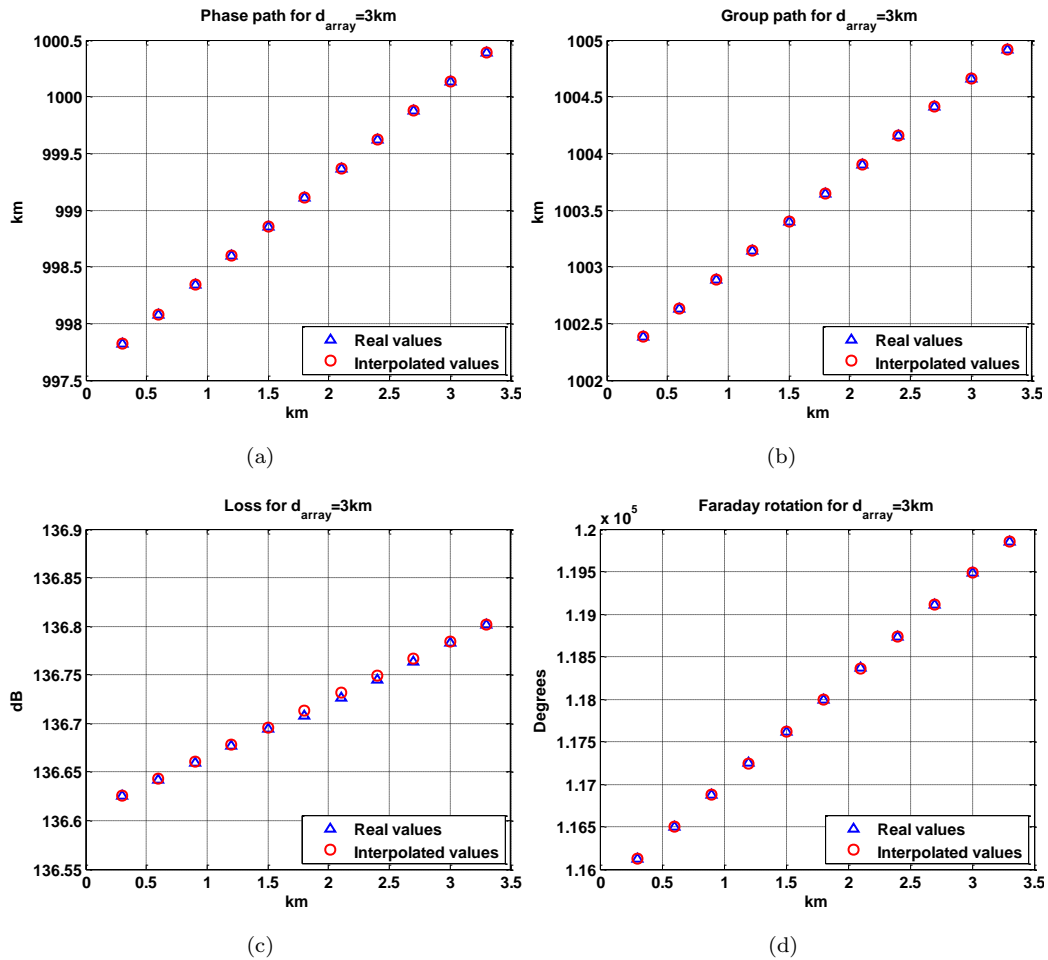


FIGURE 6.11: Phase path (a), group path (b), losses (c) and Faraday rotation (d) trend vs array dimension in presence of TIDs

### 6.3 Summary

The HF MIMO simulator described in the present thesis has been analysed from an operational point of view.

A flowchart has been provided that explains the HF MIMO simulator operation. Each block of the simulator has been analysed in order to give an insight of the operations performed for the evaluation of the signal at the receiver site.

In particular, the evaluation of the skip distance has been described. Simulations have been done in order to show the variations of the skip distance with the frequency in different day hours.

The signal propagation parameters have been analysed in order to find efficiencies in the implementation of the HF MIMO simulator software. In particular, the

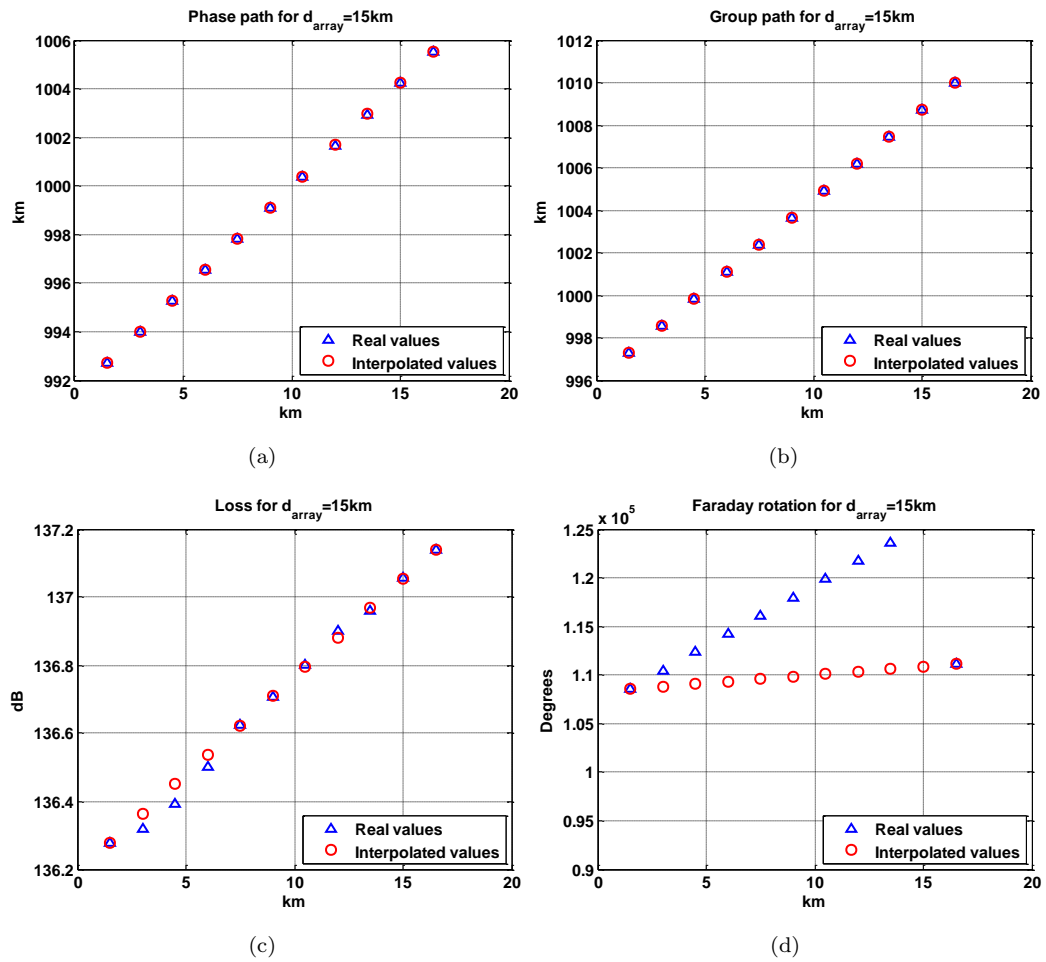


FIGURE 6.12: Phase path (a), group path (b), losses (c) and Faraday rotation (d) trend vs array dimension in presence of TIDs

use of the linear interpolation to approximate the phase path, the group path, the signal losses and the Faraday rotation has been analysed. The results for the case of perturbed and unperturbed ionosphere has been provided showing that in both cases the linear interpolation cannot be used to approximate the signal propagation parameters as the frequency changes. Otherwise, it has been shown that the linear interpolation can be used to approximate the signal parameters for the signals emitted by the elements of the transmitter array. An analysis of the limitation in the array dimension that allows for the linear interpolation to be used has been performed, showing that the results of the linear interpolation are good for phase path, group path and losses even for large arrays while it cannot be used to approximate the Faraday rotation on large arrays. It is possible that a suitable interpolation might work for Faraday rotation in the case of larger arrays

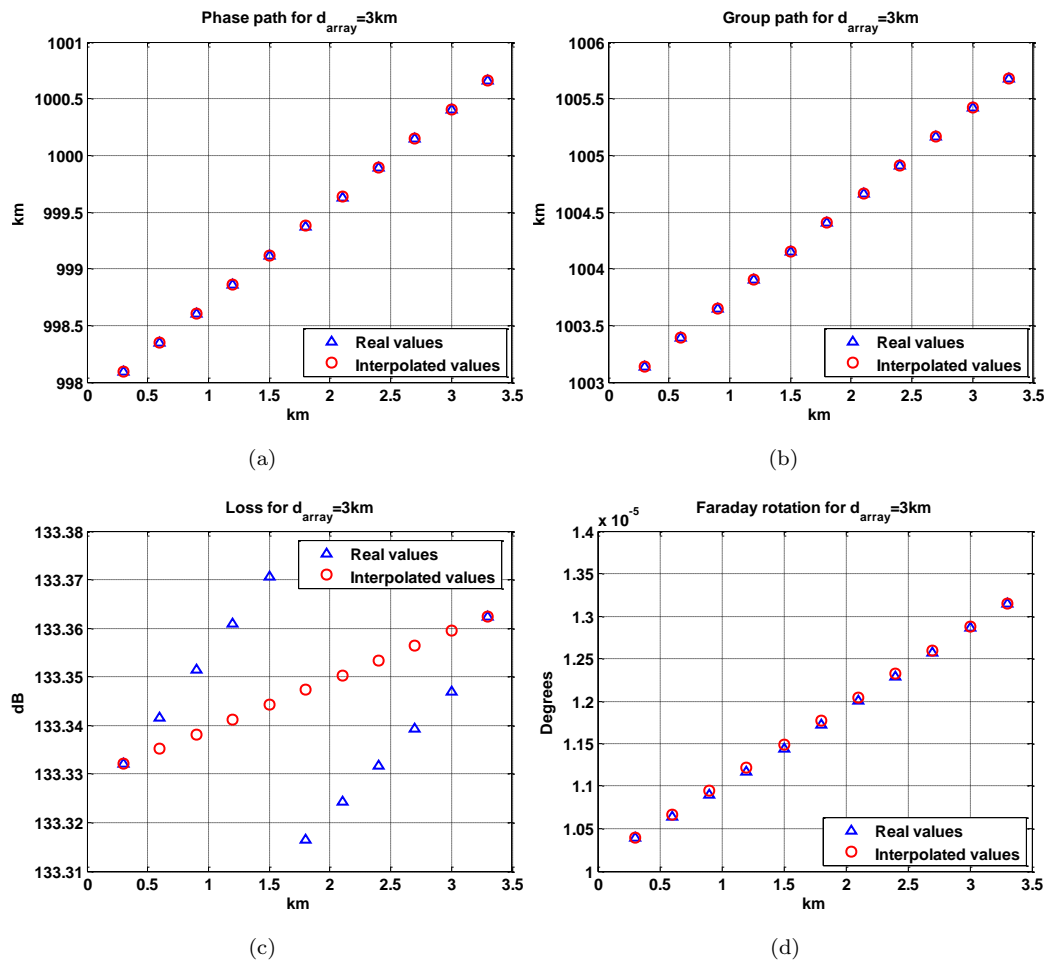


FIGURE 6.13: Phase path (a), group path (b), losses (c) and Faraday rotation (d) trend vs array dimension in an unperturbed ionosphere

and this is an area for further investigation.

# Chapter 7

## Results

The architecture of the HF MIMO simulator presented in this thesis has been described in the previous chapters. In particular, the flowchart of the HF MIMO simulator and the steps performed in order to evaluate the signal at the receiver site have been shown in Ch.6.

The present chapter aims at showing the results of the analysis of the signal at the receiver site. By using the HF MIMO simulator developed in the present thesis, the effects of the ionospheric propagation on waveform orthogonality can be analysed. In fact, when using the ES signalling technique, waveform orthogonality can be analysed via cross correlation matrix at each elements of the receiver.

Moreover, conventional beamforming techniques will be applied in order to estimate the Direction of Arrival (DoA) of the signal.

At the end, the system detection performance will be analysed by means of ROCs according to the model presented in Sec.5.2.

The present chapter is organized as follows. Sec.7.2 will show the results about waveform orthogonality while the output of conventional beamforming will be shown in Sec.7.3. At the end, the detection performance analysis will be shown, both in case of ionospheric multipath presence or absence.

## 7.1 Scenario settings & geometry description

Three different geometries are considered in order to understand whether the system configuration has any impact on the radar performance. The description of the geometries will be given in the next sections.

On regard of the ionospheric state, the TIDs parameters are the same described in Tab.6.1 and Tab.6.2.

### 7.1.1 Geometry 1

The first geometry analysed is the simplest one. Both the transmitter and the receiver are two ULA, oriented along the  $q$  and  $p$  axis of the local system of reference described in Fig.6.2(b). A representation of the system geometry is in Fig.7.1(a) while in Fig.7.1(b) the virtual array element locations that are obtained from the system geometry is shown. As can be noticed, the virtual array is a rectangular filled grid of  $N_{tx} \times N_{rx}$  elements. In this specific case,  $N_{tx} = N_{rx} = 31$  and the inter-element spacing is  $d_{tx} = d_{rx} = 15m$ , that coincides with  $\frac{\lambda_0}{2}$  when  $f_0 = 10MHz$ . In this way, the real array aperture and the virtual array aperture are both equal to  $450m$ .

### 7.1.2 Geometry 2

In this case, the system geometry is circular, and both the transmitter and the receiver are Uniform Circular Arrays (UCA), as schematically represented in Fig.7.2. Both the transmitter and the receiver elements are located on the same ring of radius  $\rho$  and centre in the origin of the local system of reference. The inter-element distance,  $d$  is usually selected such that

$$\frac{d}{\lambda_0} = \frac{1}{2} \tag{7.1}$$

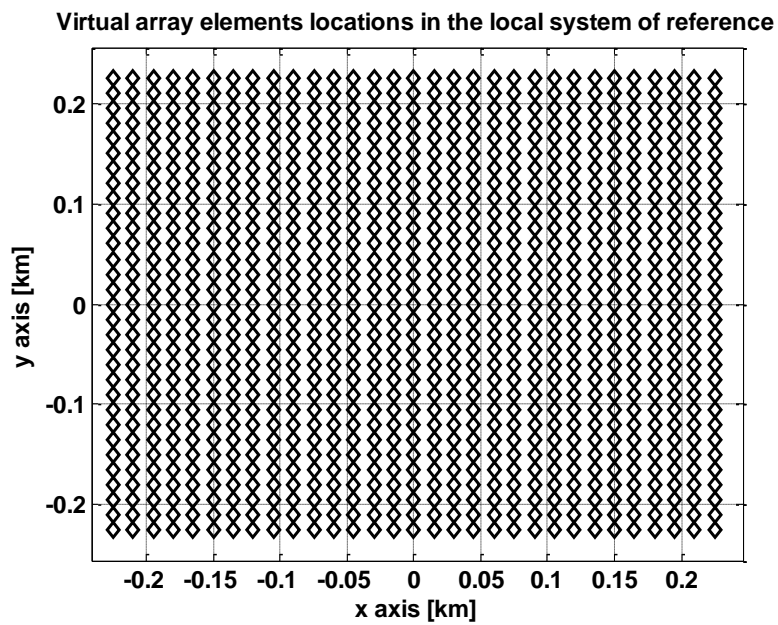
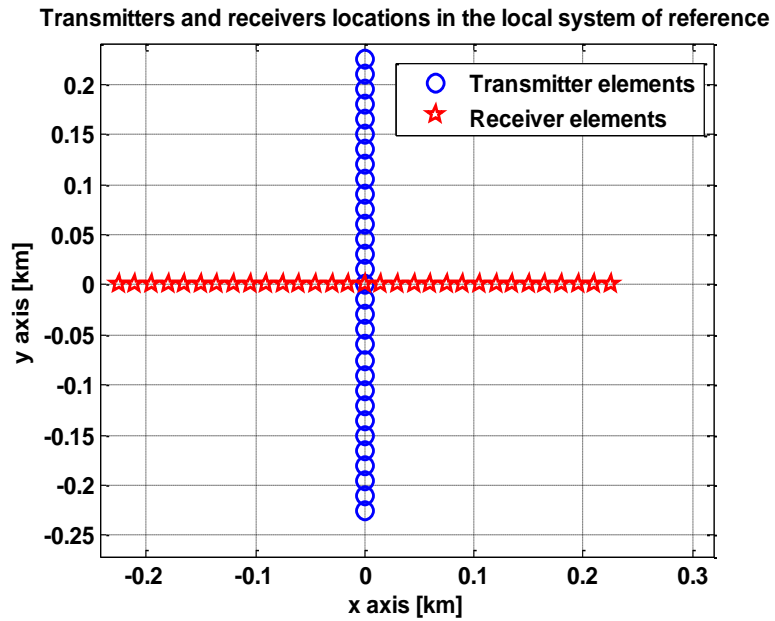


FIGURE 7.1: Representation of the transmitter and receiver location (a) and virtual array elements location (b)

that can be easily rewritten as

$$\rho \sin \left( \frac{2\pi}{N} \right) = \frac{\lambda_0}{2} \quad (7.2)$$

where  $N$  denotes the number of the array elements. Eq.(7.2) can be approximated as

$$\rho \frac{2\pi}{N} = \frac{\lambda_0}{2} \quad (7.3)$$

when  $\frac{2\pi}{N} \approx 0$ . Suppose that the transmitter elements are uniformly distributed on the radius of a ring and that the first element is located on the ring at an angular distance equal to  $d\alpha = \frac{2\pi}{N_{tx}}$  with respect to the  $q$  axis. Suppose that the receiver array has the same number of elements of the transmitter array so that the angular spacing between two consecutive receiver elements is  $d\alpha$ , but the first receiver element is located at an angular distance of  $\frac{3d\alpha}{2}$  with respect to the  $y$  axis, as depicted in Fig.7.3. In this way, the transmitter and the receiver elements are as distant as possible.

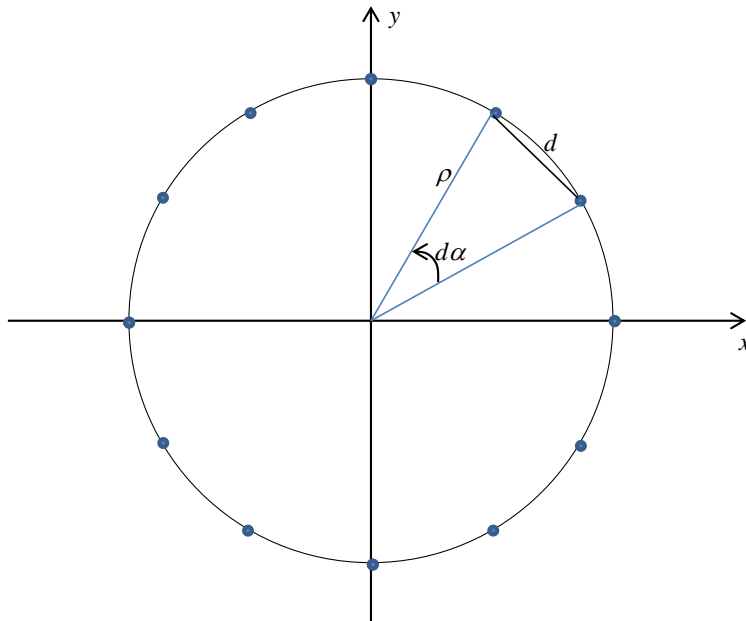


FIGURE 7.2: Geometric representation of circular geometry

It is clear that geometry 1 and geometry 2 are really different so that a criteria must be defined in order to make a fair comparison between the results. In this regard, it has been decided to compare the results of different geometries with the same angular resolution, i.e. the same virtual array aperture. In order to

make sure that geometry 2 has the same aperture of geometry 1, the radius of the ring on which the transmitter and receiver elements of the circular arrays lay has been selected to be equal to  $\rho = 4\lambda_0$ . Under this assumption, the number of array elements that are needed in order to meet the condition in Eq.(7.1) can be easily derived from Eq.(7.2). In this specific case,  $N_{tx} = N_{rx} = 51$ .

As can be noted from Fig.7.4, the virtual array obtained with the geometry in Fig.7.3 has an element in the centre of the ring along which the real elements are located.

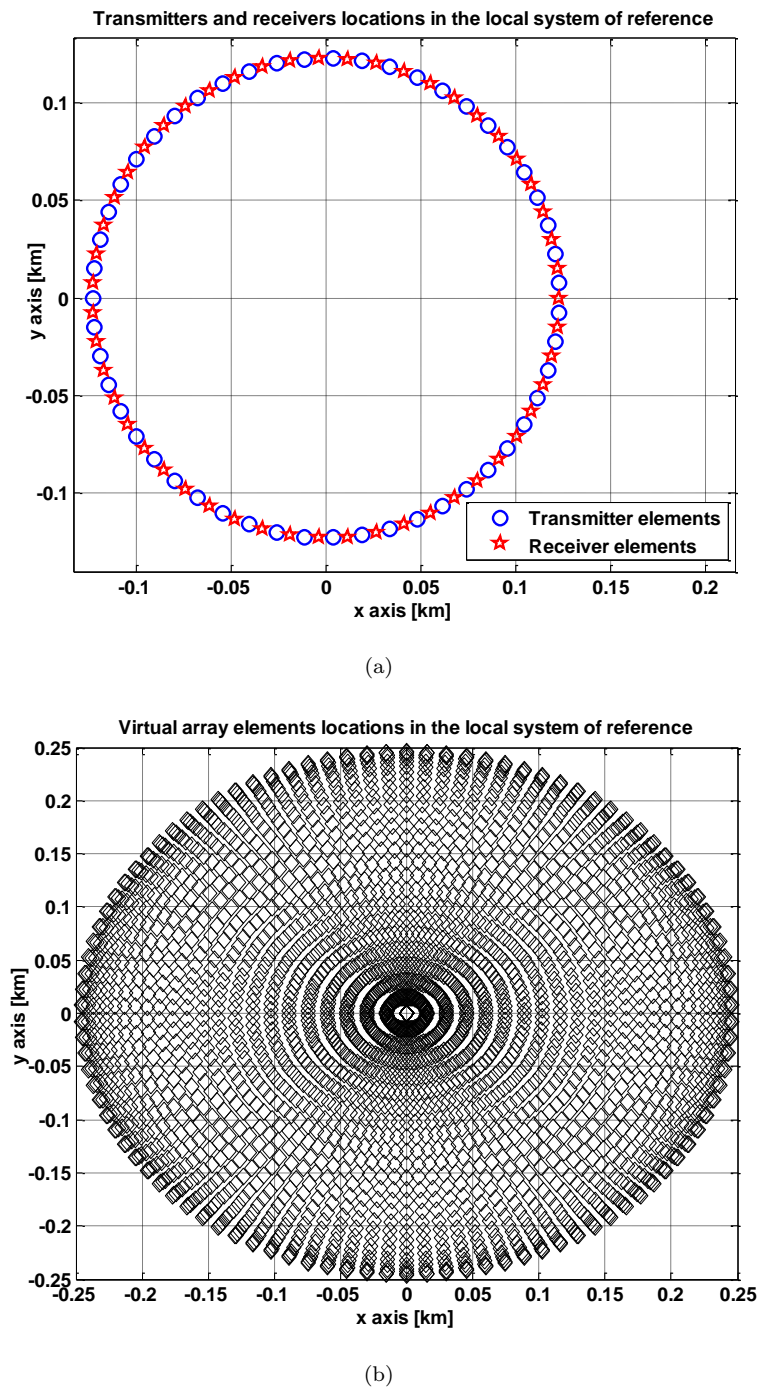


FIGURE 7.3: Representation of the transmitter and receiver locations (a) and virtual array elements location (b)

### 7.1.3 Geometry 3

This configuration is similar to the previous one, except for the fact that the elements of the transmitter and receiver arrays are in the same location on the

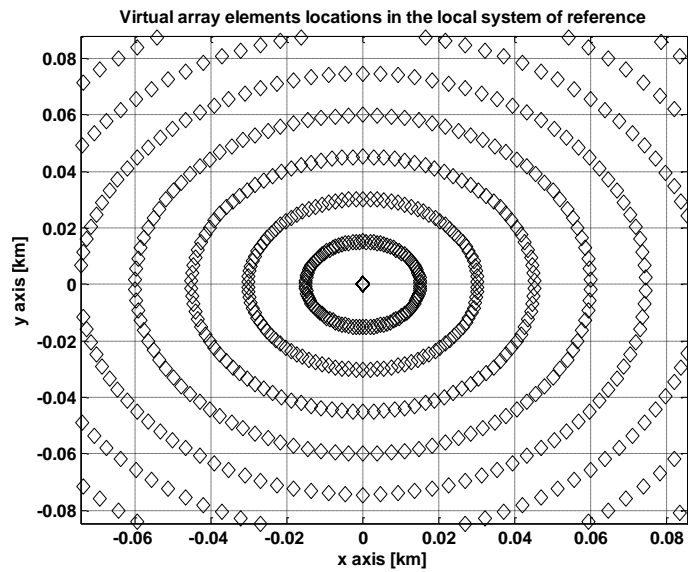
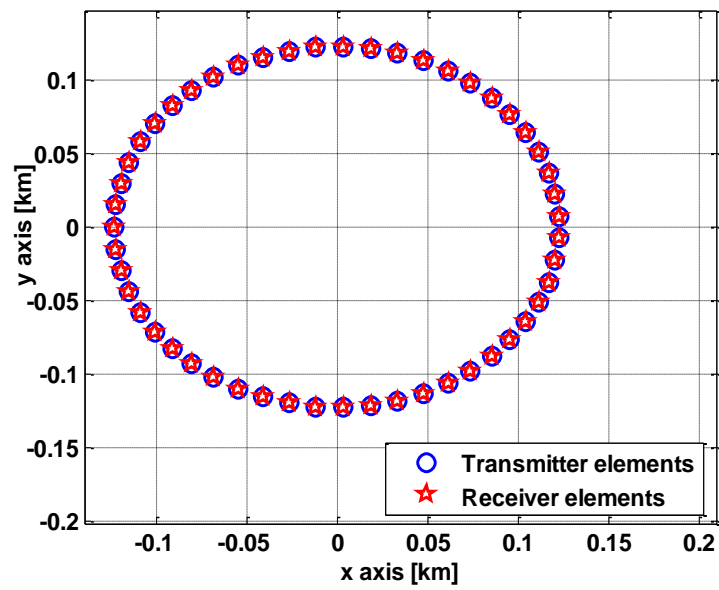


FIGURE 7.4: Zoom of the center of the virtual array represented in Fig.7.3(b). As can be seen the central element is missing.

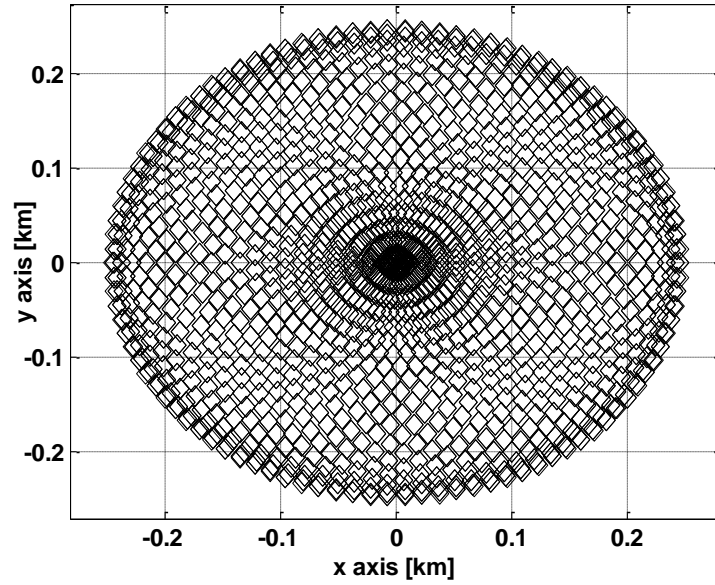
same ring. The main difference with respect to geometry 2 is that the virtual array does not have the central element, as shown in Fig.7.6.

Transmitters and receivers locations in the local system of reference



(a)

Virtual array elements locations in the local system of reference



(b)

FIGURE 7.5: Representation of the transmitter and receiver location (a) and virtual array elements location (b)

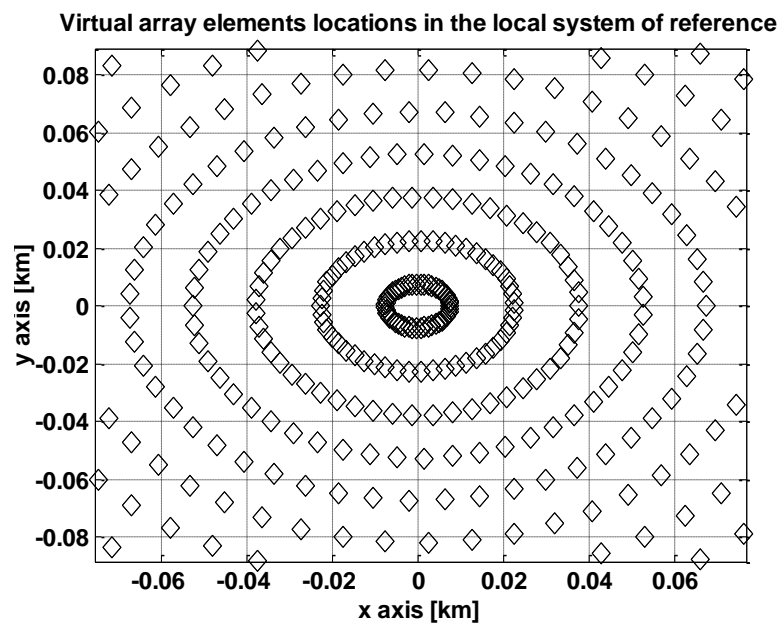


FIGURE 7.6: Zoom of the center of the virtual array represented in Fig.7.5(b).  
As can be seen the central element is missing.

## 7.2 Waveform orthogonality results

It has been shown in the previous chapters that the ionosphere is spatially and temporarily variant on wide scales and that this variability may introduce distortions on the propagating signals.

This section aims at showing the effects of ionospheric propagation on the waveform orthogonality. In fact, it may happen that the distortions induced by the ionosphere affect the transmitted signals in a way such that the orthogonality is not preserved.

In order to measure the orthogonality at the receiver site, the cross correlation matrix of the received signals is evaluated at each elements of the receiver system. In this way, the effects of the ionosphere for different point-to-point combinations can be analysed.

Notwithstanding, simulations performed considering a ionosphere perturbed by TIDs show that at each receiver, the transmitted waveforms after propagation are still orthogonal. Fig.7.7 shows the cross correlation matrix for the received signal contributions at different receiver elements. For the sake of simplicity, only 6 cross correlation matrices out of 31 are shown. As can be easily noticed, the signals after ionospheric propagation are still orthogonal, meaning that the ionosphere perturbed by TIDs does not affect the signal orthogonality. Similar results are shown for geometry 2 and geometry 3 in Fig.7.8 and in Fig.7.9 respectively.

## 7.3 Beamforming results

This section aims at showing the results of the conventional beamforming applied to the signal at the receiver site after ionospheric propagation. In this regard, a number of simulations has been performed for different transmitter and receiver geometries, in order to understand the implications of different system geometries on the Direction of Arrival (DoA) estimation process.

Moreover, it has been shown in Ch.3.3 that ionospheric disturbances effects, in particular TIDs effects, change with time. For this reason, different simulations

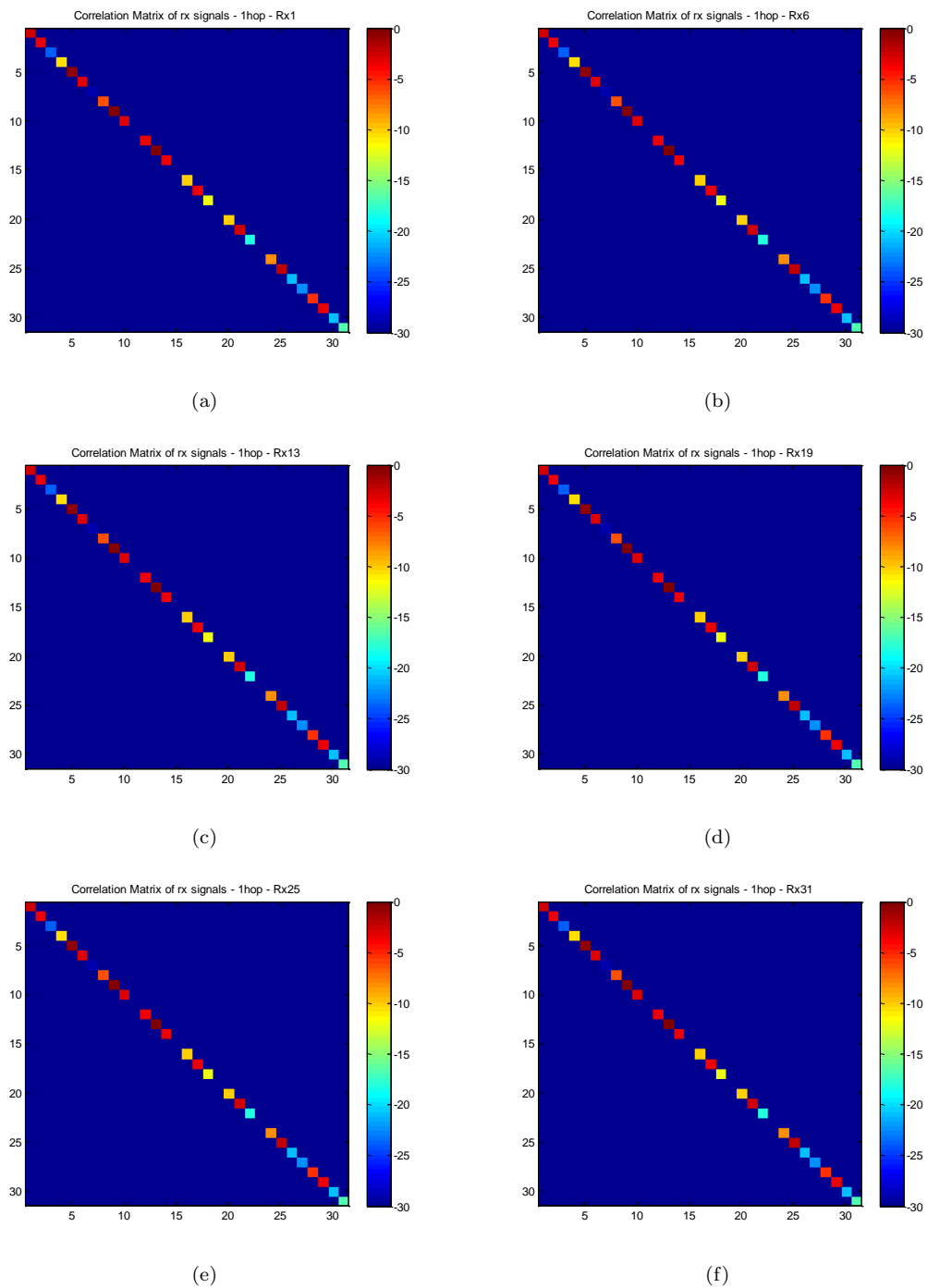


FIGURE 7.7: Cross correlation matrices of the set of transmitted waveforms after ionospheric propagation at the input of the demodulation block for geometry 1.

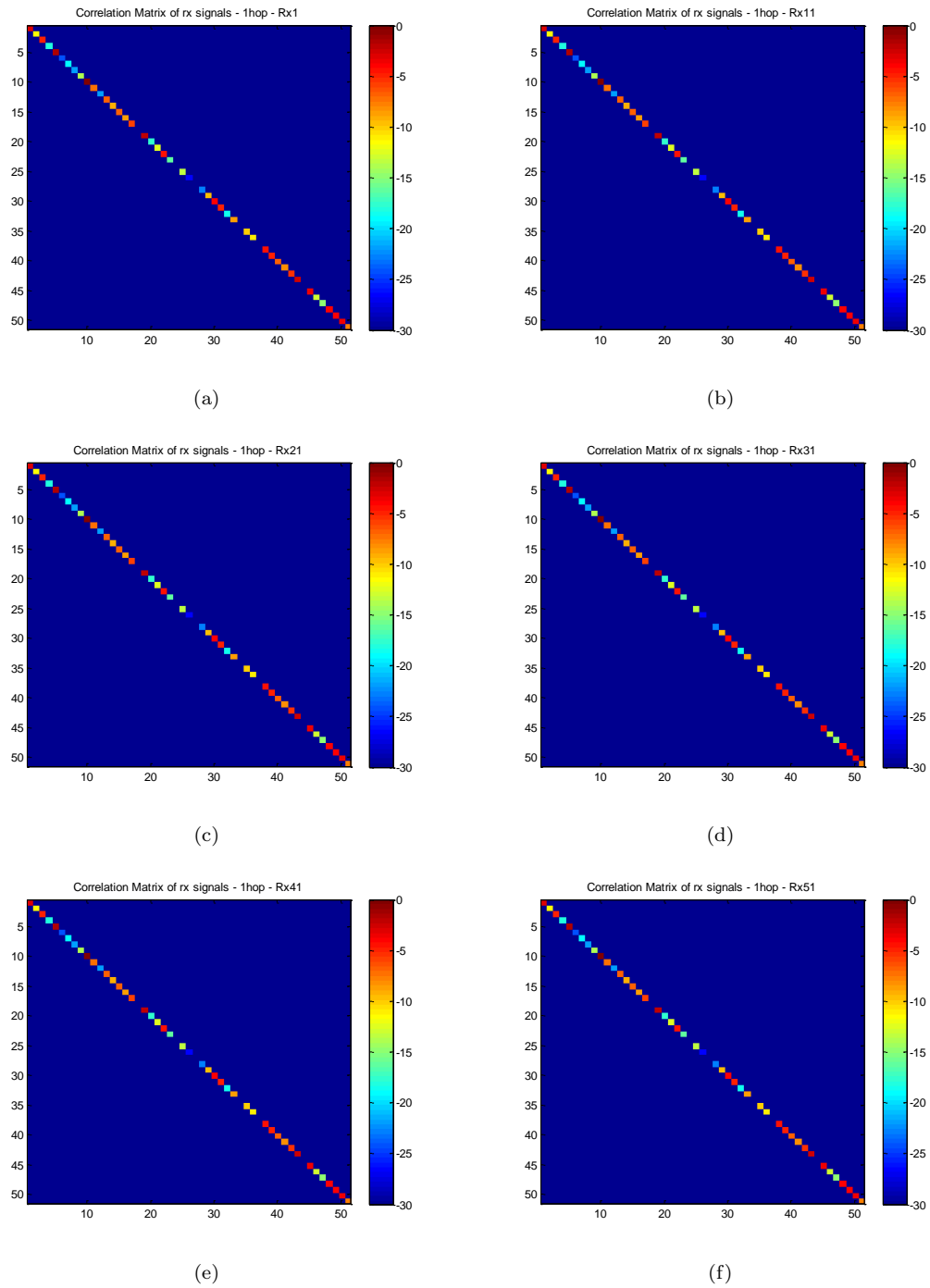


FIGURE 7.8: Cross correlation matrices of the set of transmitted waveforms after ionospheric propagation at the input of the demodulation block for geometry 2.

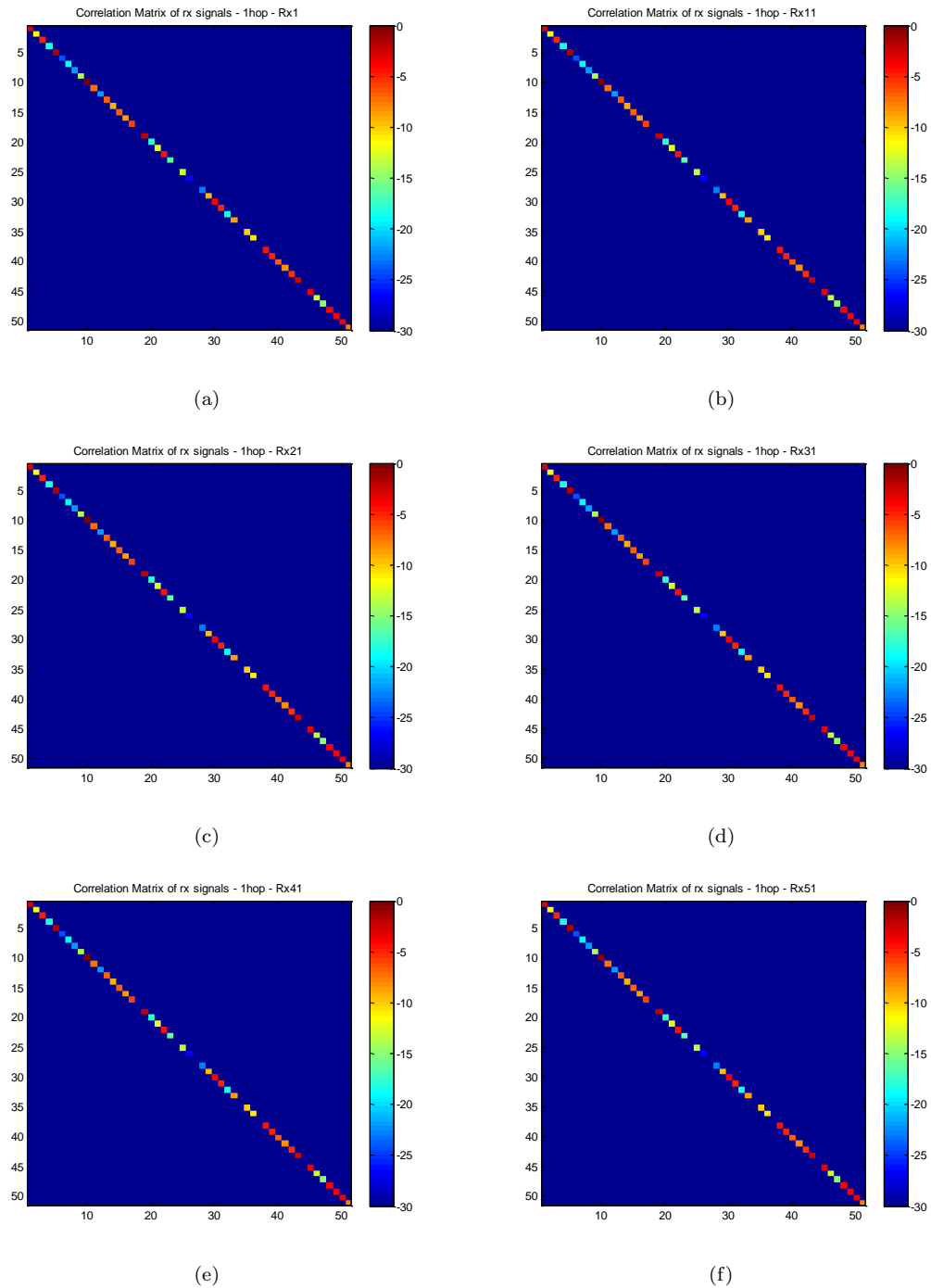


FIGURE 7.9: Cross correlation matrices of the set of transmitted waveforms after ionospheric propagation at the input of the demodulation block for geometry 3.

considering different instant of times within the perturbation period have been performed.

Single hop and two hops propagation has been considered in order to test the HF MIMO simulator. It is worth pointing out that multihop propagation can be considered in the simulator, but the beamforming results have been tested only for no more that two hops since propagation losses can be too strong for real applications.

### 7.3.1 Beamforming for geometry 1

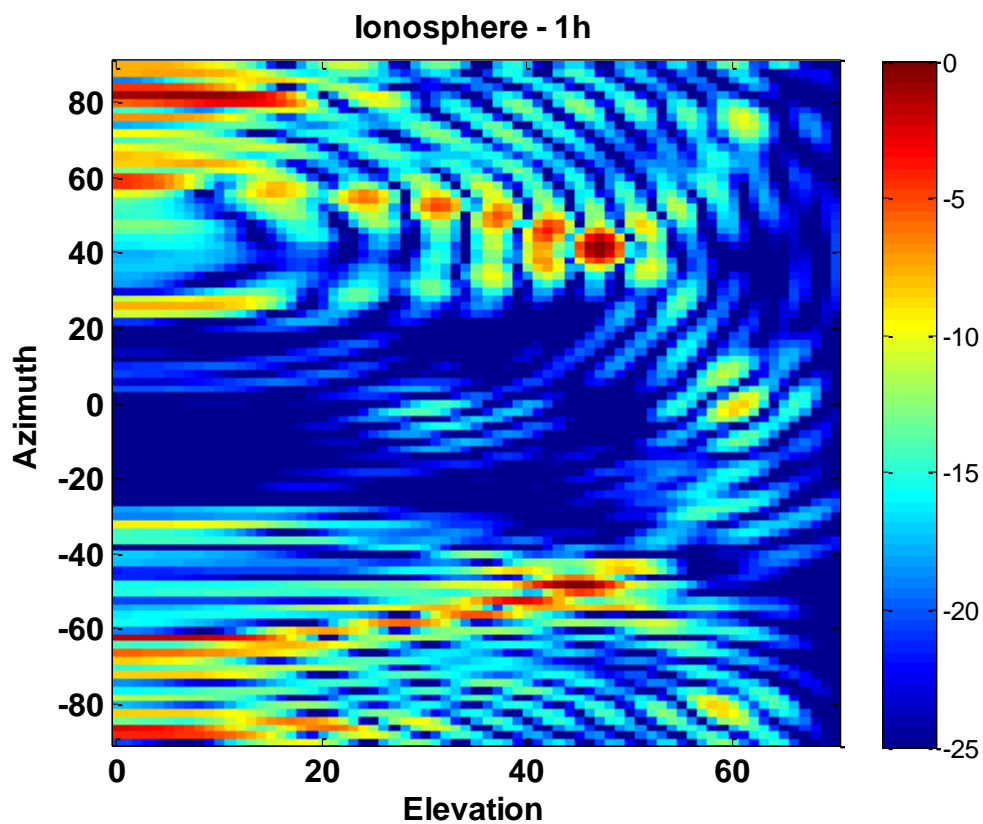


FIGURE 7.10: Result of conventional beamforming for the geometry in Fig.7.1 at time  $t = 0$  with respect to the disturbances period

Fig.7.10 shows the beamforming result in case of perturbed ionosphere at a time coinciding with the beginning of the perturbations period, say  $t = 0$ . As can be noticed, the signal is detected in the right position, but distortions are present. These distortions are due to the high losses and attenuations experienced by the transmitted signals during ionospheric propagation. In order to have an idea of

the amount of signal loss, a matrix with  $N_{rx}$  rows and in which each row coincides with the diagonal of the signal correlation matrix evaluated at the corresponding receiver element is built, as depicted in Fig.7.11.

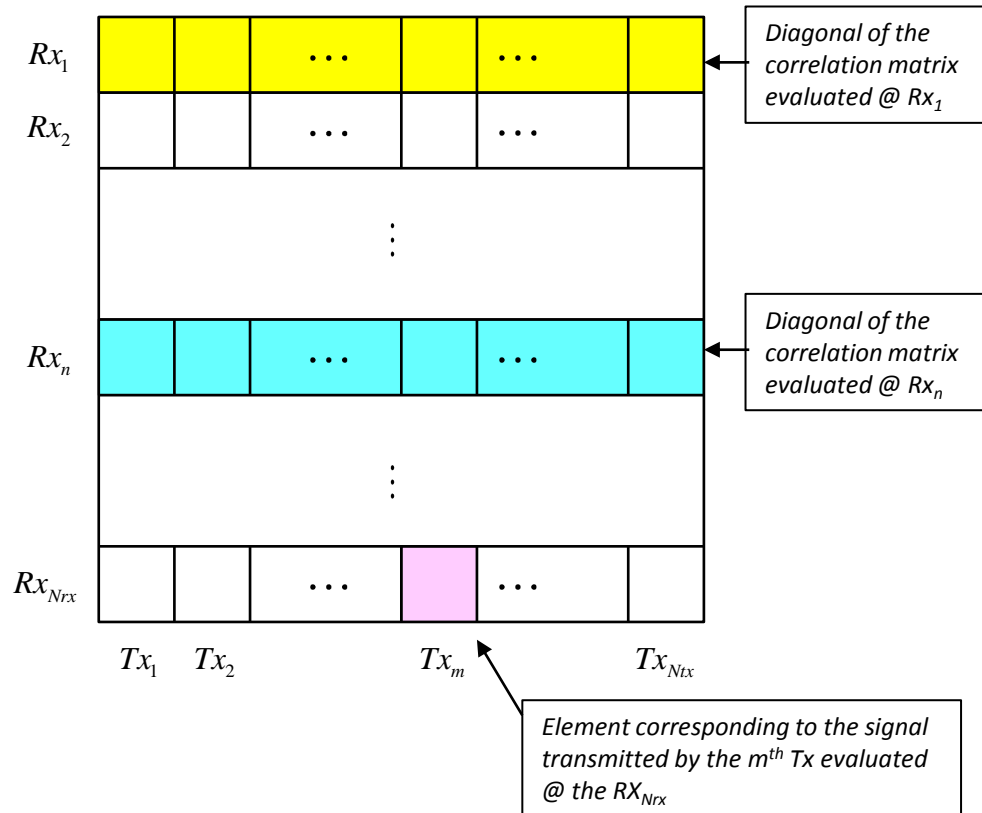


FIGURE 7.11: Result of conventional beamforming for the geometry in Fig.7.1 at time  $t = 0$  with respect to the disturbances period

Fig.7.12 shows a matrix built with the diagonals of the correlation matrices evaluated at the receiver elements of geometry 1. As can be noticed, the signal transmitted by the transmitters 18, 24, 34 and 45 are almost completely lost by all the receiver elements. Moreover, it can be seen that the level of the signal received by some elements of the receiver array, such as element 1, 4, 11, 14, 17 and others that can be clearly identified in the figure, is really low. The dynamic of the correlation matrix depicted in Fig.7.12 is between  $0dB$  and  $-60dB$ . Since the signal at the receiver coincides with the signal received by a virtual array (see Sec.2.2.2), the lack of signals in the matrix shown in Fig.7.12 can be interpreted as the lack of some of the elements of the virtual array.

The beamforming results are analysed in terms of estimated DoA, which coincides

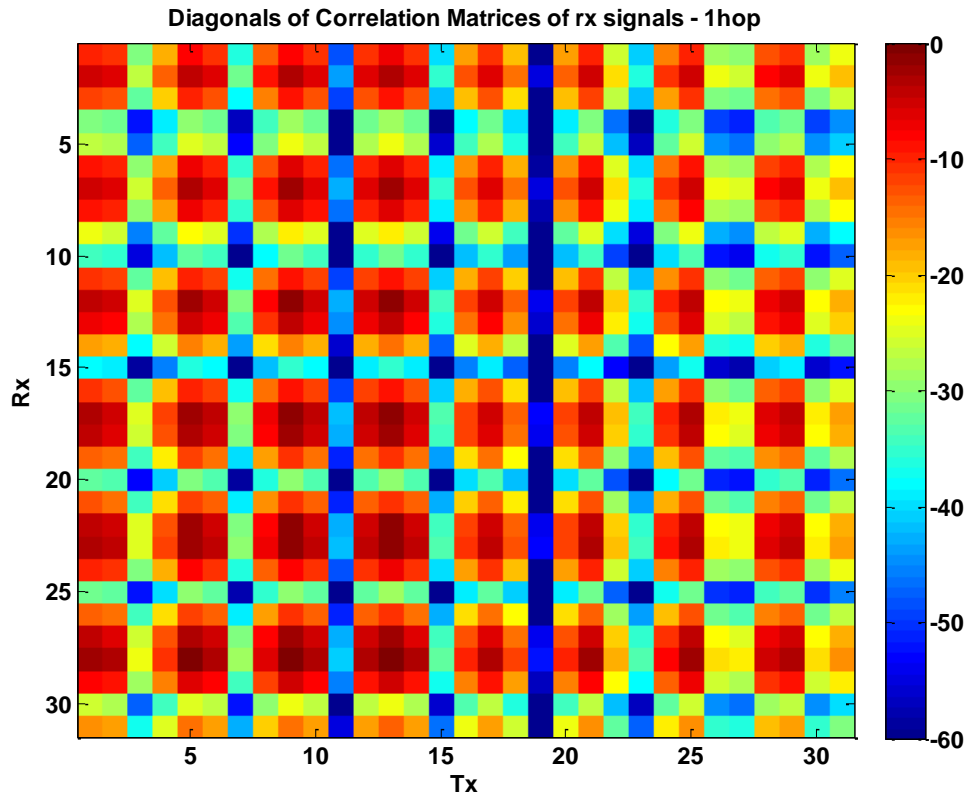


FIGURE 7.12: Result of conventional beamforming for the geometry in Fig.7.1 at time  $t = 0$  with respect to the disturbances period

with the angular location of the main lobe ( $\theta_{az-ML}, \phi_{el-ML}$ ), location and amplitude of the highest sidelobe, ( $\theta_{az-SL1}, \phi_{el-SL1}$ ) and  $A_{SL1}$  respectively, and number of sidelobes higher than  $-10db$ ,  $N_{SL} > -10dB$ . All the above mentioned parameters are in Tab.7.1, which contains the results for the three different instants of time within the TIDs period.

Geom.1 1H			
	$t = 0sec$	$t = 300sec$	$t = 500sec$
$(\theta_{az-ML}, \phi_{el-ML})$	$(45^\circ, 48^\circ)$	$(56^\circ, 32^\circ)$	$(62^\circ, 2^\circ)$
$(\theta_{az-SL1}, \phi_{el-SL1})$	$(-82^\circ, 8^\circ)$	$(52^\circ, 27^\circ)$	$(74^\circ, 10^\circ)$
$A_{SL1} [dB]$	-0,5604	-1,016	-1,871
$N_{SL} > -10dB$	> 10	> 20	> 10

TABLE 7.1: Angular location of main lobe (ML), angular location and amplitude of highest sidelobe (SL1) and number of sidelobes higher than  $-10dB$

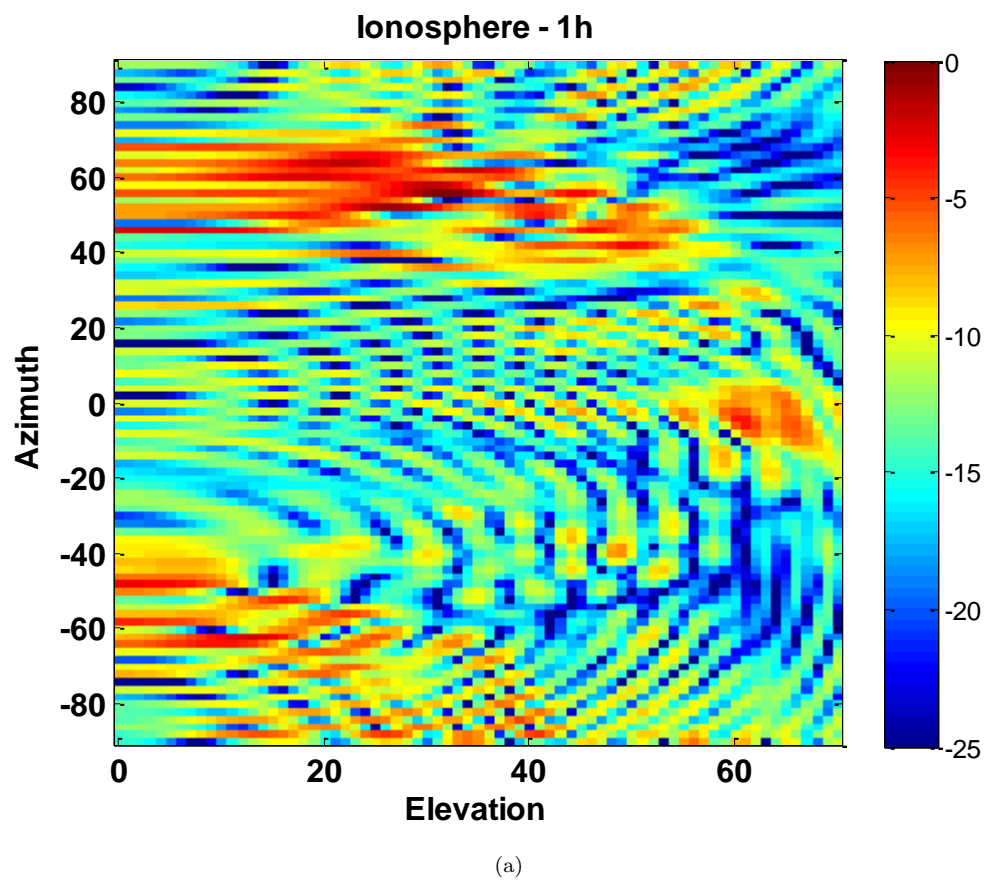


FIGURE 7.13: Result of conventional beamforming for the geometry in Fig.7.1 at time  $t = 300$  with respect to the disturbances period

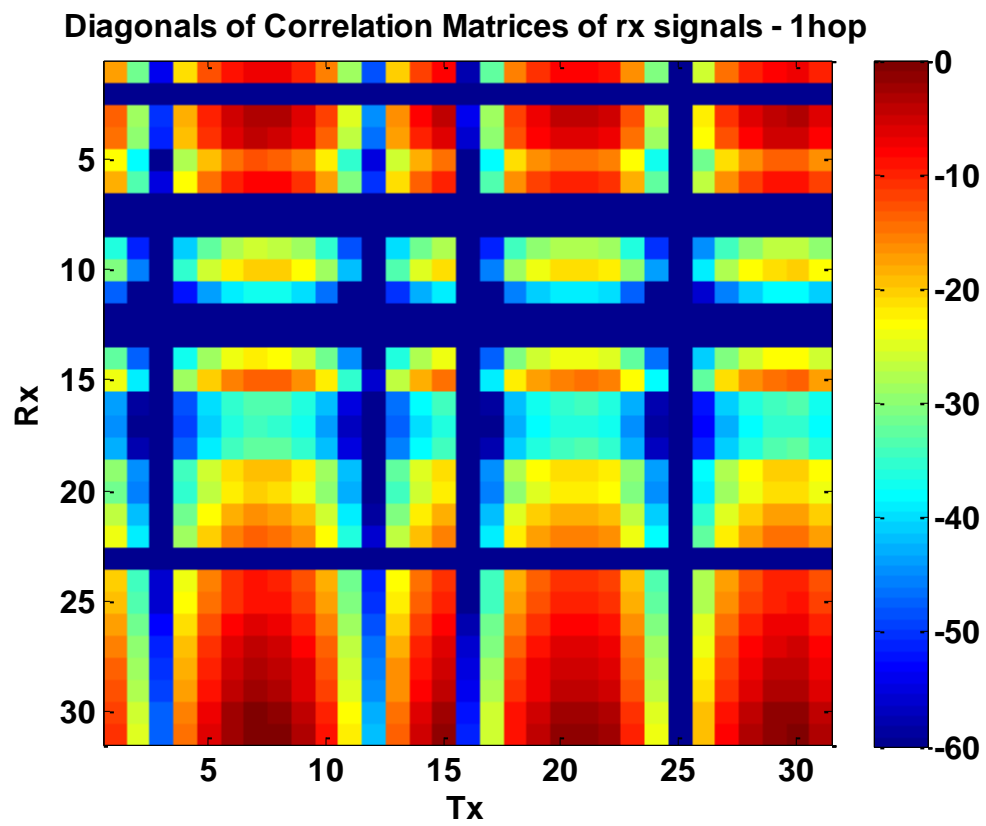


FIGURE 7.14: Result of conventional beamforming for the geometry in Fig.7.1 at time  $t = 300$  with respect to the disturbances period

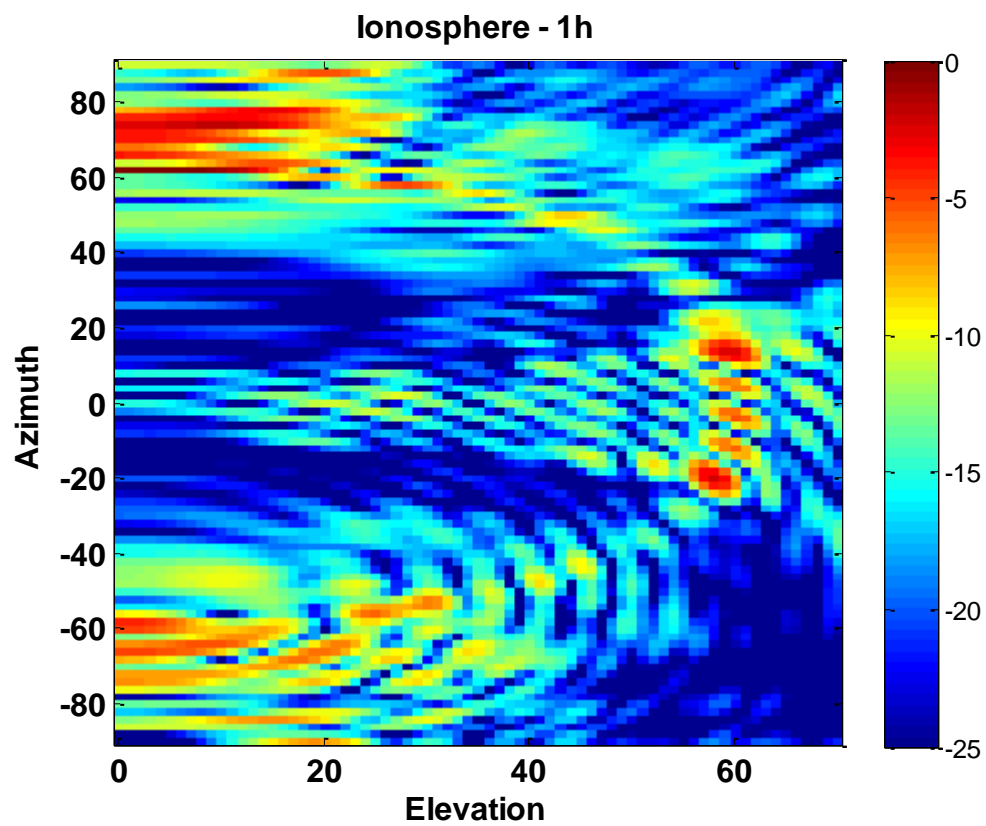


FIGURE 7.15: Result of conventional beamforming for the geometry in Fig.7.1 at time  $t = 500$  with respect to the disturbances period

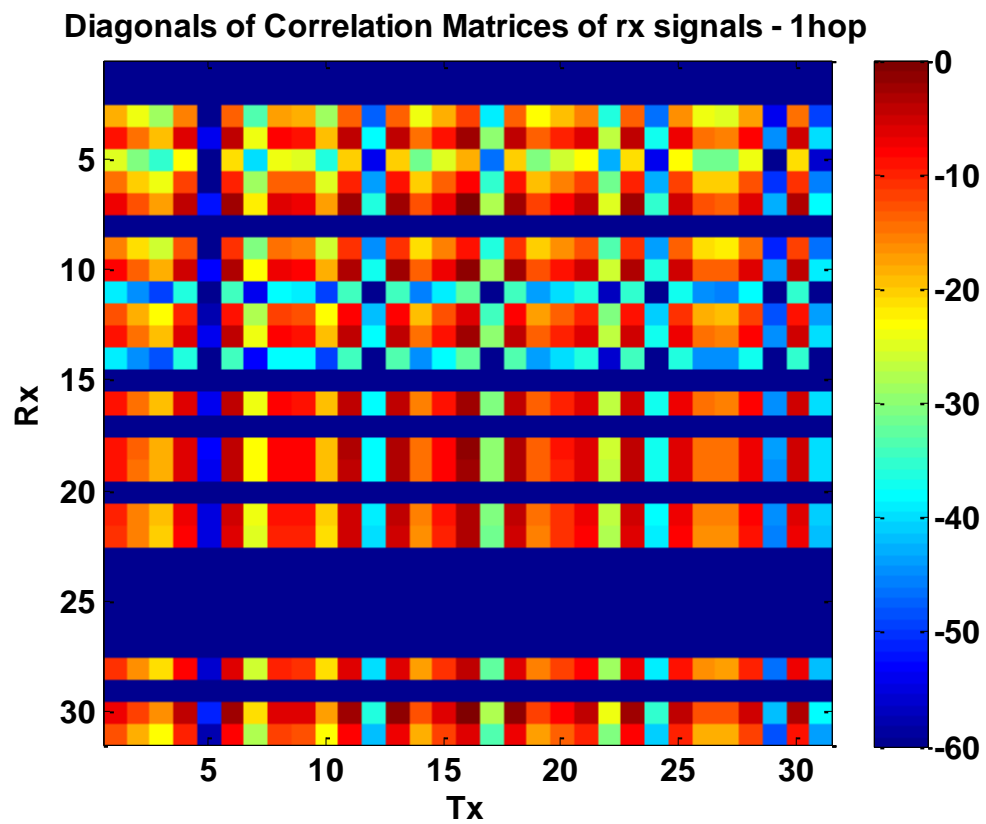


FIGURE 7.16: Result of conventional beamforming for the geometry in Fig.7.1 at time  $t = 500$  with respect to the disturbances period

### 7.3.2 Beamforming for geometry 2

The results of conventional beamforming for geometry 2 at time  $t = 0$  are in Fig.7.17. As can be noted, the signal is detected at the right angular location even though disturbances are present. Similar results are depicted in Fig.7.19 and Fig.7.21 for different time instants. The corresponding matrices that allow for the results interpretation in terms of missing signals are in Fig.7.18, Fig.7.20 and Fig.7.22. Even for geometry 3, it can be easily noticed that the DoA is almost correctly estimated, but very high sidelobe and disturbances are present. This is most likely to be associated with the high level of signal corruption due to the ionospheric degrading phenomena. Tab.7.2 summarizes the beamforming results in terms of number of sidelobes higher than  $-10dB$ , amplitude and angular location of the highest sidelobe and location of the mainlobe.

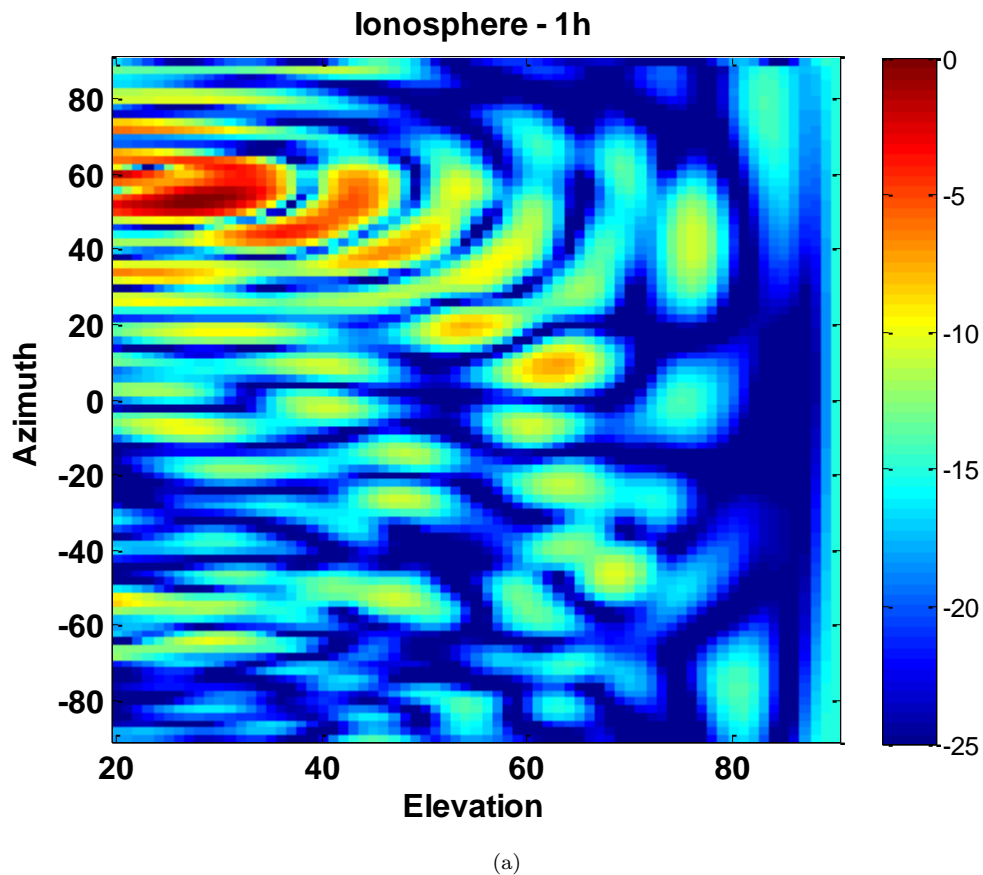


FIGURE 7.17: Result of conventional beamforming for the geometry in Fig.7.3 at time  $t = 0$  with respect to the disturbances period

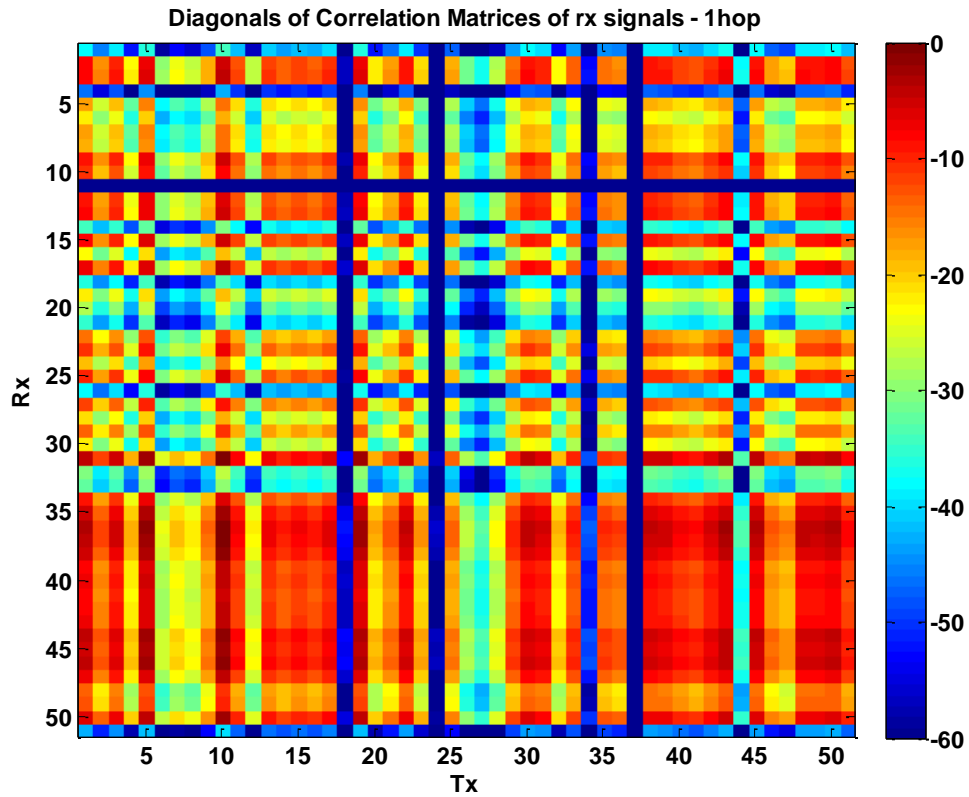
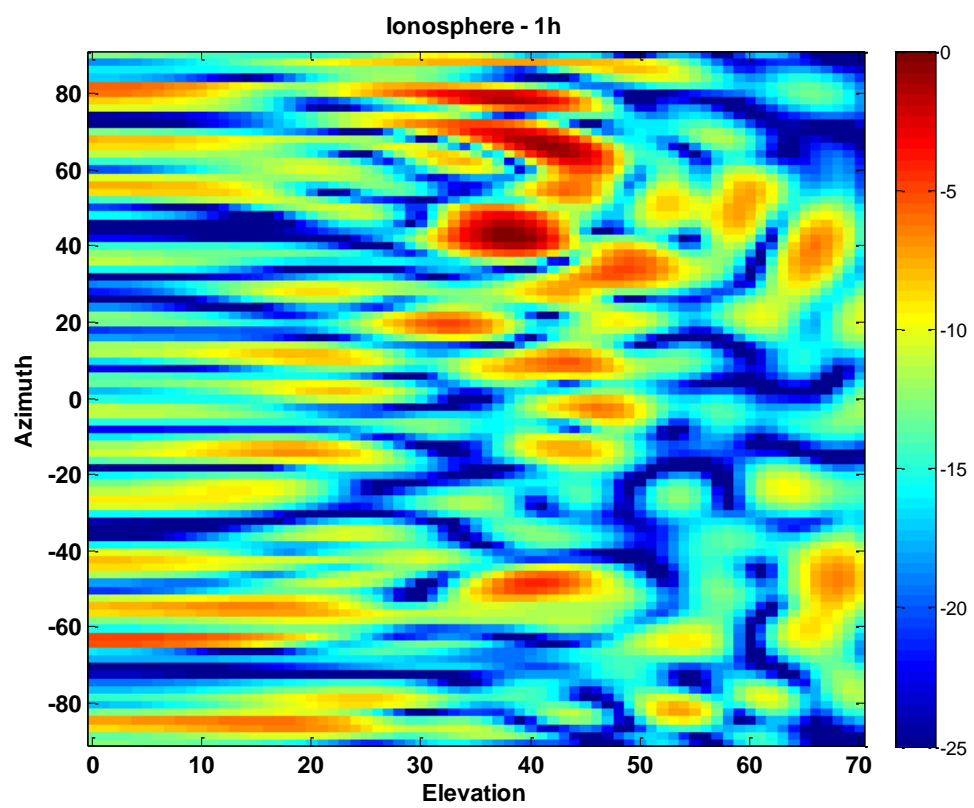


FIGURE 7.18: Result of conventional beamforming for the geometry in Fig.7.1 at time  $t = 0$  with respect to the disturbances period

<b>Geom.2</b>			
<b>1H</b>	$t = 0sec$	$t = 300sec$	$t = 500sec$
$(\theta_{az-ML}, \phi_{el-ML})$	$(56^\circ, 29^\circ)$	$(42^\circ, 38^\circ)$	$(58^\circ, 4^\circ)$
$(\theta_{az-SL1}, \phi_{el-SL1})$	$(62^\circ, 14^\circ)$	$(66^\circ, 42^\circ)$	$(52^\circ, 27^\circ)$
$A_{SL1}$	-0,1673	-0.5093	-0,2245
$N_{SL} > -10dB$	9	> 15	6

TABLE 7.2: Angular location of main lobe (ML), angular location and amplitude of highest sidelobe (SL1) and number of sidelobes higher than  $-10dB$



(a)

FIGURE 7.19: Result of conventional beamforming for the geometry in Fig.7.3 at time  $t = 300$  with respect to the disturbances period

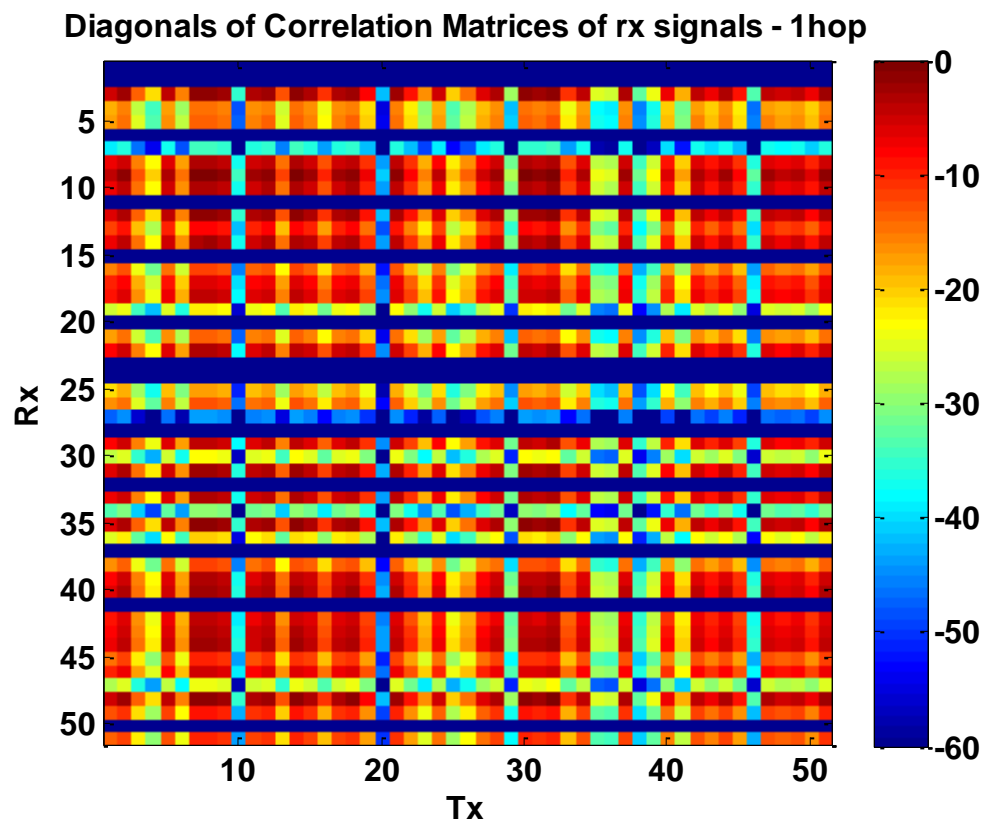


FIGURE 7.20: Result of conventional beamforming for the geometry in Fig.7.3 at time  $t = 300$  with respect to the disturbances period

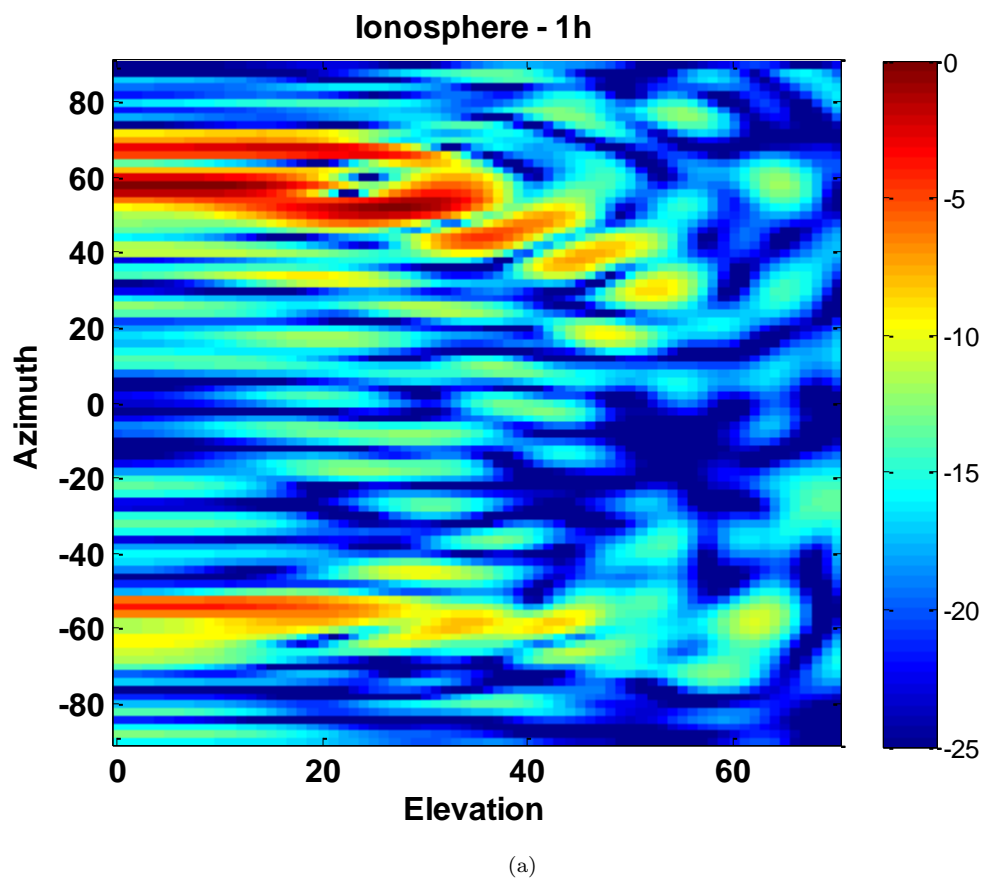


FIGURE 7.21: Result of conventional beamforming for the geometry in Fig.7.3 at time  $t = 500$  with respect to the disturbances period

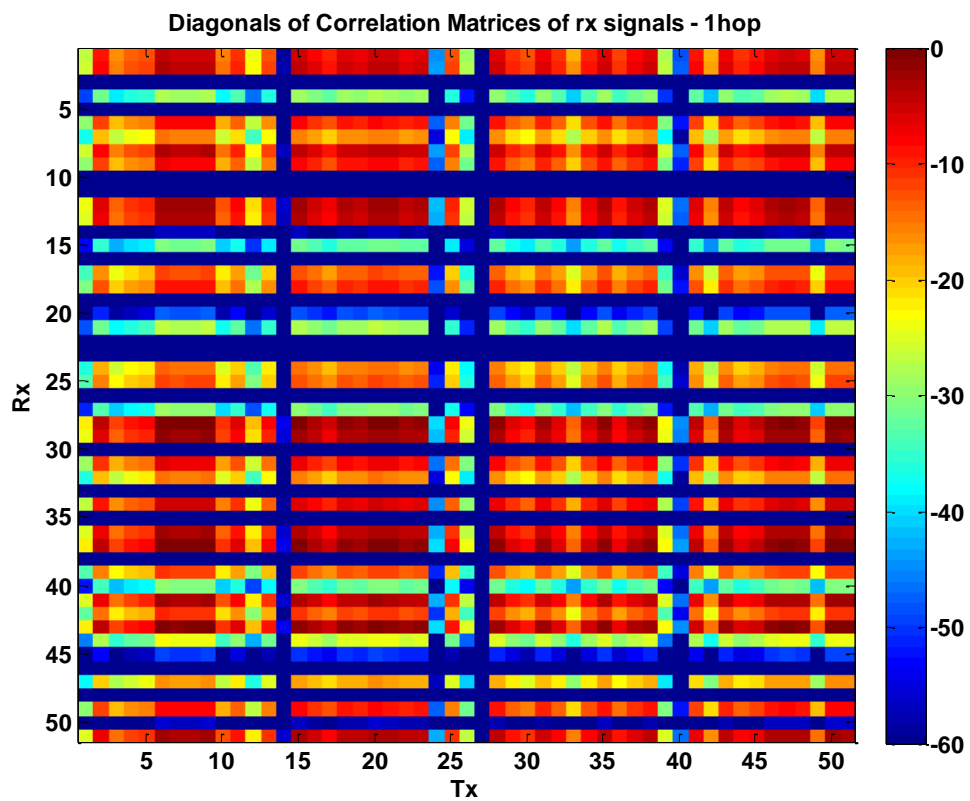


FIGURE 7.22: Result of conventional beamforming for the geometry in Fig.7.3 at time  $t = 500$  with respect to the disturbances period

### 7.3.3 Beamforming for geometry 3

The results of conventional beamforming for geometry 3 at time  $t = 0$  are in Fig.7.23. As can be noted, the signal is detected at the right angular location even though disturbances are present. Similar results are depicted in Fig.7.25 and Fig.7.27 for different time instants. The corresponding matrices that allow for the results interpretation in terms of missing signals are in Fig.7.24, Fig.7.26 and Fig.7.28. Even for geometry 3, it can be easily noticed that the DoA is almost correctly estimated, but very high sidelobe and disturbances are present. This is most likely to be associated with the high level of signal corruption due to the ionospheric degrading phenomena. Tab.7.3 summarizes the beamforming results in terms of number of sidelobes higher than  $-10dB$ , amplitude and angular location of the highest sidelobe and location of the mainlobe.

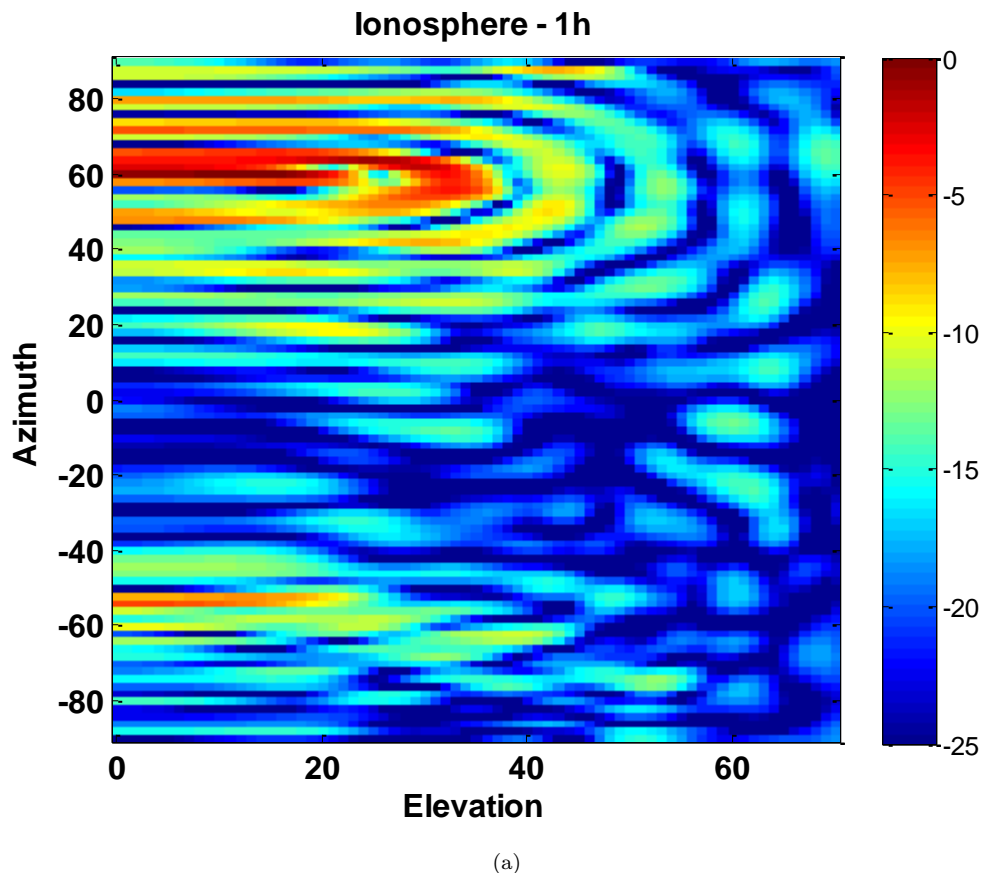


FIGURE 7.23: Result of conventional beamforming for the geometry in Fig.7.5 at time  $t = 0$  with respect to the disturbances period

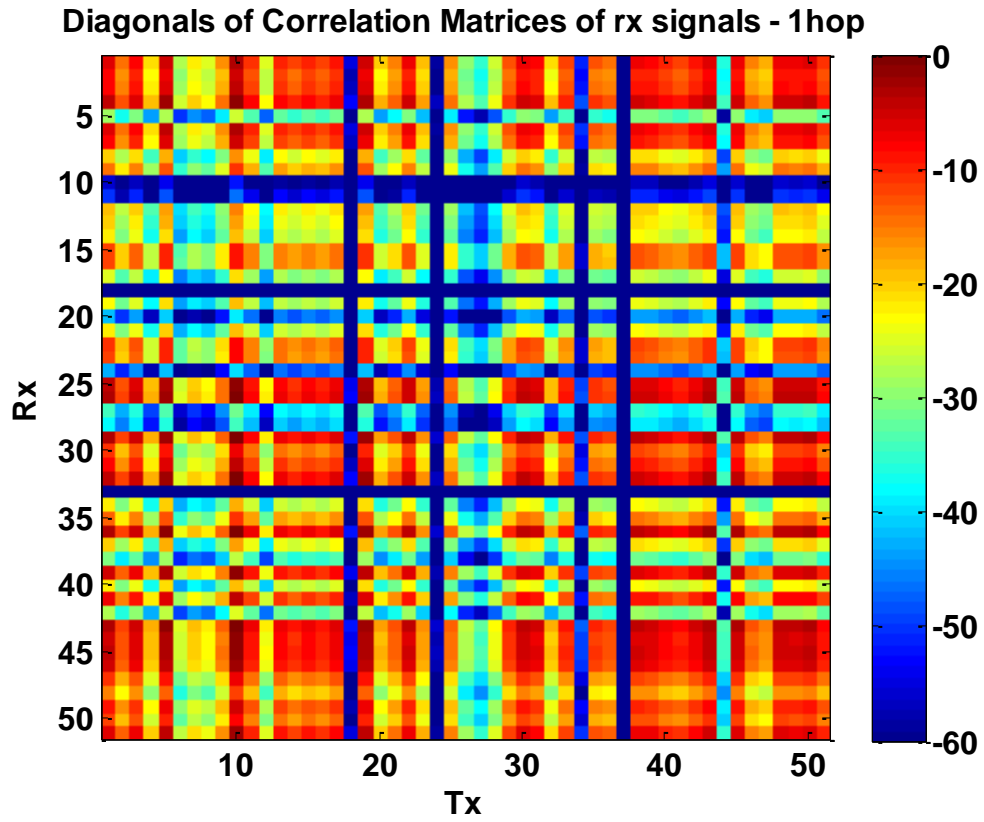


FIGURE 7.24: Result of conventional beamforming for the geometry in Fig.7.5 at time  $t = 0$  with respect to the disturbances period

<b>Geom.3</b>			
<b>1H</b>	$t = 0sec$	$t = 200sec$	$t = 500sec$
$(\theta_{az-ML}, \phi_{el-ML})$	$(62^\circ, 13^\circ)$	$(60^\circ, 13^\circ)$	$(58^\circ, 8^\circ)$
$(\theta_{az-SL1}, \phi_{el-SL1})$	$(54^\circ, 45^\circ)$	$(66^\circ, 26^\circ)$	$(66^\circ, 22^\circ)$
$A_{SL1}$	-1, 215	-0, 8916	-1, 017
$N_{SL} > -10dB$	12	> 20	5

TABLE 7.3: Angular location of main lobe (ML), angular location and amplitude of highest sidelobe (SL1) and number of sidelobes higher than  $-10dB$

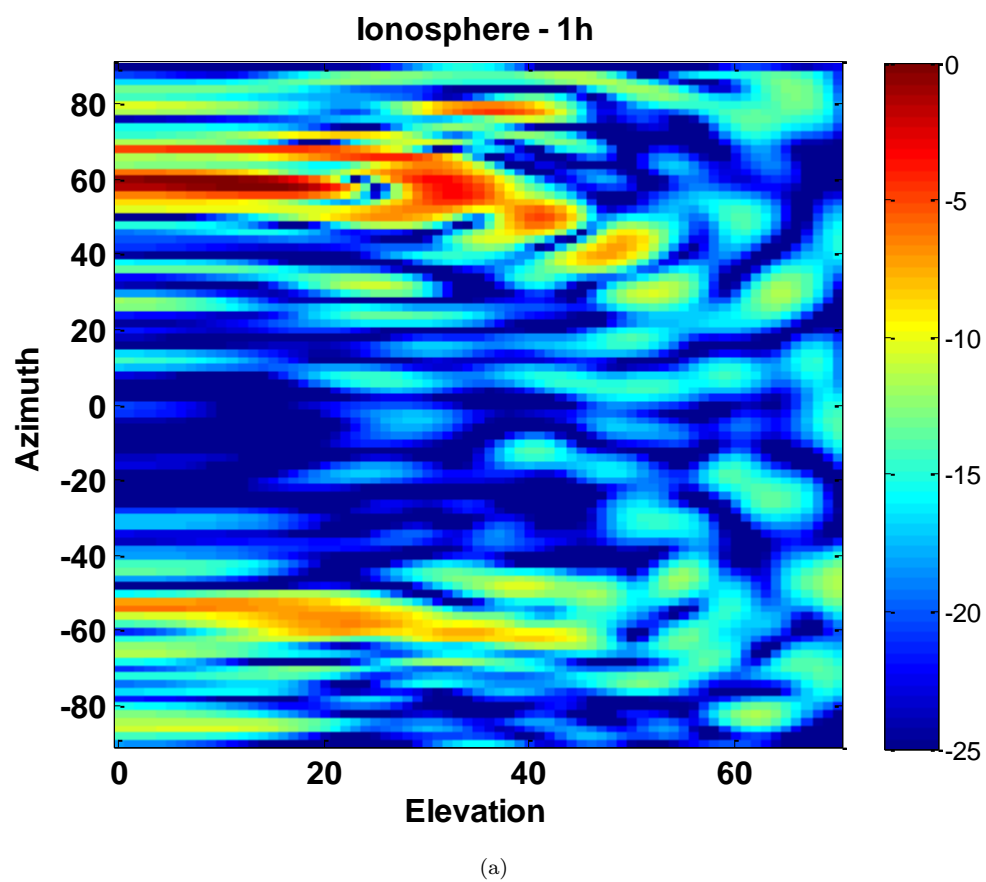


FIGURE 7.25: Result of conventional beamforming for the geometry in Fig.7.5 at time  $t = 300$  with respect to the disturbances period

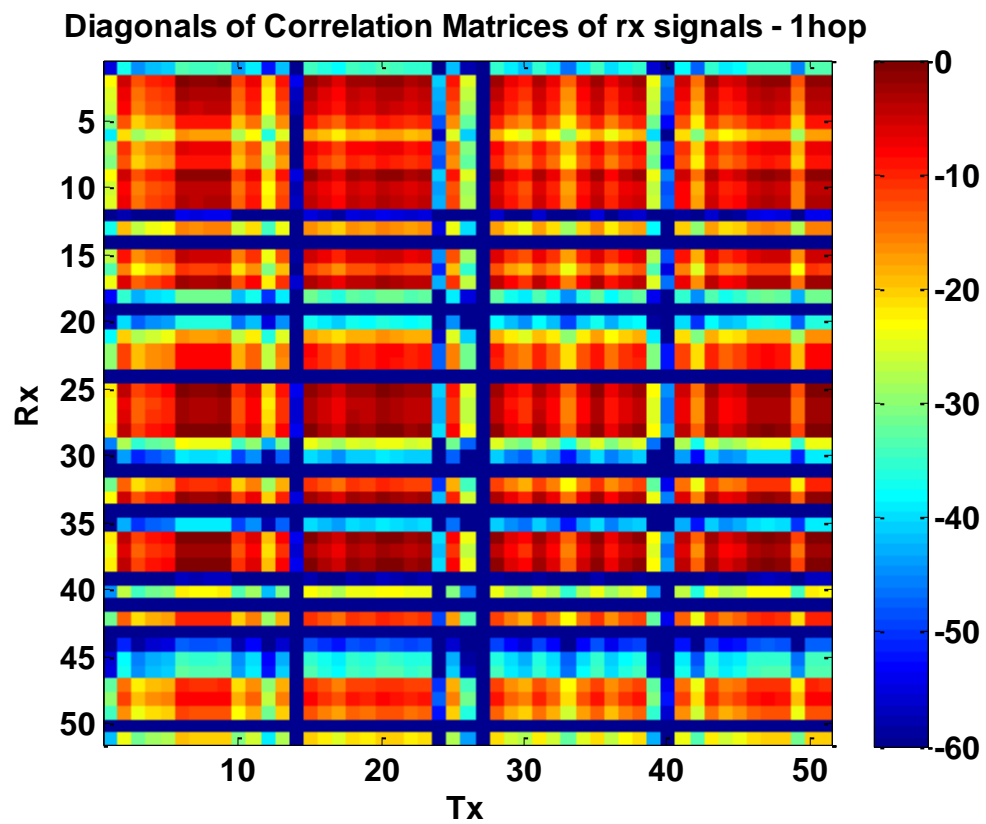


FIGURE 7.26: Result of conventional beamforming for the geometry in Fig.7.5 at time  $t = 300$  with respect to the disturbances period

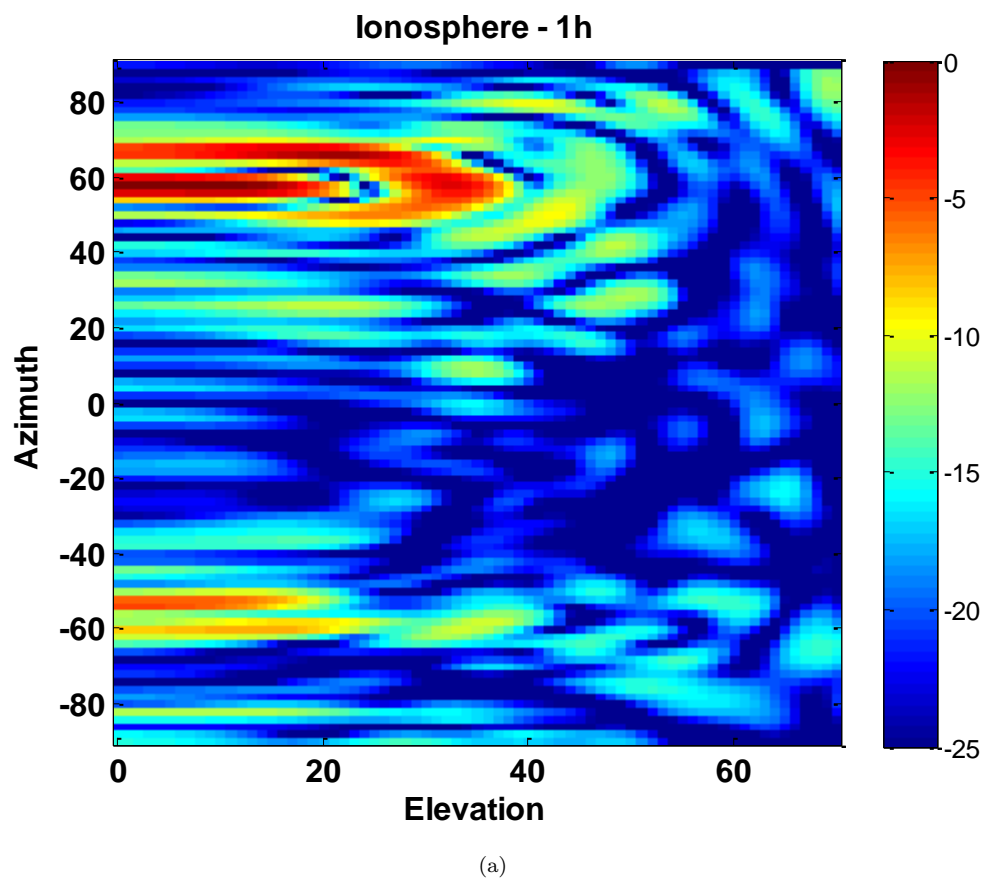


FIGURE 7.27: Result of conventional beamforming for the geometry in Fig.7.5 at time  $t = 500$  with respect to the disturbances period

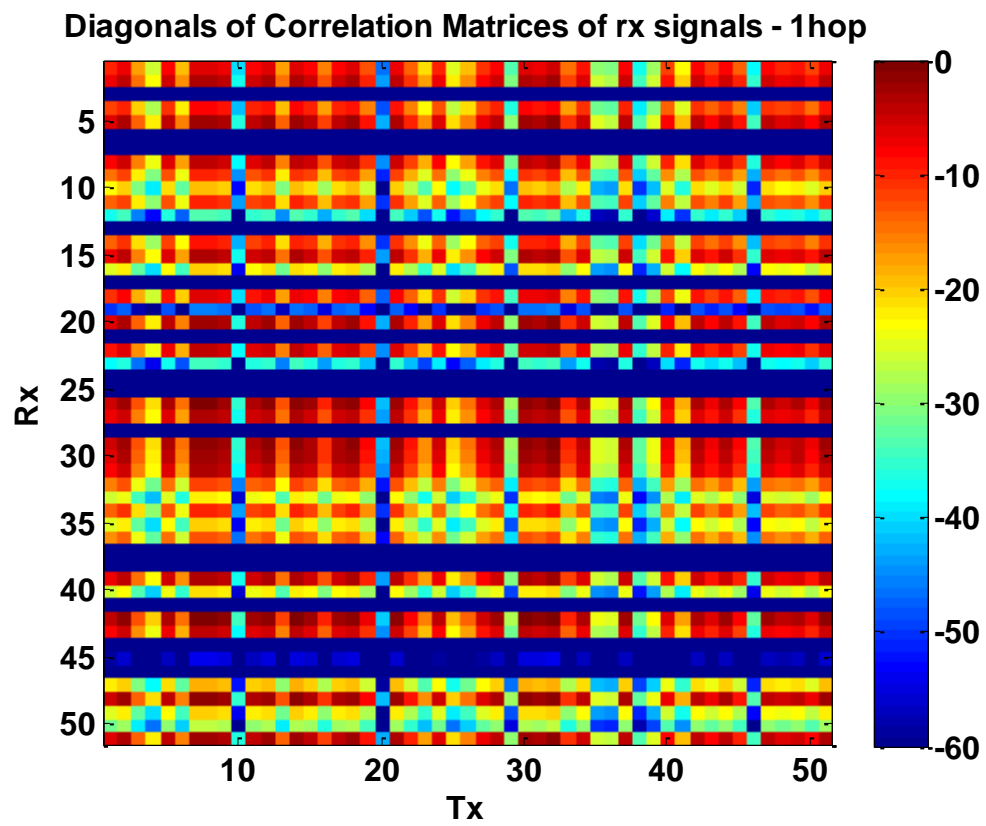


FIGURE 7.28: Result of conventional beamforming for the geometry in Fig.7.5 at time  $t = 500$  with respect to the disturbances period

All the above presented results refer to a single hop propagation. Simulations have been performed also for the case of two hops, but for the considered ionosphere state, and the system geometry there are no two hops paths available.

### 7.3.4 Remarks on beamforming results

The analysis of the beamforming results shown in the previous sections has demonstrated that the effects of the ionosphere have a big impact on the DoA estimation. In particular, the presence of ionospheric disturbances can lead to high signal attenuation that coincides to the loss of some elements of the MIMO virtual array. Such a high attenuation is the result of destructive interference due to ionospheric multipath as well as due to high propagation losses and polarization mismatch related to the Faraday rotation.

Three different geometries have been considered in order to understand the implications of the system geometry on the beamforming performance. Beamforming performance has been measured in terms of level of the highest sidelobe and number of sidelobes higher than  $-10dB$ , as shown in Tab.7.1-7.3. As can be noticed, the signal is detected in the right angular position, but a number of high sidelobes are present for every geometry tested. It can be easily noticed that the results obtained with geometry 2 show fewer angular sidelobes (higher than  $-10dB$ ) with respect to geometry 1 and geometry 3. Notwithstanding, in geometry 2 the level of the highest angular sidelobe is generally higher than the results obtained with geometry 1 and geometry 3.

## 7.4 Detection performance results and ROC

This section aims at evaluating the receiver performance in terms of Receiver Operative Curves (ROCs).

The simulation performed in order to evaluate the ROCs are based on the signal model described in Ch.5. In particular, the simulations have been performed considering the ionospheric state defined in Tab.6.1 and Tab.6.2, the target location

in Tab.6.4 and geometry 2. In order to understand the effects of ionospheric multipath on the receiver performance, the case with ionospheric multipath and the case in which only one propagation path is available are considered.

The noise and the target reflectivity have been modelled as independent zero mean Gaussian vectors and covariance matrices  $\mathbf{R}_w = \sigma_w^2 \mathbf{I}$  and  $\mathbf{R}_\sigma = \sigma_\sigma^2 \mathbf{I}$  respectively. A perturbed ionosphere is considered, with a TID period of 600sec.

The LRT in Eq.(5.40) is used and 100000 Monte Carlo simulations have been performed to evaluate the ROC curves, for a false alarm probability ranging from  $10^{-6}$  and 1 and a SNR ranging from  $-20dB$  and  $20dB$ .

All of the above simulations requires the evaluation of the ray path for the background ionosphere and this is achieved through point to point ray tracing [58].

Fig.7.29(b) shows the ROCs in case of multipath while Fig.7.29(a) shows the ROCs for the case in which only one path is considered for all the point-to-point combinations. It can be easily noticed that the results with the multipath are better than the case without multipath. This fact can be explained considering that in case of multipath, echoes coming from different target points can be associated with uncorrelated measurements that improve the detection performance. On the other hand, it is worth pointing out that the presence of multipath can be an issue for DoA estimation since multiple returns from multiple directions can lead to errors in the estimation of the actual direction of arrival of the signal.

## 7.5 Summary

The present chapters concludes the work done in this thesis. In particular, it gathers the major results obtained with the signal model developed in Ch.5 and draws the conclusion about the analysis performed with the simulator developed during the research activity.

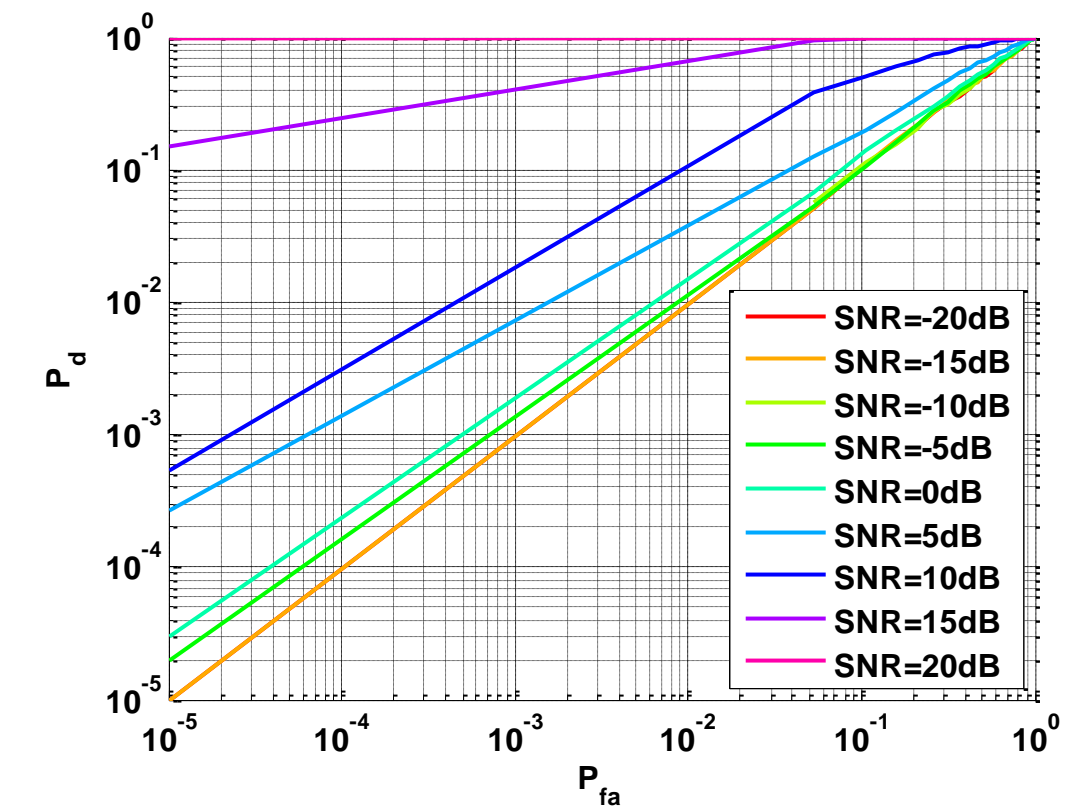
The scenario has been described first, with special attention to the three different

geometries used. For each configuration, the geometry of the transmitter and receiver arrays are described and the virtual array which is the result of the spatial convolution of the transmitter and receiver elements location is shown.

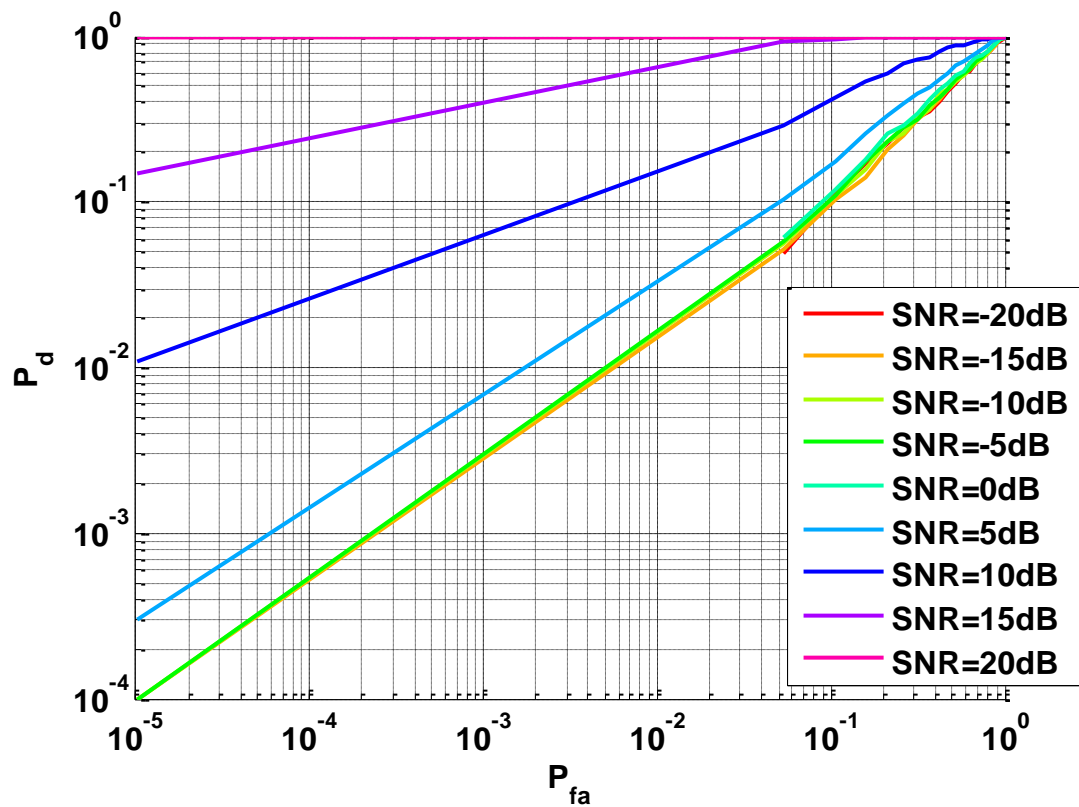
The problem of waveform orthogonality after ionospheric propagation is then faced. Simulations have been performed and the cross correlation matrix of the received signals evaluated at each receiver in order to measure the effects of the ionosphere on the waveform orthogonality. The results obtained have demonstrated that when ionosphere is perturbed by TIDs, the orthogonality of the transmitted waveforms is preserved. Notwithstanding, it will be interesting to pursue further studies including additional ionospheric perturbation, such as scintillation, in order to understand if different phenomena can degrade waveform orthogonality.

Notwithstanding, corruption of the transmitted signal during ionospheric propagation is evident on the DoA estimation. Conventional beamforming results have shown that the signal attenuation due to fading and interference can be so strong to prevent the signal detection. In addition, the unpredictable amount of amplitude attenuation due to polarization mismatching is responsible for high sidelobes and disturbances in the beamforming results.

The analysis of the receiver performance has been performed by means of ROCs. ROCs have been evaluate both in case of single path propagation and ionospheric multipath. A comparison between the results has demonstrated that in case of ionospheric multipath better performance are obtained.



(a)



(b)

FIGURE 7.29: ROC curves in case of single path propagation (a) and ionospheric multipath (b)

# Chapter 8

## Conclusion & Future Work

HF skywave radars have been widely used as an effective and low cost tool for wide area surveillance and detection of targets far beyond the optical horizon by means of ionospheric propagation. Notwithstanding, the dispersive nature of the ionosphere, its spatial non-homogeneity and temporal non-stationarity are at the basis of limitations in the system performance. In particular, ionospheric perturbations are responsible for high signal attenuation due to fading phenomena and spread Doppler clutter which can mask the returns from target of interest.

MIMO technology has been suggested as an effective tool to overcome some of issues typical of OTH skywave radar. In fact, they can be employed for spread Doppler clutter suppression and enhanced adaptive processing algorithms. Moreover, the transmission of multiple waveforms allows for the introduction of spatial directivity into the radar management support subsystem.

In fact, HF MIMO radars are based on the transmission of a set of linearly independent waveforms and their separation at the receiver in order to fully exploit the capabilities of MIMO technology. Notwithstanding, the orthogonality of the transmitted signals can be corrupted by ionospheric effects during the propagation from the transmitter to the receiver. As a consequence, a study of the ionosphere and the way it affects the transmitted signals is essential for the design of an HF MIMO skywave radar.

The HF MIMO radar signal simulator developed in the present thesis is an effective tool that can be used to evaluate the signal at the receiver for a number of ionospheric state and different system configurations. The work behind the development of such a simulator has started with the study of the MIMO technology applied to HF skywave radars. In this regard, the issues related to the transmission of a set of orthogonal waveforms has been tackled and different solutions proposed, with special attention to the bandwidth occupation since the ionosphere only supports few tens of  $kHz$  spectral occupancy.

Since HF MIMO functioning relies on the separation of the transmitted signal contributions, the demodulation problem has been faced. Two different solutions have been studied. The first one, is based on the use of a bank of matched filters at each receiver element while the second is based on the deramping process.

In order to derive a proper HF MIMO signal model, the ionosphere morphology has been investigated with the aim of identifying the way ionospheric disturbances affect the transmitted signals. The attention has been focused on the changes in group delay, phase delay and signal attenuation due to electron content variations caused by TIDs. In addition, ionospheric multipath has been included in the signal model. The expression of the signal at the receiver site has been used to solve the detection problem and the LRT has been derived.

All the information gained with the study of the ionosphere and the signal modulation and demodulation has been exploited for the implementation of software routines which compose the simulator. The software optimization problem has been faced in order to reduce the processing time. In particular, the use of linear interpolation to evaluate the signal parameters after ionospheric propagation has been investigated. The results obtained demonstrated that it is possible to exploit the interpolation in order to evaluate the signal parameters in the spatial domain, i.e. for all the elements of the array. The simulations have been performed for different array lengths in order to understand the limitation in the application of the linear interpolation. The use of linear interpolation has been investigated also for the evaluation of the signal parameters in the frequency domain.

The optimized simulator has been used for the analysis of three different aspects

of HF MIMO skywave radars. First of all, the problem of waveform orthogonality after ionospheric propagation has been faced in order to understand whether the ionosphere can affect the property of the transmitted signals. In this regards, the results obtained via evaluation of the cross correlation matrix of the signals at the receiver site have shown that when TIDs are considered as ionospheric perturbations, waveform orthogonality is preserved.

Another aspect that has been considered is the problem of DoA estimation via conventional beamforming. Simulations performed for different ionospheric states have shown that ionospheric corruption leads to high sidelobes and distortions in the beamforming results. The same simulations have been performed for different system geometries in order to understand whether the system configuration has any impact on the beamforming performance. It has been demonstrated that a circular geometry offers better results in terms of number of angular sidelobes with respect to the use of linear arrays. Notwithstanding, the amplitude of the highest angular sidelobe for circular arrays is generally higher than the case in which linear arrays are used.

At the end, the receiver performance have been analysed by means of ROCs. The simulations have been performed for the case of single path propagation and multipath propagation. A comparison between these two cases have demonstrated that multipath propagation allows for better performance thanks to the processing of multiple returns that offers benefits in fading environment such as the ionosphere.

Further topics can be investigated in this research area.

First of all, further studies on ionospheric perturbations can be pursued in order to enhance the signal model. In this regard, an important aspect to be considered is about the effects of scintillation on propagating signal, since they are responsible for spread Doppler and spread range phenomena.

From the perspective of waveform design, other signalling techniques should be studied, for example the use of codes to create a set of orthogonal waveforms to be transmitted. It would be interesting to understand the effects of the ionosphere on this kind of modulation and see whether they are robust against ionospheric corruption. In addition, an important aspect to be considered in the waveform

design is associated to the sidelobe of the range-angle ambiguity function. In fact, besides being linearly independent, the transmitted waveforms must be selected in order to reduce the range-angle ambiguity function sidelobes as much as possible. In this way, the interferences among adjacent cells due to these sidelobes can be reduced.

In regard of beamforming, adaptive beamforming techniques can be applied to enhance DoA estimation performance. Moreover, the use of sparse geometries would be interesting to be investigated in order to find an optimal solution for the virtual array geometry with the minimum number of real antennas.

At the end, is worth saying that other methods for software optimization can be studied in order to optimize the routines and reduce the time of processing.

# Bibliography

- [1] J. Ender. 98 years of the RADAR principle: the inventor Christian Hülsmeier. *EUSAR2002*, June 2002.
- [2] S.B. Colegrove. Project JINDA $\grave{a}$ LEE: from bare bones to operationa lOTHR. In *Radar Conference, 2000. The Record of the IEEE 2000 International*, pages 825–830, 2000. doi: 10.1109/RADAR.2000.851942.
- [3] A. Cameron. The JINDA $\grave{a}$ LEE operational radar network: its architecture and surveillance capability. In *Radar Conference, 1995., Record of the IEEE 1995 International*, pages 692–697, 1995. doi: 10.1109/RADAR.1995.522633.
- [4] V. Bazin, J.-P. Molinie, J. Munoz, P. Dorey, S. Saillant, G. Auffray, V. Rannou, and M. Lesturgie. A general presentation about the OTH-Radar NOSTRADAMUS. In *Radar, 2006 IEEE Conference on*, pages 9 pp.–, 2006. doi: 10.1109/RADAR.2006.1631867.
- [5] V. Bazin, J.-P. Molinie, J. Munoz, P. Dorey, S. Saillant, G. Auffray, V. Rannou, and M. Lesturgie. NOSTRADAMUS: An OTH radar. *Aerospace and Electronic Systems Magazine, IEEE*, 21(10):3–11, 2006. ISSN 0885-8985. doi: 10.1109/MAES.2006.275299.
- [6] Stephen L. Johnston. Survey of Chinese radars. In *Radar Conference, 1995., Record of the IEEE 1995 International*, pages 261–268, 1995. doi: 10.1109/RADAR.1995.522556.
- [7] M. Skolnik. *Radar Handbook, 3<sup>rd</sup> Edition*. McGraw-Hill Professional, London, U.K., 2008.

- [8] S.J. Anderson. Directional wave spectrum measurement with multistatic HF surface wave radar. In *Geoscience and Remote Sensing Symposium, 2000. Proceedings. IGARSS 2000. IEEE 2000 International*, volume 7, pages 2946–2948 vol.7, 2000. doi: 10.1109/IGARSS.2000.860299.
- [9] T.M. Blake. Ship detection and tracking using high frequency surface wave radar. In *HF Radio Systems and Techniques, Seventh International Conference on (Conf. Publ. No. 441)*, pages 291–295, 1997. doi: 10.1049/cp:19970807.
- [10] K. Davies. *Ionospheric Radio*. Peter Peregrinus Ltd., London, U.K., 1990. ISBN 086341186X.
- [11] J. Barnum. Ship detection with high-resolution hf skywave radar. *Oceanic Engineering, IEEE Journal of*, 11(2):196–209, 1986. ISSN 0364-9059. doi: 10.1109/JOE.1986.1145176.
- [12] M. D E Turley. Signal processing techniques for maritime surveillance with skywave radar. In *Radar, 2008 International Conference on*, pages 241–246, 2008. doi: 10.1109/RADAR.2008.4653925.
- [13] G. F. Earl and B. D. Ward. The frequency management system of the JINDALEE over-the-horizon backscatter HF radar. *Radio Science*, 22(2): 275–291, 1987. ISSN 1944-799X. doi: 10.1029/RS022i002p00275. URL <http://dx.doi.org/10.1029/RS022i002p00275>.
- [14] T. Georges, Jr. Maresca, J., J. Riley, and C. Carlson. Real-time sea-state surveillance with skywave radar. *Oceanic Engineering, IEEE Journal of*, 8(2):97–103, 1983. ISSN 0364-9059. doi: 10.1109/JOE.1983.1145550.
- [15] S. Anderson. Prospects for tsunami detection and characterisation with HF skywave radar. In *Radar, 2008 International Conference on*, pages 639–645, 2008. doi: 10.1109/RADAR.2008.4654000.

- 
- [16] S.J. Anderson, Y.I. Abramovich, and A. I. Skinner. Robust mapping of tropical cyclone wave fields using HF skywave radar. In *RADAR 2002*, pages 47–50, 2002. doi: 10.1109/RADAR.2002.1174651.
- [17] D. Bilitza. International Reference Ionosphere 2000. *Radio Science*, 36(2): 261–275, 2001.
- [18] A. L. Saverino, A. Capria, F. Berizzi, and E. Dalle Mese. Cognitive adaptive waveform technique for HF skywave radar. In *Cognitive Information Processing (CIP), 2010 2nd International Workshop on*, pages 247–252, 2010. doi: 10.1109/CIP.2010.5604247.
- [19] Coleman C.J. A model of HF sky wave radar clutter. *Radio Science*, 31(4): 869–875, 1996. doi: 10.1029/96RS00721.
- [20] John M. Goodman, J. Zinn, Michael H. Reilly, T. J. Fitzgerald, Morris B. Pongratz, P. B. Morris, Paul A. Bernhardt, Charles M. Rush, Lewis M. Duncan, and Santimay. Basu. Effect of the Ionosphere on Radiowave Systems. In *Ionospheric Effects Symposium, Conference Proceedings*, 1981.
- [21] Kun Lu and Zhijian Chen. Elimination of ionospheric multipath propagation effect for over-the-horizon radar. In *Radar, 2006. CIE '06. International Conference on*, pages 1–5, 2006. doi: 10.1109/ICR.2006.343586.
- [22] J.M. Headrick and M.I. Skolnik. Over-the-horizon radar in the HF band. *Proceedings of the IEEE*, 62(6):664–673, 1974. ISSN 0018-9219. doi: 10.1109/PROC.1974.9506.
- [23] A.J. Paulraj, D.A. Gore, R.U. Nabar, and H. Bolcskei. An overview of MIMO communications - a key to gigabit wireless. *Proceedings of the IEEE*, 92(2): 198–218, 2004. ISSN 0018-9219. doi: 10.1109/JPROC.2003.821915.
- [24] R.K. Mehra. Optimal input signals for parameter estimation in dynamic systems—survey and new results. *Automatic Control, IEEE Transactions on*, 19(6):753–768, 1974. ISSN 0018-9286. doi: 10.1109/TAC.1974.1100701.

- [25] J.-M. Colin. Phased array radars in france: present and future. In *Phased Array Systems and Technology, 1996., IEEE International Symposium on*, pages 458–462, 1996. doi: 10.1109/PAST.1996.566137.
- [26] V.S. Chernyak. On the concept of MIMO radar. In *Radar Conference, 2010 IEEE*, pages 327–332, 2010. doi: 10.1109/RADAR.2010.5494601.
- [27] E. Fishler, A. Haimovich, R. Blum, D. Chizhik, L. Cimini, and R. Valenzuela. MIMO radar: an idea whose time has come. In *Radar Conference, 2004. Proceedings of the IEEE*, pages 71–78, 2004. doi: 10.1109/NRC.2004.1316398.
- [28] B. J. Donnet and I. D. Longstaff. MIMO radar, techniques and opportunities. In *Radar Conference, 2006. EuRAD 2006. 3rd European*, pages 112–115, 2006. doi: 10.1109/EURAD.2006.280286.
- [29] F. Daum and J. Huang. MIMO radar: Snake oil or good idea? In *Waveform Diversity and Design Conference, 2009 International*, pages 113–117, 2009. doi: 10.1109/WDDC.2009.4800326.
- [30] F.C. Robey, S. Coutts, D. Weikle, J.C. McHarg, and K. Cuomo. MIMO radar theory and experimental results. In *Signals, Systems and Computers, 2004. Conference Record of the Thirty-Eighth Asilomar Conference on*, volume 1, pages 300–304 Vol.1, 2004. doi: 10.1109/ACSSC.2004.1399141.
- [31] A.M. Haimovich, R.S. Blum, and L.J. Cimini. MIMO radar with widely separated antennas. *Signal Processing Magazine, IEEE*, 25(1):116–129, 2008. ISSN 1053-5888. doi: 10.1109/MSP.2008.4408448.
- [32] E. Fishler, A. Haimovich, R.S. Blum, L.J. Cimini, D. Chizhik, and R.A. Valenzuela. Spatial diversity in radars-models and detection performance. *Signal Processing, IEEE Transactions on*, 54(3):823–838, 2006. ISSN 1053-587X. doi: 10.1109/TSP.2005.862813.
- [33] N.H. Lehmann, A.M. Haimovich, R.S. Blum, and L. Cimini. High resolution capabilities of MIMO radar. In *Signals, Systems and Computers*,

2006. *ACSSC '06. Fortieth Asilomar Conference on*, pages 25–30, 2006. doi: 10.1109/ACSSC.2006.356576.
- [34] Jian Li and Petre Stoica. MIMO radar with colocated antennas. *Signal Processing Magazine, IEEE*, 24(5):106–114, 2007. ISSN 1053-5888. doi: 10.1109/MSP.2007.904812.
- [35] M. Weiss. Digital antennas. *Multistatic Surveillance and reconnaissance: Sensor, Signals and Data Fusion. educational Notes RTO-EN-SET133, paper 5*, pages 5–1 – 5–29, 2009. doi: 1.
- [36] Jian Li and Peter Stoica. *MIMO Radar Signal Processing*. Wiley & Sons, 2008. ISBN 9780470178980.
- [37] J. J. M. De Wit, W.L. Van Rossum, and A.J. De Jong. Orthogonal waveforms for FMCW MIMO radar. In *Radar Conference (RADAR), 2011 IEEE*, pages 686–691, 2011. doi: 10.1109/RADAR.2011.5960625.
- [38] B. J. Donnet and I. D. Longstaff. MIMO radar- waveforms and applications. In *4<sup>th</sup> EMRS DTC Technical Conference*, Edinburgh, 2007.
- [39] T. Aittomaki and V. Koivunen. Signal covariance matrix optimization for transmit beamforming in MIMO radars. In *Signals, Systems and Computers, 2007. ACSSC 2007. Conference Record of the Forty-First Asilomar Conference on*, pages 182–186, 2007. doi: 10.1109/ACSSC.2007.4487191.
- [40] Petre Stoica, Jian Li, and Yao Xie. On probing signal design for MIMO radar. *Signal Processing, IEEE Transactions on*, 55(8):4151–4161, 2007. ISSN 1053-587X. doi: 10.1109/TSP.2007.894398.
- [41] D.R. Fuhrmann and G. San Antonio. Transmit beamforming for MIMO radar systems using partial signal correlation. In *Signals, Systems and Computers, 2004. Conference Record of the Thirty-Eighth Asilomar Conference on*, volume 1, pages 295–299 Vol.1, 2004. doi: 10.1109/ACSSC.2004.1399140.
- [42] D.R. Fuhrmann and G. San Antonio. Transmit beamforming for MIMO radar systems using signal cross-correlation. *Aerospace and Electronic Systems*,

- IEEE Transactions on*, 44(1):171–186, 2008. ISSN 0018-9251. doi: 10.1109/TAES.2008.4516997.
- [43] D.A. Gray and R. Fry. MIMO noise radar - element and beam space comparisons. In *Waveform Diversity and Design Conference, 2007. International*, pages 344–347, 2007. doi: 10.1109/WDDC.2007.4339440.
- [44] G.J. Frazer, Y.I. Abramovich, B.A. Johnson, and F.C. Robey. Recent results in MIMO over-the-horizon radar. In *Radar Conference, 2008. RADAR '08. IEEE*, pages 1–6, 2008. doi: 10.1109/RADAR.2008.4720867.
- [45] Gordon J. Frazer, Y.I. Abramovich, and B.A. Johnson. Spatially waveform diverse radar: Perspectives for high frequency OTHR. In *Radar Conference, 2007 IEEE*, pages 385–390, 2007. doi: 10.1109/RADAR.2007.374247.
- [46] G.J. Frazer, Y.I. Abramovich, and B.A. Johnson. HF skywave MIMO radar: The HILOW experimental program. In *Signals, Systems and Computers, 2008 42nd Asilomar Conference on*, pages 639–643, 2008. doi: 10.1109/ACSSC.2008.5074484.
- [47] G.J. Frazer, Y.I. Abramovich, and B.A. Johnson. Multiple-input multiple-output over-the-horizon radar: experimental results. *Radar, Sonar Navigation, IET*, 3(4):290–303, 2009. ISSN 1751-8784. doi: 10.1049/iet-rsn.2008.0142.
- [48] Gordon J. Frazer, B.A. Johnson, and Y.I. Abramovich. Orthogonal waveform support in MIMO HF OTH radars. In *Waveform Diversity and Design Conference, 2007. International*, pages 423–427, 2007. doi: 10.1109/WDDC.2007.4339454.
- [49] Jian Li, Petre Stoica, and Xumin Zhu. Mimo radar waveform synthesis. In *Radar Conference, 2008. RADAR '08. IEEE*, pages 1–6, 2008. doi: 10.1109/RADAR.2008.4721118.
- [50] A.G. Stove. Linear FMCW radar techniques. *Radar and Signal Processing, IEE Proceedings F*, 139(5):343–350, 1992. ISSN 0956-375X.

- [51] P.E. Pace. *Detecting and Classifying Low Probability of Intercept Radar*. Artech House Remote Sensing Library. Artech House, 2009. ISBN 9781596932357. URL [http://books.google.it/books?id=K\\_T4M-na6JYC](http://books.google.it/books?id=K_T4M-na6JYC).
- [52] A. Hassanien and S.A. Vorobyov. Transmit/receive beamforming for MIMO radar with colocated antennas. In *Acoustics, Speech and Signal Processing, 2009. ICASSP 2009. IEEE International Conference on*, pages 2089–2092, april 2009. doi: 10.1109/ICASSP.2009.4960027.
- [53] G. Babur, O.A. Krasnov, A. Yarovoy, and P. Aubry. Nearly orthogonal waveforms for MIMO FMCW radar. *Aerospace and Electronic Systems, IEEE Transactions on*, 49(3):1426–1437, 2013. ISSN 0018-9251. doi: 10.1109/TAES.2013.6557996.
- [54] J.V. Evans. High-power radar studies of the ionosphere. *Proceedings of the IEEE*, 63(12):1636–1650, 1975. ISSN 0018-9219. doi: 10.1109/PROC.1975.10032.
- [55] A.S. Jursa. *Handbook of Geophysics and the Space Environment*. Air Force Geophysics Laboratory, 1985. URL [http://www.cnofs.org/Handbook\\_of\\_Geophysics\\_1985/](http://www.cnofs.org/Handbook_of_Geophysics_1985/).
- [56] J.A. Ratcliffe. *Sun, Earth, and Radio: An Introduction to the Ionosphere and Magnetosphere*. World University Library. McGraw-Hill, 1970. URL <http://books.google.it/books?id=yexEAAAAIAAJ>.
- [57] D. Blitza. *International reference Ionosphere*. URL <http://iri.gsfc.nasa.gov/>.
- [58] C.J. Coleman. A ray tracing formulation and its application to some problems in over-the-horizon radar. *Radio Science*, 33(4):1187–1197, July/August 1998.
- [59] Coleman C.J. A general purpose ionospheric ray tracing procedure, tech.rep.,SRL0131TR. *Def. Sci. and Technol. Organ.*, 1993.

- [60] Asnawi, M. Abdullah, and M.A. Momani. Medium scale travelling ionospheric disturbance detection using GPS MyRTKnet. In *Space Science and Communication, 2009. IconSpace 2009. International Conference on*, pages 153–156, Oct. 2009. doi: 10.1109/ICONSPACE.2009.5352650.
- [61] M. Rieger and R. Leitinger. The effect of travelling ionospheric disturbances (TIDs) on GNSS user systems. In *Proceedings of the 27th General Assembly of URSI*, Maastricht, The Netherlands, 2002.
- [62] K. S. B. Yau. A simple polarisation fading model for HF propagation in the ionosphere. *IEE*, Conference pub. 493:131–135, 2003.
- [63] R. J. Sullivan M. T. Tuley, T. C. Miller. Ionospheric scintillation effect on a space based foliage penetration ground moving target indication radar. August 2001.
- [64] K.S.B. Yau, C.J. Coleman, and M.A. Cervera. Investigation on fading of High Frequency radio signals propagating in the ionosphere - Results from a Jindalee radar experiment. In *Ionospheric Radio Systems and Techniques, 2006. IRST 2006. 10th IET International Conference on*, pages 7–11, july 2006.
- [65] Hannu Koskinen. *Physics of Space Storms: From the Surface of the Sun to the Earth*. Springer Heidelberg Dordrecht London New York, 2011. ISBN 978-3-642-00310-3. doi: 10.1007/978-3-642-00319-6.
- [66] J.A. Bennett. The calculation of Doppler shifts due to a changing ionosphere. *Journal of Atmospheric and Terrestrial Physics*, 29(7):887–891, 1967. ISSN 0021-9169. doi: 10.1016/0021-9169(67)90055-4. URL <http://www.sciencedirect.com/science/article/pii/0021916967900554>.
- [67] C.L. Weber. *Principles of radar system design*. University of Southern California, 1984.